

MODELING AND SIMULATION OF VISCOELASTIC SOFT MATERIALS FOR  
SOFT ROBOTIC APPLICATIONS

A Dissertation

by

JIAN QU

Submitted to the Office of Graduate and Professional Studies of  
Texas A&M University  
in partial fulfillment of the requirements for the degree of

DOCTOR OF PHILOSOPHY

Chair of Committee,	Anastasia Muliana
Committee Members,	Alan Freed
	Sevan Goenezen
	Jun Kameoka
	Kamran Khan
Head of Department,	Andreas A. Polycarpou

May 2020

Major Subject: Mechanical Engineering

Copyright 2020 Jian Qu

## ABSTRACT

This study presents numerical simulations of deformations and shape changes in soft and flexible systems suitable for soft robotics structures. The compliant nature of soft materials, such as silicone elastomer, rubber and PDMS, makes them appealing for soft robotic applications. In some applications, such as surgical devices, precise controls of shape reconfigurations are necessary. To achieve high precision motion in soft robots, it requires incorporating detailed material responses in simulation the shape reconfigurations in soft robots. In this study, we formulate a constitutive model for nonlinear viscoelastic response of soft materials. Both isotropic and anisotropic responses are considered. The constitutive model is implemented within user material subroutines (UMAT) within ABAQUS finite element analysis. Finite element is then used to simulate and investigate the response of the soft robotics devices, such as pneumatic soft actuators and micro-hands. Furthermore, an investigation of soft composites comprising of elastic fiber and nonlinear viscoelastic matrix for potential applications in soft robots is presented. Parametric studies are carried out to obtain a better understanding of the design of soft composites.

## ACKNOWLEDGEMENTS

I would like to express my deepest appreciation to my advisor, Professor Anastasia Muliana. I am able to be introduced in the world of mechanics under your guidance. You convincingly conveyed a spirit of curiosity in regard to research and excitement in regard to science. Your richness of knowledge, dedication to research and integrity will inspire me for my whole life. Sincerely thank you for always giving me room for making mistakes and freedom to pursue and implement the ideas about the research work and career development.

I also want to send my deepest gratitude to my co-advisor, Professor Kamran Khan. I will never forget your help on solving divergence issues in FEA software, whenever I had what kinds of problems about research, you were always so patient to help me sort out the ideas and provide valuable discussions. Without your support, I cannot complete my research so smoothly.

I would like to thank Professor Alan Freed and Professor Sevan Goenezen and Jun Kameoka for serving as my committee members. You are always so kind whenever I need help from you.

I want to thank my friends, lab mates and all people I met during the past five years. Here I won't list all your names, but the acknowledgement for your help is sent from my heart and you are very important for me.

Finally, I want to send my special thanks to my family members. Thank my parents for unconditional support and understanding and everything you have done for me and for giving me so much love, understanding, encouragement and tolerance. Love you all.

## TABLE OF CONTENTS

ABSTRACT.....	II
ACKNOWLEDGEMENTS.....	III
CHAPTER I INTRODUCTION.....	1
1.1 Current research on soft material.....	1
1.2 Constitutive Models for Soft Materials.....	6
1.3 Research Objectives.....	10
CHAPTER II CONSTITUTIVE MODELS FOR NONLINEAR ELASTIC AND VISCOELASTIC MATERIAL RESPONSE.....	19
2.1 Constitutive model for isotropic and anisotropic material.....	19
2.2 Implementation of the material model in 3D continuum elements.....	22
2.3 Implementation of the material model for shell elements.....	23
2.4 viscoelastic constitutive model.....	25
2.4.1 Gent based QLV model.....	23
2.4.2 Anisotropic quasi-linear viscoelastic model.....	23
CHAPTER III NUMERICAL EXAMPLES.....	30
3.1 Uniaxial tension.....	30
3.2 Equibiaxial tension.....	33
3.3 Inflation of a spherical balloon.....	37
3.4 Circular Pneumatic Actuated soft Micromold (cPASMO).....	39
3.4.1 Fabrication of cPASMO.....	39
3.4.2 Modeling of cPASMO.....	41
3.4.3 Results of cPASMO.....	44
3.5 Numerical analysis of blood vessel from brain aneurysm model.....	48
3.6 Microhands model.....	50
3.6.1 Experiment work.....	51
3.6.2 Modeling and simulation.....	53
CHAPTER IV MECHANICAL RESPONSE OF SOFT COMPOSITE.....	57
4.1 Uniaxial response of elastic soft composites.....	58
4.2 Uniaxial response of viscoelastic soft composites.....	87
4.3 Structural Analysis.....	88
CHAPTER V CONCLUSION AND FUTURE WORK.....	104
REFERENCES.....	106

# CHAPTER I

## INTRODUCTION

### **1.1 Current research on soft material**

Soft materials, such as silicone rubbers and PDMS, are widely used in a number of engineering applications due to their relatively lightweight and compliant characteristics. They are easily fabricated to various shapes and sizes at a relatively low cost and can be fast actuated with small stimuli. These materials are now a backbone for soft robotics applications. Some of these silicone rubbers are biocompatible, making them appealing for biomedical devices and implants.

For example, biomedical Micro-Electro-Mechanical Systems (BioMEMS) are being used for patient diagnosis, monitoring and therapy[1], such as microorganisms used as biosensor for monitoring environmental pollutants[2] and serving as a valve for releasing preloaded drugs [3]. In BioMEMS field, soft robots have become prevalent in micro surgery and medical tasks because they allow for smooth and precise motions that relieve uncomfortable feeling to the patients.

Traditional robots are rigid structures usually composed of metal, and the motions are based on flexible joints that have a limited number of degrees of freedom. These robots are typically used in manufacturing that requires repetitive and defined motion with high precision. The complicated control for stiff links of hard robotic structures make it difficult to perform delicate tasks in unstructured environment. The limitation has led to an emerging research area in soft robotics. Soft robots have been designed to have multiple-degree-of-freedom motions while maintaining their light-weight

characteristics. Typically, their motions and mechanisms are inspired by nature, i.e., mimicking motions and functional behaviors in animals and plant [4]. Biomechanics features of muscular-hydrostats has been introduced to describe several soft animal structures [5]. Examples of muscular hydrostats are given as squid arms and tentacles [5], octopus arm [6] and human tongue [7]. In another approach, researchers have developed hard robots based on soft animal structures. For examples, the trunk-like manipulator are composed of elastic elements connected by rigid links which powered by electric engine[8].

Soft robots are typically composed of elastomeric structural components without any rigid internal skeletons, making them significantly flexible. Soft robots have advantages over hard hyper-redundant robots in that: (1) They provide multiple degrees of freedom. (2) Actuating complicated motions with small stimuli[9]. (3) They perform delicate tasks and manipulate fragile objects with complex geometry[10].

Most soft robots use electroactive polymer (EAP) and pneumatic artificial muscle (PAM) actuators [4]. EAP is suitable for soft robot due to low weight, pliability and large actuation strain[11]. However, the limitation of the EAP actuation capability is that a high actuation voltage is needed to produce large strains[4]. Applying high voltages for actuation is often time impractical.

PAMs, pneumatic soft actuators, consist of thin, flexible and tubular membrane. They are well-developed soft actuators that are capable of providing a large displacement as well as a large force actuated by a deformation of the elastomeric pneumatic networks under a pressurization. Suzumori et al. developed a microactuator

driven by an electro-pneumatic system made of fiber-reinforced rubber[12]. The model has three chambers which are controlled separately by valve to bend. Tsukagoshi et al. introduced the Active Hose which consist of a spiral tube similar to elephant trunk-like manipulator to generate bending [13]. Menciassi et al. developed model for micro-endoscopy which have two actuators that one clamper to stick to locomotion and one extensor pneumatically driven for positive displacement[14]. Pritts and Rahn developed a manipulator that consist of two section with 6-8 opposing contracting and extending actuator in each section to provide two-axis bending[15]. Suzumori et al. developed a bending optimal pneumatic rubber actuator applied for manta swimming [16].

Despite recently fast development in soft robotics, which focus mainly on understanding the kinematic mechanisms and motion control, little attention is given to the deformation of the soft structures trigger by various stimuli. Current challenges in developing soft robotics structures are attributed to: 1) lack of understanding of the deformation mechanisms in compliant heterogeneous bodies[17, 18] whose responses are highly nonlinear, anisotropic and time-dependent, and 2) lack of mathematical models and methods of solutions that describe kinematics and dynamics in compliant heterogeneous structures undergoing large deformations and configurational changes. This leads to trial and error experimental and design approaches in developing soft robots. There is a need for rigorous theoretical and computational studies that are capable of incorporating the influence of the deformation of soft and compliant structures and how it can be manipulated to achieve desirable shape reconfiguration



performance at the macroscopic level. As a first step, proper constitutive material models are needed for the soft materials.

Another application of silicone rubber is in tissue mimicking-phantom, which is often used to understand the mechanical responses of some biological tissues associated to diseased and healthy tissues. Silicone rubbers are also used for generating organ prototypes, which help physicians in treating the patients. For example, blockage arterial walls disrupt the blood flow, which is essential to maintain healthy tissues and functions. Stents are often used to treat blockage arterial walls. Another example, cerebral aneurysm is a very common disease that weakens the artery, causes a localized dilation ballooning of the artery, and has a high risk of rupture. The ruptured aneurysm leads to life threatening subarachnoid hemorrhage around the brain[19]. Surgery is required if rupture is expected after the wall stress reach the limits.

Stent is considered as an effective treatment for brain aneurysm by providing support and reinforcement for the wall of the aorta and avoiding the blood from entering the aneurysm. In the above examples, one can perform experimental tests to understand the response of tissue mimicking soft arterial walls under the presence of stents. For example, patient specific blood vessels can be 3D printed polymers [20] to create a replica of aneurysm. Experimental tests can then be performed on this replica to understand the fluid flow with and without stent. Thus, simulations on the interactions between stents and soft arterial walls can be performed prior to medical intervention. For this purpose, proper constitutive models for the tissues, which are highly nonlinear, anisotropic, and time-dependent, are necessary.

In addition, tissues and many biological materials are heterogeneous, which can complicate the modeling and simulation in understanding their deformation. In order to study the deformation mechanisms in tissues and biological materials, and designing engineering devices that mimic biological materials, it is often necessary to understand the mechanical responses of soft materials with embedded heterogeneities. Experiment [21] has been conducted to develop a soft composite material model to model anisotropic tissue. The paper investigates the effect of fiber volume fraction, fiber number and spacing on mechanical behavior of soft composite. Chanda [22] investigate simulate two-layer with different fiber angle in the heart to investigate the pumping efficiency of the heart both experimentally and analytically (ANSYS finite element software). Moreira and Nunes [23] fabricated soft composite specimens with one family of unidirectional fibers to investigate the influence of fiber orientation on under simple shear. Yousefsani et al. [24] present analytical solution for white matter tissue considered as a transversely isotropic composites made of axonal fibers in the framework of nonlinear soft composites mechanics. Since soft composites have been considered to study behaviors of biological tissues, they are also expected to be applicable for soft robotic structures, e.g., PAM.

Holzapfel and Gasser [25] extended anisotropic formulation to viscoelastic response of fiber-reinforced composites at finite strains and implemented the equations into a FE program. Nguyen et al. [26] developed a constitutive model for anisotropic and viscoelastic soft fiber composites considering different viscoelastic behavior of fiber and matrix and allowed the composite's model parameters to be involved in the

properties of matrix and fibers. There are limited studies in the literature on modeling the time-dependent characteristic of soft matrix and elastic behavior of fiber in soft composite.

## 1.2 Constitutive Models for Soft Materials

There have been constitutive material models formulated for describing nonlinear elastic response of isotropic materials, undergoing large deformations. Many of these models have been extended for including anisotropic and/or time-dependent behaviors. For example, Neo-Hookean is one of the most common nonlinear elastic models, discussed in 1943 by Treloar, which has similarity to Hooke's law in linear elastic behavior. The strain energy density function for an incompressible neo-Hookean material is given by

$$W = \frac{\mu}{2}(I_1 - 3) \quad (1.1)$$

where  $\mu$  is initial shear modulus. Even though neo-Hookean model is widely used to capture soft material and nonlinear behavior of biological tissues [27-29], it is inadequate for capturing deformation at large strains[30]. Mooney-Rivlin model is a hyperelastic model with a linear combination of two invariants. The strain energy density function is as follows:

$$W = C_1(I_1 - 3) + C_2(I_2 - 3) \quad (1.2)$$

where  $C_1$  and  $C_2$  are material constants. Neo-Hookean model is obtained if  $C_2 = 0$ . The two parameters could not adequately capture large stretch. To fitted experiments on liver tissue, nine material constants like Mooney-Rivlin model is presented for stress-

strain curve[28] leading to complicated fitting parameter. To obtain good convergence of nonlinear response between analytical and experimental results, the hyperelastic material model generally involve several material constants, e.g. Ogden model. There are numerous sets of values of the material parameters which fit the experimental data for a wide range of stretch [31]. The material parameters calibrated from the uniaxial response do not necessarily predict the response from the biaxial loading particularly at larger stretch. In some models such as the Gent model the mismatches are rather small, but in other models such as the six parameter Ogden model and Arruda-Boyce model [32] large mismatches are seen. Simultaneously fitting material parameters for uniaxial and biaxial loadings can give good overall fits of the data. The basic Gent model gives theoretical three-dimensional predictions equivalence to the complex eight chain Arruda and Boyce model [33]. The empirical Gent model with only two parameters indicates the capability in describing soft material [34].

Several nonlinear elastic models for anisotropic materials have also been considered. Einstein et al. [35] applied invariant formulation for dispersed transverse isotropy in aortic heart valves. The constitutive equation accounts for a statistical dispersion of fibers and introduces a new invariant theory based on a novel closed-form ‘splay invariant’. Sun and Sacks [36] pointed out the numerical instability and convergence when implementing the above model into finite element code. The numerical instability is a result of a lack of convexity of the strain energy function and the condition number of material stiffness matrix higher than a prescribed value. Humphrey and Yin [37] proposed present a new constitutive formulation that combines

certain desirable features of two previously used approaches (phenomenological and microstructural) for anisotropic material. The Holzapfel-Gasser-Ogden (HGO) material model [38] is commonly used for modeling responses of fiber-reinforced systems in biological tissues, where two families of collagen fibers are arranged in symmetrical spirals in each layer of arteries. The advantage of this model is that the fibers and matrix are associated with the histology of arterial tissue and the material parameters can be experimentally determined. The strain energy function of HGO model with perfectly aligned fibers is given by

$$\begin{aligned}
W(\mathbf{C}) &= W_D(\bar{I}_1) + W_V(J) + W_{aniso}(\bar{I}_4, \bar{I}_6) \\
&= \frac{G}{2}(\bar{I}_1 - 3) + \frac{K}{2}(J - 1)^2 + \frac{K_1}{2K_2} \sum_{i=4,6} (e^{k_2(\bar{I}_i - 1)^2} - 1),
\end{aligned} \tag{1.3}$$

where  $K$  is the bulk modulus,  $G$  is the shear modulus.  $W_{aniso}(\bar{I}_4, \bar{I}_6)$  is the energy stored in the fibers.  $\bar{I}_4$  and  $\bar{I}_6$  are the pseudo-invariants of  $\bar{\mathbf{C}}$ ,  $\mathbf{a}_{04}$ , and  $\mathbf{a}_{06}$ , defined as

$$\bar{I}_4 = \mathbf{a}_{04} \cdot (\bar{\mathbf{C}}\mathbf{a}_{04}), \quad \bar{I}_6 = \mathbf{a}_{06} \cdot (\bar{\mathbf{C}}\mathbf{a}_{06}) \tag{1.4}$$

where  $\mathbf{a}_{04}$ , and  $\mathbf{a}_{06}$  are two unit vectors associated with the contribution of the collagen fiber family in the reference configuration. Since fibers are aligned perfectly in media layer and dispersed for the intima and adventitia, Gasser et al.[39] proposed a similar model for arterial with distributed collagen fiber orientations. However, the capability of experimental measurement of the fiber direction is still arguable, less complicated model based on perfectly aligned fibers are considered [40].

The soft biological tissues and rubber-like materials are viscoelastic in nature [41]. it is then necessary to consider a proper viscoelastic constitutive model to study the deformations of soft materials that are being used to mimic biological tissues and

for soft robotics that mimics functionality of biological systems. Several studies on investigating viscoelastic behaviors of soft materials and biological tissues have been reported. For example, Rashid et al. [42] performed stress relaxation tests in tension on porcine brain tissue that showed a stiffer response with increasing strain rates, indicating that viscoelastic models are necessary. Piolettia et al. [43] developed a framework based on elastic and viscoelastic potentials for large deformations. Limbert et al. [44] extent it to incorporate an explicit dependence of the invariants of the Cauchy-Green deformation rate tensor and structure tensors in the stress response. Holzapfel and Gasser [25] developed a anisotropic viscoelastic model as an extension of the isotropic convolution integral formulation developed by Holzapfel [45] to include a dependence of the equilibrium stress and overstress response on the invariants of the Cauchy-Green deformation and structure tensors. Bischoff [46] proposed a physically based rheological network constitutive model for capturing the anisotropic, viscoelastic, and orthotropic material behavior of biological soft tissue. In 1945 Green [47] proposed a pioneering constitutive model to describe the viscoelastic behavior of rubberlike polymers, based on the kinetic theory of rubber elasticity and a relaxation hypothesis. In later review publications, Lockett [48] listed a summary of the current constitutive models for rubber-like materials. Morman [49] also provided the contemporary nonlinear viscoelasticity for soft materials and their promising applications. The emphasis was again on constitutive equations. Schapery [50] put emphasis on constitutive theories as applied to nonlinear isotropic viscoelastic solids. Muliana [51] developed a new class of QLV model by Fung [52] expressing strain as

an integral of a nonlinear measure of stress in view of causality. Freed and Rajagopal [53] developed a fraction-order viscoelastic fiber model that incorporates the properties of biological fibers and their physical mechanism during deformations.

A quasi-linear viscoelastic (QLV) model was proposed by Fung [52] to describe the uniaxial elongation of biological soft tissue like muscles, ligaments and tendons. In that study, he assumed the relaxation rate is independent of the instantaneous local strain. The quasi-linear viscoelastic model is widely used today due to its simplicity to incorporate both nonlinearity (dependence of properties on load or strain) and time dependence (viscoelasticity) in a simplified integral model. The QLV model has also been used to model materials like the biomedical applications[54, 55], elastomeric polymers and rubbers [56, 57].

### **1.3 Research Motivations and Objectives**

Soft robotics are gaining popularity due to their many advantages, such as performing multiple degree-of-freedom motions while maintaining their light weight characteristics, easily maneuvering in complicated paths, and can be actuated with various non-mechanical stimuli, over the traditional robots. The inherent compliant characteristics of soft robots is appealing for many applications including biomedicine, defense, agriculture, rescue activities in disaster zones. Despite their promising benefits in many applications, there are still challenging scientific issues in the development of soft biomedical robots, owing to lacks of suitable materials, challenging motion and positioning controls with high accuracy and precision, and difficulties in integrating

sensors and actuators into the deformable systems as the sensor and actuator systems also deform with the reconfiguration of the body. Thus, continuous sensing and actuating will require information of the current deformation state of the body. It is noted that currently available control and modeling approaches are mostly derived based on the assumption of a kinematic chain of rigid links, which are not suitable for soft robots. Soft robots utilize polymer and elastomer-based materials, which exhibit nonlinear viscoelastic behaviors, and hence can influence the ability to precisely control the desired shape reconfigurations. For example, stress relaxation in the materials can alter the reconfigured shapes. It is also important for the soft robots to have sufficient load bearing ability while being compliant and flexible. It is imperative to address the above challenges, which in part is associated with the analyses and design of suitable materials, in order to accelerate the widespread applications of soft robots.

This study presents simulations of shape reconfigurations of soft and compliant systems, actuated by mechanical stimulus, which are relevant for soft robotics and understanding biomechanical of tissues of complex geometries. The main focus of this study is to understand the effect of nonlinear elastic and viscoelastic material behaviors on the shape reconfigurations of soft devices. In addition, the study also investigates the anisotropic and heterogeneous materials responses on the shape reconfigurations of the systems.

In this research, we considered both anisotropic and viscoelastic responses utilizing the Gent and HGO strain energy functions and QLV model due to their simplicity in the mathematical models and relatively small numbers of material constants. The



material model is implemented in the user material subroutine in ABAQUS finite element (FE) analysis. Both 3D continuum and shell elements are considered and both compressible and incompressible constraints are also studied.

The overall objective of this work is to understand the deformations of soft and compliant systems under various mechanical boundary conditions, which can guide the development of various soft devices and understanding of mechanical behaviors of biological tissues. We also extended the study for soft composites, incorporating elastic fibers and soft viscoelastic matrix. The soft composites are appealing for soft robotics applications.

## CHAPTER II

### CONSTITUTIVE MODELS FOR NONLINEAR ELASTIC AND VISCOELASTIC MATERIAL RESPONSE

This chapter presents nonlinear elastic and viscoelastic constitutive models for soft materials and their implementation within user material subroutine in ABAQUS finite element analysis. We consider both isotropic and anisotropic response of materials. The model consists of isotropic strain energy function of the Gent model and anisotropic strain energy of the HGO model. A quasi-linear single integral model is then considered to incorporate the viscoelastic responses. Parametric studies are performed to acquire a better understanding of the effect of material parameters such as different material fiber angles, relaxation time and the ratio of the relaxation modulus to the instantaneous modulus. Several examples of boundary value problems are presented.

#### **2.1 Constitutive model for isotropic and anisotropic elastic material responses**

This preliminary study introduces the necessary kinematics and balance equations. Let us consider any particle  $P$  belonging to an abstract body  $B$  placed in a three-dimensional space. Let the shape of the body  $B$  transform from the reference configuration  $\Omega_R(B)$  to the current configuration of the body  $\Omega_t(B)$  over some time interval  $[t_0, t]$ . Let us describe the deformation as one to one mapping and assign a function  $\chi$  to map points in the body from a reference configuration to the ones in the

current configuration at time  $t$ . For any particle  $P$  in the body, let  $\mathbf{X}$  be the position of the particle in undeformed reference configuration, and  $\mathbf{x}$  be the position at deformed current configuration, then the motion of the body is given as:

$$\mathbf{x} = \boldsymbol{\chi}(\mathbf{X}, t). \quad (2.1)$$

The strain energy is defined in terms of the deformation gradient  $\mathbf{F}$  expressed as

$$\mathbf{F}(\mathbf{X}, t) = \frac{\partial \boldsymbol{\chi}}{\partial \mathbf{X}}, \quad (2.2)$$

and the volume preserving part of deformation gradient  $\mathbf{F}$  is defined by  $\bar{\mathbf{F}} = J^{-1/3} \mathbf{F}$ , and  $J$ , the volume change, is  $J = \det \mathbf{F}$ . For incompressible materials, the volume change is one.

The deviatoric stretch matrix of  $\bar{\mathbf{F}}$  is given as:

$$\mathbf{B} = \mathbf{F} \cdot \mathbf{F}^T = J^{2/3} \bar{\mathbf{B}}, \quad \bar{\mathbf{B}} = \bar{\mathbf{F}} \cdot \bar{\mathbf{F}}^T \quad (2.3)$$

$$\mathbf{C} = \mathbf{F}^T \cdot \mathbf{F} = J^{2/3} \bar{\mathbf{C}}, \quad \bar{\mathbf{C}} = \bar{\mathbf{F}}^T \cdot \bar{\mathbf{F}}$$

We adopt the decoupled form of a Helmholtz free-energy function  $W(\mathbf{C})$  for describing nonlinear elastic and anisotropic material model:

$$\begin{aligned} W(\mathbf{C}) &= W_D(\bar{I}_1) + W_V(J) + W_{aniso}(\bar{I}_4, \bar{I}_6) \\ &= -\frac{GJ_m}{2} \ln\left(\frac{J_m - \bar{I}_1 + 3}{J_m}\right) - \frac{K}{2} \ln(J) + \frac{K}{2} \frac{J^2 - 1}{2} + \frac{K_1}{2K_2} \sum_{i=4,6} (e^{k_2(\bar{I}_i - 1)^2} - 1), \end{aligned} \quad (2.4)$$

where  $W(\mathbf{C})$  is the strain energy per unit of reference volume, with  $W_D(\bar{I}_1)$  as its deviatoric part,  $W_V(J)$  as its volumetric part, and  $W_{aniso}(\bar{I}_4, \bar{I}_6)$  as its anisotropic part.

$W_D(\bar{I}_1)$  and  $W_{aniso}(\bar{I}_4, \bar{I}_6)$  are a purely isochoric isotropic Gent model and isochoric anisotropic free-energy contribution of the HGO model, respectively:

$$W_D(\bar{I}_1) = -\frac{GJ_m}{2} \ln\left(\frac{J_m - \bar{I}_1 + 3}{J_m}\right), \quad (2.5)$$

$$W_{aniso}(\bar{I}_4, \bar{I}_6) = \frac{K_1}{2K_2} \sum_{i=4,6} (e^{k_2(\bar{I}_i-1)^2} - 1).$$

A slightly compressible Gent hyperelastic free energy, having two parameter empirical constitutive model, is used for the hyperelastic volumetric and isochoric isotropic terms of the isotropic part of constitutive model. The advantage of the model is to capture strain-stiffing at large strains, which are experimentally observed in soft materials. The model reduces to isotropic material response as a special case. In formulating the model, we separate the volumetric and deviatoric part of the constitutive equation for the finite element implementation in order to avoid numerical problems such as element locking.  $W_v(J)$  denotes a purely volumetric contribution represented by the slightly compressible Gent hyperelastic model given by

$$W_v(J) = -\frac{K}{2} \ln(J) + \frac{K}{2} \frac{J^2 - 1}{2}. \quad (2.5)$$

Some differential formulas have been used in above:

$$\begin{aligned} \frac{\partial W_J}{\partial J} &= -\frac{K}{2} \frac{1}{J} + \frac{KJ}{2}, \quad \frac{\partial^2 W_J}{\partial J^2} = \frac{K}{2} + \frac{K}{2} \frac{1}{J^2}, \quad \frac{\partial J}{\partial \mathbf{C}} = -\frac{1}{2} \mathbf{J} \mathbf{C}^{-1} \\ \frac{\partial^2 J}{\partial \mathbf{C} \partial \mathbf{C}} &= \frac{1}{2} \left[ \frac{1}{2} \mathbf{J} \mathbf{C}^{-1} \otimes \mathbf{C}^{-1} - \mathbf{J} \mathbf{C}^{-1} \odot \mathbf{C}^{-1} \right] \end{aligned} \quad (2.7)$$

The second Piola-Kirchhoff stress tensor is prescribed as

$$\begin{aligned} \mathbf{S} &= 2 \frac{\partial W_D}{\partial \mathbf{C}} + 2 \frac{\partial W_J}{\partial \mathbf{C}} = 2 \left( \frac{\partial W_D}{\partial \bar{I}_1} \frac{\partial \bar{I}_1}{\partial \mathbf{C}} + \frac{\partial W_J}{\partial J} \frac{\partial J}{\partial \mathbf{C}} \right) \\ &= \frac{GJ_m}{J_m - \bar{I}_1 + 3} J^{-2/3} \left( \mathbf{I} - \frac{1}{3} \text{tr} \mathbf{C} \mathbf{C}^{-1} \right) + \frac{KJ}{2} \left( J - \frac{1}{J} \right) \mathbf{C}^{-1} \end{aligned} \quad (2.8)$$

Then by considering the anisotropy, we can get the stress at the current configuration:

$$\begin{aligned}
\mathbf{S} &= 2 \left( \frac{\partial W_D}{\partial I_1} \frac{\partial \bar{I}_1}{\partial \mathbf{C}} + \frac{\partial W_V}{\partial J} \frac{\partial J}{\partial \mathbf{C}} + \frac{\partial W_{aniso}}{\partial I_4} \frac{\partial \bar{I}_4}{\partial \mathbf{C}} + \frac{\partial W_{aniso}}{\partial I_6} \frac{\partial \bar{I}_6}{\partial \mathbf{C}} \right) \quad (2.9) \\
&= \frac{GJ_m}{J_m - \bar{I}_1 + 3} J^{-2/3} (\mathbf{I} - \frac{1}{3} \text{tr} \mathbf{C} \mathbf{C}^{-1}) + \frac{KJ}{2} (J - \frac{1}{J}) \mathbf{C}^{-1} \\
&\quad + 2K_1 \sum_{i=4,6} (I_i - 1) e^{K_2(I_i-1)^2} a_{0i} \otimes a_{0i}
\end{aligned}$$

The Cauchy stress tensor can be simply found by using a push forward operation. The Cauchy stress for the 3D continuum is given by

$$\boldsymbol{\sigma} = J^{-1} \mathbf{F} \frac{\partial W}{\partial \mathbf{F}} = \frac{GJ_m}{J(J_m - \bar{I}_1 + 3)} (\bar{\mathbf{B}} - \frac{1}{3} \bar{I}_1 \mathbf{I}) + \frac{K}{2} (J - \frac{1}{J}) \mathbf{I} + 2W'_{aniso} a_i \otimes a_i \quad (2.10)$$

## 2.2 Implementation of the material model in three-dimensional continuum elements

For the UMAT implementation, the material tangent stiffness matrix can be determined in a similar manner as the Cauchy stress tensor. The elasticity tensor is

$$\mathbb{C}^{\tau c} = 4 \frac{\partial^2 W}{\partial \mathbf{C} \partial \mathbf{C}} \quad (2.11)$$

The isotropic contribution to  $\mathbb{C}^{\tau c}$  are given by Eqs. (2.5) and (2.6)

$$\begin{aligned}
\mathbb{C}_D &= 4 \left( \frac{\partial^2 W_D}{\partial \bar{I}_1^2} \frac{\partial \bar{I}_1}{\partial \mathbf{C}} \otimes \frac{\partial \bar{I}_1}{\partial \mathbf{C}} + \frac{\partial W_D}{\partial \bar{I}_1} \frac{\partial^2 \bar{I}_1}{\partial \mathbf{C} \partial \mathbf{C}} \right) \quad (2.12) \\
&= \frac{2GJ_m}{(J_m - \bar{I}_1 + 3)^2} J^{-4/3} (\mathbf{I} - \frac{1}{3} \text{tr} \mathbf{C} \mathbf{C}^{-1}) \otimes (\mathbf{I} - \frac{1}{3} \text{tr} \mathbf{C} \mathbf{C}^{-1}) \\
&\quad + \frac{2GJ_m}{(J_m - \bar{I}_1 + 3)} \left( \frac{1}{3} \bar{I}_1 \mathbf{C}^{-1} \odot \mathbf{C}^{-1} + \frac{1}{9} \bar{I}_1 \mathbf{C}^{-1} \otimes \mathbf{C}^{-1} - \frac{1}{3} J^{-2/3} (\mathbf{I} \otimes \mathbf{C}^{-1} + \mathbf{C}^{-1} \otimes \mathbf{I}) \right)
\end{aligned}$$

$$\begin{aligned}
\mathbb{C}_V &= 4 \left( \frac{\partial^2 U}{\partial \bar{I}_1^2} \frac{\partial \bar{I}_1}{\partial \mathbf{C}} \otimes \frac{\partial \bar{I}_1}{\partial \mathbf{C}} + \frac{\partial U}{\partial J} \frac{\partial^2 J}{\partial \mathbf{C} \partial \mathbf{C}} \right) \quad (2.13) \\
&= KJ^2 \mathbf{C}^{-1} \otimes \mathbf{C}^{-1} + (K - KJ^2) \mathbf{C}^{-1} \odot \mathbf{C}^{-1}
\end{aligned}$$

The following formula has been used in the push-forward operation

$$\mathbb{C}^{\tau Z-J} = \mathbb{C}^{\tau c} + \frac{1}{2} (\delta_{ik} \tau_{jl} + \tau_{ik} \delta_{jl} + \delta_{il} \tau_{jk} + \tau_{il} \delta_{jk}) \mathbf{e}_i \otimes \mathbf{e}_j \otimes \mathbf{e}_k \otimes \mathbf{e}_l \quad (2.14)$$

$$\mathbb{C}_{ijkl}^{\tau c} = F_{ip} F_{jq} F_{kr} F_{ls} \mathbb{C}_{pqrs}$$

The isotropic contributions to  $\mathbb{C}_{ijkl}^{\tau c}$  are given by

$$\begin{aligned} \mathbb{C}^{\tau Z-J} &= \mathbb{C}^{\tau c} + \frac{1}{2} (\delta_{ik} \tau_{jl} + \tau_{ik} \delta_{jl} + \delta_{il} \tau_{jk} + \tau_{il} \delta_{jk}) \mathbf{e}_i \otimes \mathbf{e}_j \otimes \mathbf{e}_k \otimes \mathbf{e}_l \\ &= \frac{2GJ_m}{(J_m - I_1 + 3)^2} (\bar{\mathbf{B}} \otimes \bar{\mathbf{B}} - \frac{1}{3} \bar{I}_1 \bar{\mathbf{B}} \otimes \mathbf{I} - \frac{1}{3} \bar{I}_1 \mathbf{I} \otimes \bar{\mathbf{B}} + \frac{1}{9} \bar{I}_1^{-2} \mathbf{I} \otimes \mathbf{I}) + KJ^2 \mathbf{I} \otimes \mathbf{I} \\ &\quad + \frac{2GJ_m}{(J_m - I_1 + 3)} \left( \frac{1}{9} \bar{I}_1 \mathbf{I} \otimes \mathbf{I} - \frac{1}{3} (\mathbf{I} \otimes \bar{\mathbf{B}} + \bar{\mathbf{B}} \otimes \mathbf{I}) \right) + \frac{GJ_m}{(J_m - I_1 + 3)} (\mathbf{I} \odot \bar{\mathbf{B}} + \bar{\mathbf{B}} \odot \mathbf{I}) \end{aligned} \quad (2.15)$$

The anisotropic contribution to  $\mathbb{C}_{ijkl}^{MZ-J}$  for the model is given as

$$\begin{aligned} \mathbb{C}_{ijkl}^{MZ-J} &= \frac{\partial \dot{J} \sigma}{\partial D} \\ &= 2K_1 e^{K_2(I_n - 1)^2} [(2 + 4K_2(I_n - 1)^2) a_i a_j a_k a_l + (I_n - 1)(\delta_{ij} a_k a_l + \delta_{jk} a_i a_l)] \end{aligned} \quad (2.16)$$

We combine both isotropic and anisotropic contributions, and express the formula as:

$$\begin{aligned} \mathbb{C}_{ijkl}^{MZ-J} &= \frac{2GJ_m}{J(J_m - I_1 + 3)^2} (\bar{B}_{ij} \bar{B}_{kl} - \frac{1}{3} \bar{I}_1 \bar{B}_{ij} \delta_{kl} - \frac{1}{3} \bar{I}_1 \delta_{ij} \bar{B}_{kl} + \frac{1}{9} \bar{I}_1^{-2} \delta_{ij} \delta_{kl}) + KJ^2 \delta_{ij} \delta_{kl} \\ &\quad + \frac{2GJ_m}{J(J_m - I_1 + 3)} \left( \frac{1}{9} \bar{I}_1 \delta_{ij} \delta_{kl} - \frac{1}{3} \delta_{ij} \bar{B}_{kl} - \frac{1}{3} \bar{B}_{ij} \delta_{kl} \right) + \frac{GJ_m}{2J(J_m - I_1 + 3)} (\delta_{ik} \bar{B}_{jl} + \bar{B}_{ik} \delta_{jl} + \bar{B}_{jk} \delta_{il} + \bar{B}_{il} \delta_{jk}) \\ &\quad + 2K_1 e^{K_2(I_n - 1)^2} [(2 + 4K_2(I_n - 1)^2) a_i a_j a_k a_l + (I_n - 1)(\delta_{ij} a_k a_l + \delta_{jk} a_i a_l)] \end{aligned} \quad (2.17)$$

### 2.3 Implementation of the material model for shell element

Since some of the structures or devices are of very thin walls, we modified the material model suitable for shell elements. The 3D Cauchy stress is given in the previous section.

The deformation gradient  $\mathbf{F}$  is

$$\mathbf{F} = \begin{bmatrix} F_{11} & F_{12} & 0 \\ F_{21} & F_{22} & 0 \\ 0 & 0 & F_{33} \end{bmatrix} = \begin{bmatrix} F_s & 0 \\ 0 & F_{33} \end{bmatrix} \quad (2.18)$$

where direction 3 is the normal to the shell. Incompressibility is assumed, so

$J = \det \mathbf{F} = 1$ . The left Cauchy-Green tensor becomes

$$\mathbf{B} = \begin{bmatrix} \mathbf{F}_c \mathbf{F}_c^T & 0 \\ 0 & F_{33}^2 \end{bmatrix} \quad (2.19)$$

Due to a plane stress condition,  $\sigma_{33} = 0$ , the pressure can be calculated as

$$p = -\frac{GJ_m}{J_m - I_1 + 3} B_{33} \quad (2.20)$$

The Cauchy stress in shell is

$$\sigma_s = \frac{GJ_m}{J(J_m - I_1 + 3)} (\mathbf{B} - B_{33} \mathbf{I}) + 2W'_{aniso} a_i \otimes a_i \quad (2.21)$$

So only three stress components in the plane of the sheet need to be provided. The rate of the deformation gradient is given by

$$\dot{\mathbf{F}} = \mathbf{L}\mathbf{F} = \begin{bmatrix} L_s F_s & 0 \\ 0 & L_{33} F_{33} \end{bmatrix} \quad (2.22)$$

where the spatial velocity gradient  $\mathbf{L}$  is the combination of rate of deformation tensor  $\mathbf{D}$  and the spin tensor  $\mathbf{W}$ . Because  $D_{33} = -(\mathbf{D}_{11} + \mathbf{D}_{22})$ , we could obtain:

$$\dot{F}_{33} = -\frac{(\mathbf{D}_{11} + \mathbf{D}_{22})}{\det F_s} \quad (2.23)$$

The tangent modulus related to the Jaumann stress rate is calculated as

$$\begin{aligned} \mathbb{C}_{ijkl}^{MZ-J} &= \frac{\partial \dot{J}\sigma}{\partial D} \quad (2.24) \\ &= \frac{4GJ_m}{(J_m - I_1 + 3)^2} (B_{ij} B_{kl} - B_{33} \delta_{ij} B_{kl} - 2B_{ij} \delta_{kl} \frac{F_{33}}{\det F_s} + 2B_{33} \delta_{ij} \delta_{kl} \frac{F_{33}}{\det F_s}) \\ &\quad + \frac{2GJ_m}{J(J_m - I_1 + 3)} \left( B_{ij} \delta_{kl} - B_{33} \delta_{ij} \delta_{kl} - \frac{4F_{33}}{\det F_s} \delta_{ij} \delta_{kl} \right) \\ &\quad + \frac{GJ_m}{J_m - I_1 + 3} (\delta_{ik} B_{jl} + B_{ik} \delta_{jl} + B_{jk} \delta_{il} + B_{il} \delta_{jk}) \\ &\quad + 2K_1 e^{K_2(I_n - 1)^2} [(2 + 4K_2(I_n - 1)^2) a_i a_j a_k a_l + (I_n - 1)(\delta_{il} a_k a_j + \delta_{jl} a_i a_k)] \end{aligned}$$

Since ABAQUS uses the Green-Naghdi stress rate for shell elements, we need to use the relation between the Jaumann rate and Green-Naghdi rate in the following manner:

$$(\overset{\nabla}{\mathbb{C}})_{ijkl}^{\tau c} = \overset{\circ}{\mathbb{C}}_{ijkl} + \Lambda_{iakl} \tau_{aj} + \Lambda_{ajkl} \tau_{ia} \quad (2.25)$$

where  $\Lambda_{ijkl}$  are the components of a material-dependent fourth-order tensor and  $\tau_{ia}$  is the Kirchhoff stress. From the expression in Mehradadi and Nemat-Nasser [58],  $\Lambda_{ijkl}$  can be calculated as

$$\mathbf{W} - \boldsymbol{\Omega} = \boldsymbol{\Lambda}(\mathbf{V}) : \mathbf{D} \quad (2.26)$$

$$\boldsymbol{\Lambda}(\mathbf{V}) : \mathbf{D} = \frac{1}{I_V \Pi_V - III_V} \{ I_V^2 (\mathbf{V}\mathbf{D} - \mathbf{D}\mathbf{V}) - I_V (\mathbf{V}^2 \mathbf{D} - \mathbf{D}\mathbf{V}^2) + \mathbf{V}^2 \mathbf{D}\mathbf{V} - \mathbf{V}\mathbf{D}\mathbf{V}^2 \}$$

where  $\boldsymbol{\Omega}$  is defined as  $\boldsymbol{\Omega} = \dot{\mathbf{R}} \mathbf{R}^T$ ;  $\mathbf{V}$  and  $\mathbf{R}$  are left stretch tensor the rotation tensor in the polar decomposition of  $\mathbf{F}$ .  $I_V$ ,  $\Pi_V$  and  $III_V$  are principal invariants of  $\mathbf{V}$ . By substituting Eqs. (2.24) and (2.26) to Eq. (2.25), we could obtain the final Green-Naghdi tangent moduli.

## 2.4 Viscoelastic constitutive model

Jennifer et al. [59] carried out mechanical measurements on three soft materials which presents the stress relaxation behavior and temperature can impact the soft material's mechanical response. In order to better understand the material behavior of soft material accurately, it's worthwhile to model a viscoelastic response by adopting the quasi-linear viscoelasticity framework to model the soft material.

Fung [52] introduced a quasi-linear viscoelastic (QLV) model to capture the response of uniaxial tension of biological soft materials by assuming the relaxation rate is independent of the instantaneous local strain. The QLV model nowadays is widely applied in many applications[54-56, 60] as a simple way to incorporate both



nonlinearity (dependence of properties on load or strain) and time dependence (viscoelasticity) in a simple linear convolution integral.

In term of strain history, the stress is given by

$$\mathbf{S}(t) = \int_0^t \mathbf{G}(t-s) \frac{d\mathbf{S}^e(\mathbf{E}(s))}{ds} ds \quad (2.27)$$

$\mathbf{S}(t)$  is the second Piola Kirchhoff stress,  $\mathbf{G}(t)$  is the reduced relaxation function and  $\mathbf{S}^e(\mathbf{E}(s))$  is the instantaneous elastic response in terms of Green-St. Venant strain.

In the QLV model, it is assumed that the stress depends linearly on the time history, and the relaxation function does not depend on the deformation state, and response at current time can be approximated by a linear combination of responses of multiple deformation inputs applied at different time histories. We used the 2<sup>nd</sup> Piola-Kirchhoff stress, that the physical quantities should be independent of observer transformations, and expressed by decomposition achieved by split the deviatoric and hydrostatic components of the 2<sup>nd</sup> Piola-Kirchhoff stress:

$$\mathbf{S} = \mathbf{S}_D + \mathbf{S}_H = \int_{-\infty}^t \mathbf{D}(t-s) \frac{\partial}{\partial s} \mathbf{S}_D^e(s) ds + \int_{-\infty}^t \mathbf{H}(t-s) \frac{\partial}{\partial s} \mathbf{S}_H^e(s) ds \quad (2.28)$$

where  $\mathbf{S}_D^e, \mathbf{S}_H^e$  are the corresponding terms of Cauchy stress to the 2<sup>nd</sup> Piola-Kirchhoff stress, which are given by the following relations  $\mathbf{S}_D^e = \mathbf{J}\mathbf{F}^{-1}\mathbf{T}_D^e\mathbf{F}^{-T}$  and  $\mathbf{S}_H^e = \mathbf{J}\mathbf{F}^{-1}\mathbf{T}_H^e\mathbf{F}^{-T}$

where  $\mathbf{T}_D^e = \mathbf{T}^e - \frac{1}{3}tr(\mathbf{T}^e)\mathbf{I}$ ,  $\mathbf{T}_H^e = \frac{1}{3}tr(\mathbf{T}^e)\mathbf{I}$  are the deviatoric and hydrostatic Cauchy

stress components, respectively.  $\mathbf{D}(t)$  and  $\mathbf{H}(t)$  are the associated reduced tensorial relaxation operators,  $J$  is the  $\det(\mathbf{F})$  defining the volume change. Pre-multiplying by  $J^{-1}\mathbf{F}$  and post-multiplying by  $\mathbf{F}^T$  to give the Cauchy stress:

$$\begin{aligned} \mathbf{T}(t) = & J^{-1} \mathbf{F}(t) \left( \int_{-\infty}^t \mathbf{D}(t-s) \frac{\partial}{\partial s} \mathbf{S}_D^e(s) ds \right) \mathbf{F}^T(t) \\ & + J^{-1} \mathbf{F}(t) \left( \int_{-\infty}^t \mathbf{H}(t-s) \frac{\partial}{\partial s} \mathbf{S}_H^e(s) ds \right) \mathbf{F}^T(t) \end{aligned} \quad (2.29)$$

Integrating by parts gives,

$$\begin{aligned} \mathbf{T}(t) = & J^{-1} \mathbf{F}(t) (\mathbf{S}_D^e(t) + \int_0^t \frac{d\mathbf{D}(t-s)}{d(t-s)} \mathbf{S}_D^e(s) ds) \mathbf{F}^T(t) \\ & + J^{-1} \mathbf{F}(t) (\mathbf{S}_H^e(t) + \int_0^t \frac{d\mathbf{H}(t-s)}{d(t-s)} \mathbf{S}_H^e(s) ds) \mathbf{F}^T(t) \end{aligned} \quad (2.30)$$

By considering incompressibility, i.e.  $J=1$ , the second term of (2.30) only contains the hydrostatic term which can represent the compressible deformation of the body, and reduces to

$$J^{-1} \mathbf{F}(t) (\mathbf{S}_H^e(t) + \int_0^t \frac{d\mathbf{H}(t-s)}{d(t-s)} \mathbf{S}_H^e(s) ds) \mathbf{F}^T(t) \rightarrow -p(t) \mathbf{I} \quad (2.31)$$

where  $p(t)$  is considered as a Lagrange multiplier. It refers to the indeterminate part of the stress due to incompressibility. Therefore, (2.30) can be reduced to

$$\mathbf{T}(t) = -p \mathbf{I} + \mathbf{F}(t) (\mathbf{S}_D^e(t) + \int_0^t \frac{d\mathbf{D}(t-s)}{d(t-s)} \mathbf{S}_D^e(s) ds) \mathbf{F}^T(t) \quad (2.32)$$

#### 2.4.1 Gent based QLV model

The second Piola-Kirchhoff stress of the quasi-linear viscoelastic model of an incompressible body is:

$$\mathbf{S} = \frac{KJ}{2} (J - \frac{1}{J}) \mathbf{C}^{-1} + \mathbf{S}_D^e(t) + \int_0^t \frac{d\mathbf{D}(t-s)}{d(t-s)} \mathbf{S}_D^e(s) ds \quad (2.33)$$

The total Cauchy stress is:

$$\boldsymbol{\sigma}(t) = \frac{K}{2} (J - \frac{1}{J}) \mathbf{I} + J^{-1} \mathbf{F}(t) (\mathbf{S}_D^e(t) + \int_0^t \frac{d\mathbf{D}(t-s)}{d(t-s)} \mathbf{S}_D^e(s) ds) \mathbf{F}^T(t) \quad (2.34)$$

The Jacobian is given as,

$$\begin{aligned}\mathbb{C}_D(t) &= 2 \frac{\partial \mathbf{S}_D(t)}{\partial \mathbf{C}(t)} = 2 \left[ \frac{\partial \mathbf{S}_D^e(t_n)}{\partial \mathbf{C}(t_n)} + \frac{t_n - t_{n-1}}{2} \left( \frac{d\mathbf{D}_a(t-s)}{d(t-s)} \Big|_{s=t_n} \frac{\partial \mathbf{S}_D^e(t_n)}{\partial \mathbf{C}(t_n)} \right) \right] \quad (2.35) \\ &= \left[ 1 + \frac{t_n - t_{n-1}}{2} \left( \frac{d\mathbf{D}_a(t-s)}{d(t-s)} \Big|_{s=t_n} \right) \right] \mathbb{C}_D^e(t)\end{aligned}$$

where  $\mathbb{C}_D^e(t)$  is the Jacobian for elastic terms shown above.

Expressing  $D(t)$  with one term Prony series, then we have:

$$\begin{aligned}D(t) &= \frac{\mu_\infty}{\mu_o} + \left(1 - \frac{\mu_\infty}{\mu_o}\right) e^{-t/\tau} \quad (2.36) \\ \frac{dD(t-s)}{d(t-s)} &= \left(1 - \frac{\mu_\infty}{\mu_o}\right) \left(-\frac{1}{\tau}\right) e^{-(t-s)/\tau}\end{aligned}$$

where  $\mu_{oi}$  and  $\mu_{\infty i}$  are the shear modulus and long-time shear modulus, respectively,

$\tau$  is their characteristic relaxation time.

The final Jacobian is shown as,

$$\begin{aligned}\mathbb{C}_{ijkl}^{MZ-J} &= KJ^2 \delta_{ij} \delta_{kl} \quad (2.37) \\ &+ \left(1 - \frac{\Delta t}{2\tau} \left(1 - \frac{\mu_\infty}{\mu_o}\right)\right) \left[ \frac{2GJ_m}{J(J_m - I_1 + 3)^2} (\bar{B}_{ij} \bar{B}_{kl} - \frac{1}{3} \bar{I}_1 \bar{B}_{ij} \delta_{kl} - \frac{1}{3} \bar{I}_1 \delta_{ij} \bar{B}_{kl} + \frac{1}{9} \bar{I}_1^2 \delta_{ij} \delta_{kl}) \right. \\ &+ \left. \frac{2GJ_m}{J(J_m - I_1 + 3)} \left( \frac{1}{9} \bar{I}_1 \delta_{ij} \delta_{kl} - \frac{1}{3} \delta_{ij} \bar{B}_{kl} - \frac{1}{3} \bar{B}_{ij} \delta_{kl} \right) \right] \\ &+ \frac{GJ_m}{2J(J_m - I_1 + 3)} (\delta_{ik} \bar{B}_{jl} + \bar{B}_{ik} \delta_{jl} + \bar{B}_{jk} \delta_{il} + \bar{B}_{il} \delta_{jk})\end{aligned}$$

## 2.4.2 Anisotropic quasi-linear viscoelastic model

If anisotropy of model is considered, only the elastic stress  $\mathbf{S}_D^e$  of equation (2.34)

and (2.37) need to be replaced by the anisotropic form which we have derived above.

By substituting equations (2.9) into equations (2.37), we can obtain:

$$\begin{aligned}
\mathbb{C}_{ijkl}^{MZ-J} &= KJ^2 \delta_{ij} \delta_{kl} & (2.38) \\
&+ \left(1 - \frac{\Delta t}{2\tau} \left(1 - \frac{\mu_\infty}{\mu_o}\right)\right) \left[ \frac{2GJ_m}{J(J_m - I_1 + 3)^2} (\bar{B}_{ij} \bar{B}_{kl} - \frac{1}{3} \bar{I}_1 \bar{B}_{ij} \delta_{kl} - \frac{1}{3} \bar{I}_1 \delta_{ij} \bar{B}_{kl} + \frac{1}{9} \bar{I}_1^2 \delta_{ij} \delta_{kl}) \right. \\
&+ \frac{2GJ_m}{J(J_m - I_1 + 3)} \left( \frac{1}{9} \bar{I}_1 \delta_{ij} \delta_{kl} - \frac{1}{3} \delta_{ij} \bar{B}_{kl} - \frac{1}{3} \bar{B}_{ij} \delta_{kl} \right) + \frac{GJ_m}{2J(J_m - I_1 + 3)} (\delta_{ik} \bar{B}_{jl} + \bar{B}_{ik} \delta_{jl} + \bar{B}_{jk} \delta_{il} + \bar{B}_{il} \delta_{jk}) \\
&\left. + 2K_1 e^{K_2(I_n - 1)^2} ((2 + 4K_2(I_n - 1)^2) a_i a_j a_k a_l + (I_n - 1)(\delta_{il} a_k a_j + \delta_{jl} a_i a_k)) \right]
\end{aligned}$$

CHAPTER III

FINITE ELEMENT IMPLEMENTATION VERIFICATION AND  
BOUNDARY VALUE PROBLEMS

In this chapter, numerical analyses are performed in order to examine the constitutive models and FE implementation. Several simple boundary value problems, such as uniaxial tension, equibiaxial test and inflation of a spherical balloon, are first considered and the numerical results are compared to the analytical solutions. The purpose is to test the numerical implementations of the models. Structural analyses are then conducted on more complex boundary conditions, e.g. PASMO, micro-hands, and blood vessels, in order to understand the overall response of the devices under mechanical stimulus.

### 3.1 Uniaxial tension

We first assume an incompressible isotropic material of a unit cube under uniaxial extension. The principal stretches are

$$\lambda_1 = \lambda; \lambda_2 = \lambda_3 = \frac{1}{\sqrt{\lambda}}; I_1 = \lambda^2 + \frac{2}{\lambda} \quad (3.1)$$

The principal stretch  $\lambda_1$  direction is orientated with loading direction. Three-dimensional continuum element is used. The non-zero Cauchy stress for an incompressible Gent model corresponding to the uniaxial stretch is

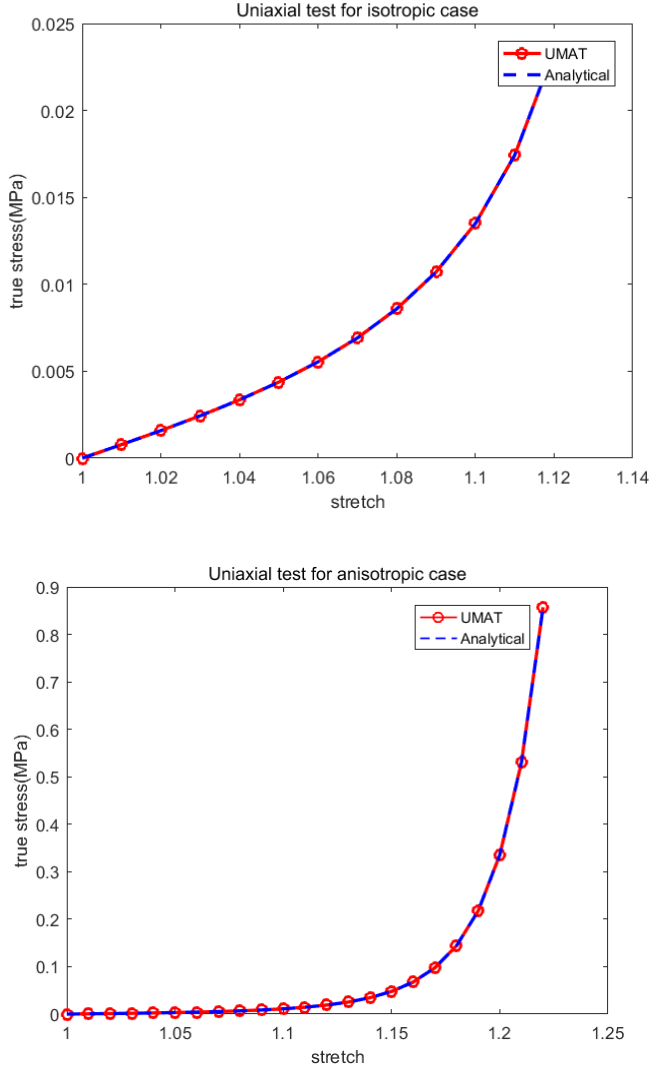
$$\sigma_{11} = \left(\lambda^2 - \frac{1}{\lambda}\right) \left(\frac{GJ_m}{J_m - I_1 + 3}\right) \quad (3.2)$$

In UMAT, we applied nearly incompressible material to eliminate convergence problems, and the material parameters of the Gent model are  $G = 0.026MPa$ ,  $J_m = 0.067$  and  $K=2000$ . With the relation of Poisson's ratio  $\nu = \frac{3K / G - 2}{6K / G + 2}$ , the initial  $\nu$  is greater than 0.49995.

For an anisotropic material, we assume single fiber direction and its longitudinal axis is along the loading direction. The uniaxial stress is present as:

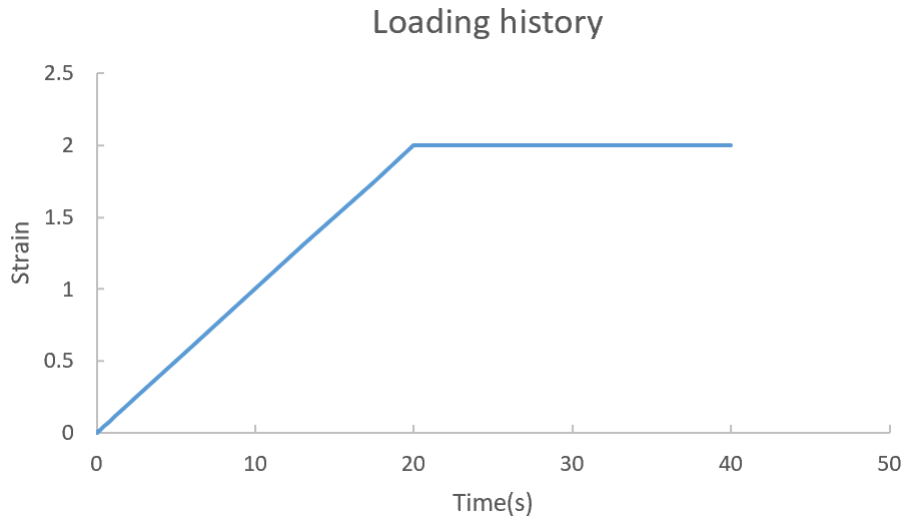
$$\sigma_{11} = \left(\lambda^2 - \frac{1}{\lambda}\right) \left(\frac{GJ_m}{J_m - I_1 + 3}\right) + 2K_1(I_4 - 1)e^{K_2(I_4 - 1)^2} \lambda^2 \quad (3.3)$$

The material parameters for the anisotropic case is  $\mu = 0.024MPa$ ,  $J_m = 0.9$ ,  $K = 2000$ ,  $K_1 = 0.8MPa$  and  $K_2 = 503.5$ . Figure 1 illustrates the stress versus stretch result of uniaxial test for isotropic and anisotropic models. The responses determined from the FE analyses of UMAT are in good agreements with the analytical solutions. From the figure 1, it is easy to notice the anisotropic case shows stiffer response, and there is significant variation in the true stress between isotropic case and anisotropic case. The reason of higher stress for anisotropic case is that the fibers restrain the tension of model for anisotropic case.

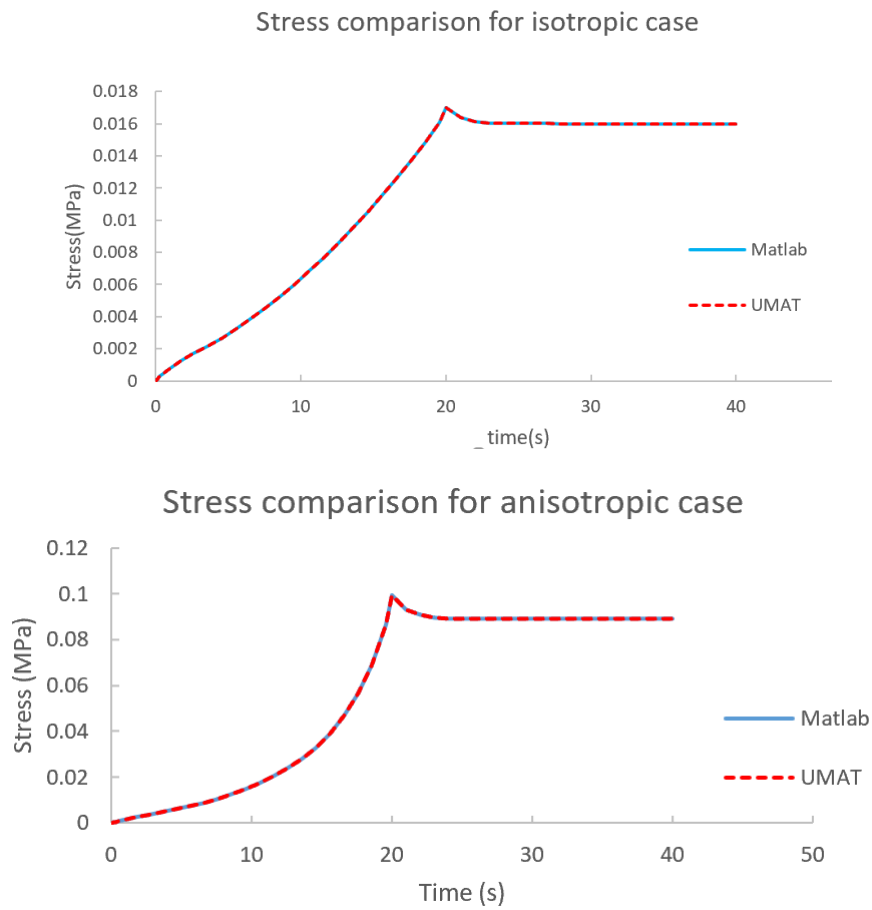


**Figure 1.** Stress vs. stretch curve for uniaxial tension: (a) Isotropic. (b) Anisotropic

Uniaxial tension loading is also tested for the nonlinear viscoelastic isotropic and anisotropic model. To consider the time dependent response of QLV model, we set up a loading history as shown in Fig. 2. The material properties of QLV model are  $\frac{\mu_\infty}{\mu_a} = 0.5$ ,  $\tau_a = 1s$ . The body is stretch along x direction for 20 seconds till the stretch ratio of 3 and then hold stretch unchanged for another 20 seconds. From figure 3, compared to isotropic case, the response for anisotropic case show stiffer curve in the first 20 seconds and same curve from 20 to 40 seconds.



**Figure 2.** Loading history for QLV model



**Figure 3.** Comparison of stress vs stretch between UMAT and Matlab under uniaxial tension for isotropic and anisotropic case



### 3.2 Equibiaxial test

The motion of equibiaxial test is described as

$$\lambda_1 = \lambda_2 = \lambda; \lambda_3 = \frac{1}{\lambda^2}; I_1 = 2\lambda^2 + \frac{1}{\lambda^4} \quad (3.4)$$

The Cauchy stresses for incompressible Gent model is given by

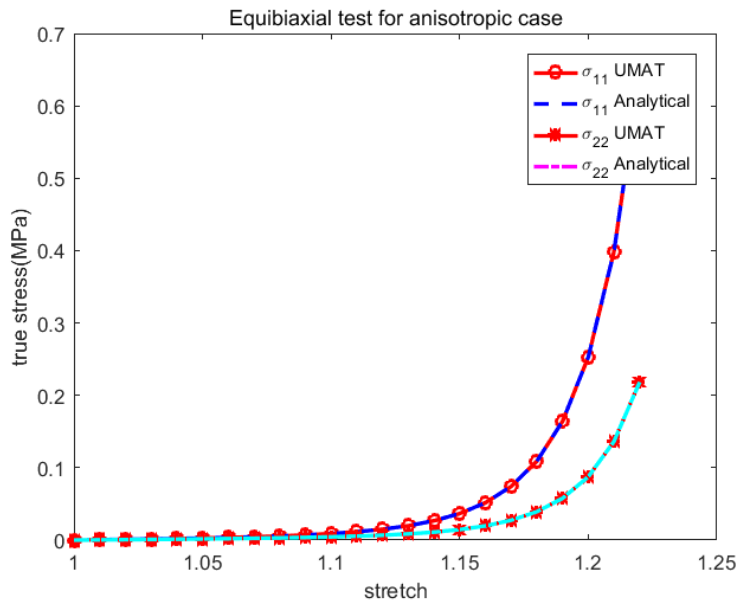
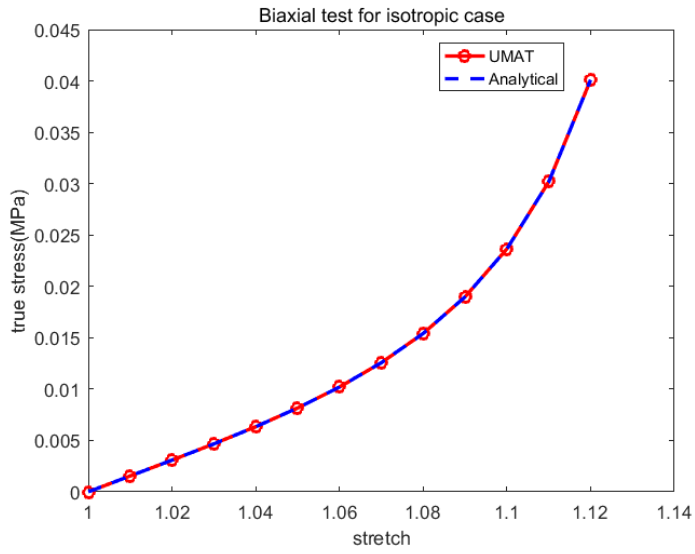
$$\sigma_{11} = \left(\lambda^2 - \frac{1}{\lambda^4}\right) \left(\frac{GJ_m}{J_m - I_1 + 3}\right) \quad (3.5)$$

For the anisotropic case, only single fibre direction is considered, and the direction between fiber and local 1-axis is 30 degrees.

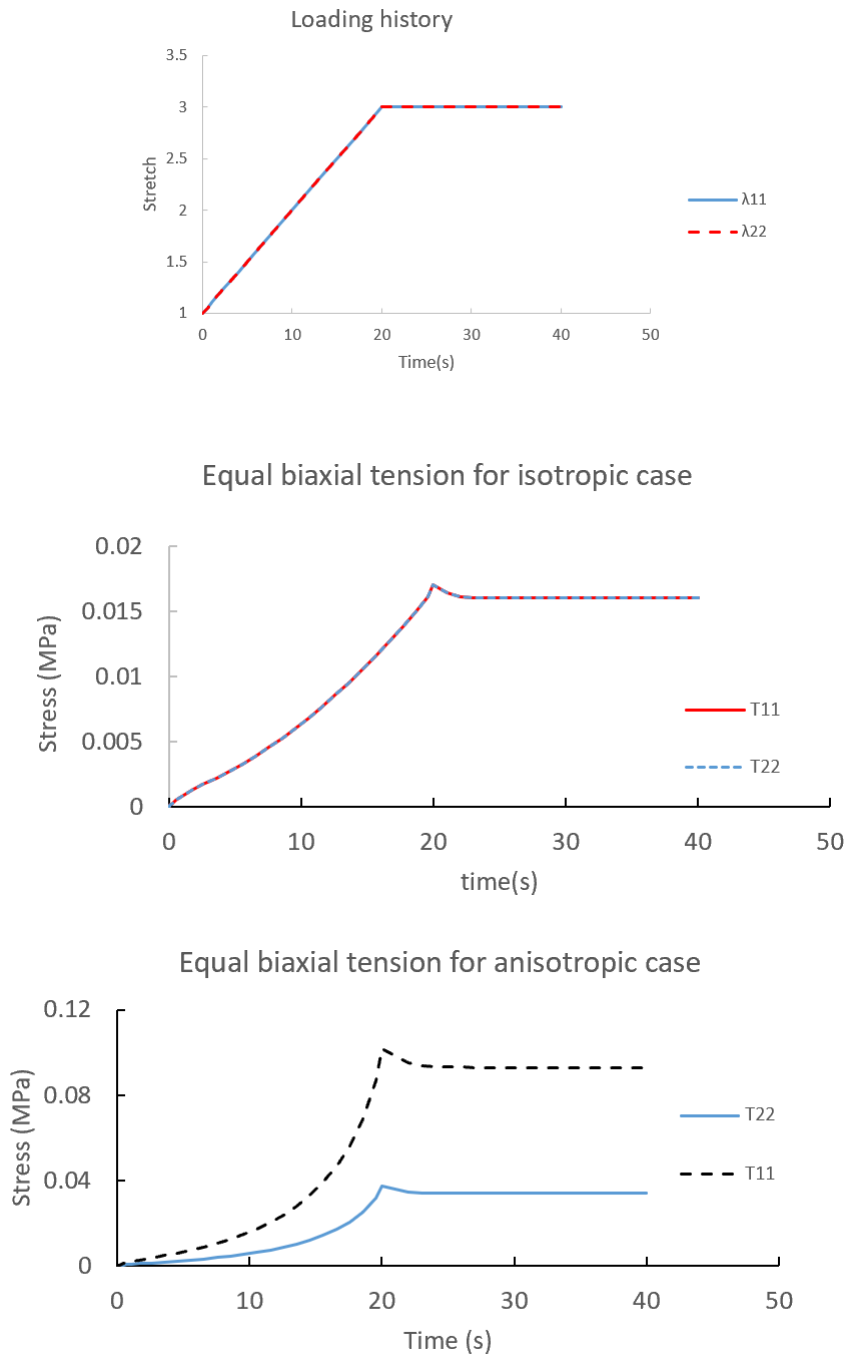
$$\sigma_{11} = \left(\lambda^2 - \frac{1}{\lambda}\right) \left(\frac{GJ_m}{J_m - I_1 + 3}\right) + 2K_1(I_4 - 1)e^{K_2(I_4 - 1)^2} \lambda^2 \cos^2 \varphi \quad (3.6)$$

$$\sigma_{22} = \left(\lambda^2 - \frac{1}{\lambda}\right) \left(\frac{GJ_m}{J_m - I_1 + 3}\right) + 2K_1(I_4 - 1)e^{K_2(I_4 - 1)^2} \lambda^2 \sin^2 \varphi$$

Figure 4 illustrates the response from the analytical and numerical simulation for biaxial tension. Three-dimensional continuum element is used. The material parameters for both isotropic and anisotropic case are same as section 3.1. A single shell element S4R is applied in ABAQUS. Response from the numerical solution shows good agreement with the analytical solution. For the anisotropic case, as the stretch increases the fibers preventing deformation in uniaxial tension. Furthermore, the fiber angle become larger as the stretch of composite increases which decreases further deformation in tension direction, consequently the stress is larger.



**Figure 4.** Stress vs. stretch curve for equibiaxial tension: (a) Isotropic. (b) Anisotropic



**Figure 5.** Equal biaxial tension of viscoelastic materials with isotropic and anisotropic responses

Equal biaxial tension test for viscoelastic response is performed, and the results are portrayed in fig. 5. The material parameters for the anisotropic case are  $\mu = 0.024MPa$  ,  $J_m = 0.9$  ,  $K = 2000$  ,  $K_1 = 0.8MPa$  and  $K_2 = 5.5$  .

Loading/unloading rate in both two directions hold the same value. The stress in two different directions show the same response. From figure 5, the response of anisotropic case from 0-20 seconds is stiffer than isotropic one as we expected and the response from 20-40 seconds remain similar due to viscoelastic response.

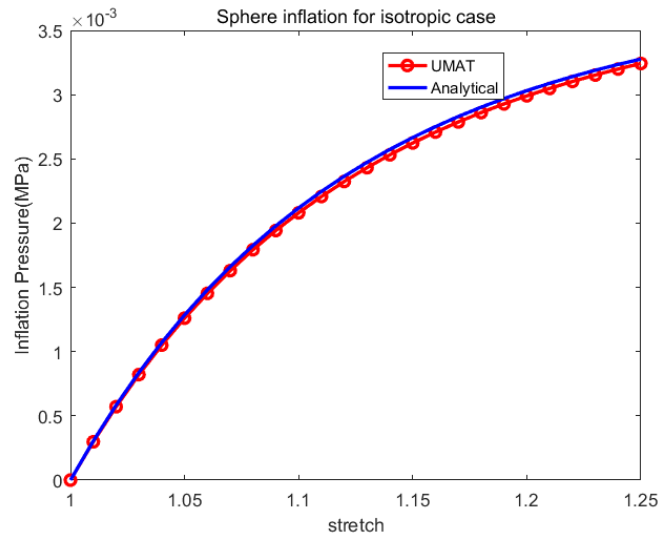
### 3.3 Inflation of a spherical balloon

For an incompressible isotropic model, we consider a pressurized spherical thin shell with undeformed radius smaller than the thickness. We assume the spherical balloon inflate symmetrically in radial directions. The inflation pressure is given by

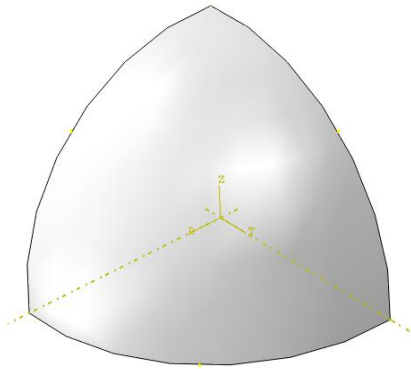
$$P = \frac{2Gt_0}{r_0} \frac{(\lambda^{-1} - \lambda^{-7})J_m}{J_m + 3 - \lambda^{-4} - 2\lambda^2} \quad (3.7)$$

where  $r_0 = 1mm$  is the initial radius of sphere and thickness  $t_0 = 1mm$ . One-eighth model is considered in the simulation using S4R element type in ABAQUS, shown in Figure 7. The material parameters for both isotropic and anisotropic case are same as section 3.1. Figure 6 presents the inflation pressure versus stretch for isotropic Gent material. The material parameters for both isotropic and anisotropic case are same as section 3.1 except that  $J_m$  is altered to 10 to reach larger stretch. It shows the numerical methods are in good agreement with analytical ones.

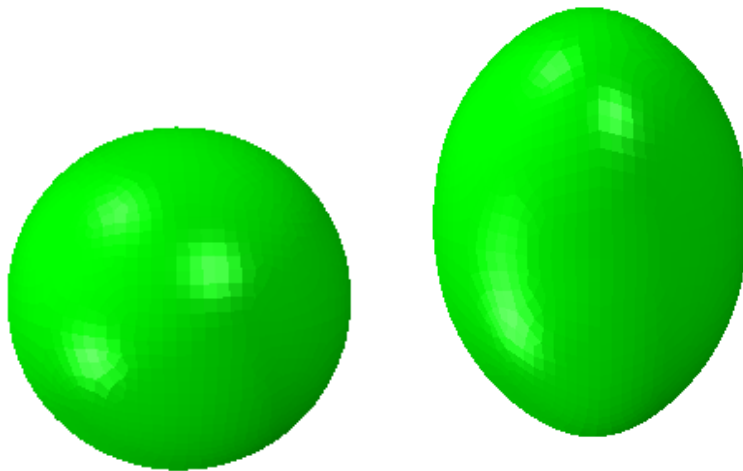
For the anisotropic case, the fiber direction is along the circumferential direction. Figure 8 indicates the elongated spheroid shape with inner pressure load subject to undeformed spherical shape.



**Figure 6.** Inflation pressure vs. stretch for Gent model in balloon inflation



**Figure 7.** The one-eighth of the structure is modeled for simulation



**Figure 8.** Inflation pressure vs. stretch for anisotropic model in balloon inflation: (a) Undeform and (b) deformed model

### **3.4 Circular Pneumatic Actuated Soft Micromold (cPASMO)**

Circular Pneumatic Actuated Soft Micromold (cPASMO) was designed to produce collagen microparticles for encapsulating beta cells. This is a collaborative work with Prof. Jun Kameoka, Department of Electrical Engineering, TAMU. cPASMO is composed of template, pneumatic actuated channel, and resistance. The working principal is to deform the particles' template by generating inner wall pressure of channel. This deformation is able to produce a gap between collagen microparticles and particles' mold and extract collagen microparticles via buoyancy force. Therefore, collagen microparticles can be released gently and the extraction process can be controllable. Moreover, the expanded area can be determined by the position of air channel determines and the uniformity of expansion of particles' mold.

Ecoflex (a siloxane produced by Smooth-On) is widely used in pneumatic soft actuator for a variety of different applications.

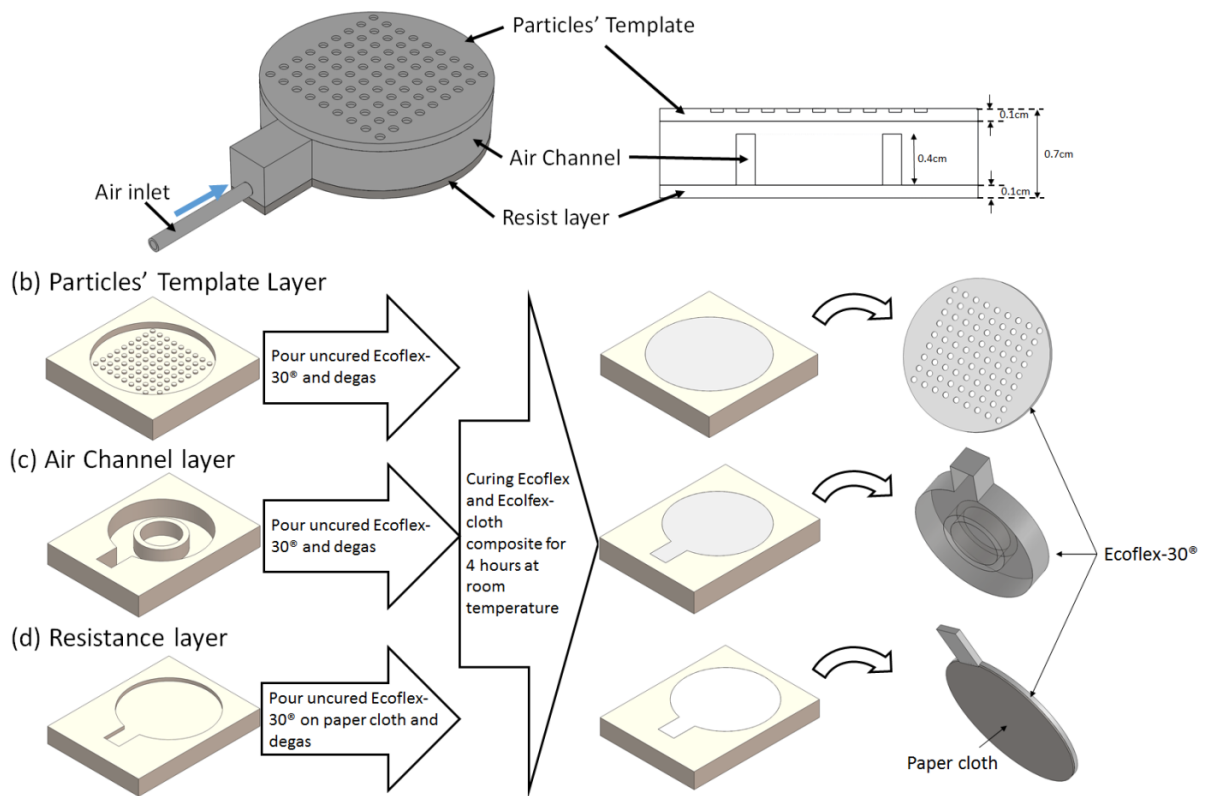
This platform uses soft micro-mold with pneumatic extraction actuator made by ecoflex that can produce arbitrary shapes of collagen microstructures precisely from 100  $\mu\text{m}$  to over 2mm in range and can encapsulate cells inside without causing damage.

#### **3.4.1 Fabrication of cPASMO**

The construction process is shown in figure 9a [61]. Top layer is the particles' template, which is used to generate collagen microparticles and middle layer is air channel for creating the pneumatic actuation. The bottom layer, providing resistance from deformations, transports pneumatic pressure to particles' template for deformation. This actuation can deform particles' template in order to generate gaps for

releasing collagen microparticles. Figure 9b to 9d presents the process to prepare particles' template, air channel and resistance layer, respectively. Particles' template and air channel layer of cPASMO device are fabricated by Ecoflex-30®, while the resistance layer is composed by Ecoflex-30®-cloth composite with stronger mechanical properties. Each layer is made by Envision Tech 3D printer. The uncured Ecoflex-30® is poured in 3D-printed mold for making particles' template, air channel and resistance layer, respectively. Then, the bonding between these three layers is operated by Ecoflex-30® and the curing time is 4 hours at room temperature.

(a) 3D view and side view of cPASMO



**Figure 9.** Schematic diagram of circular pneumatic actuated soft micromolds (cPASMO) device (a) 3D and top view of circular PASMO device, which is composed by three layers, template layer, channel part and resist layer. Molds is printed through 3D printer. (b-d) The master mold of particles' template, air channel and resistance are made by 3D printer, respectively. Uncured Ecoflex-30® is poured into each mold. After being cured for 4 hours at room temperature, peel them from mold. Layers are bonded for 4 hours at room temperature with uncured Ecoflex-30® used as glue between them.

### 3.4.2 Modeling of cPASMO

The device consists of a cylindrical body with three different layers. A schematic of a PASMO device is shown in Fig. 9. The bottom layer is rather thin (1 mm) and is made of a relatively stiff material in order to prevent expansion at the bottom surface when air pressure is applied. The second layer consists of a circular micro-channel of Ecoflex material where air pressure is applied. The thickness of the second layer is 7 mm and the height of the micro-channel is 4 mm. The top layer of 1 mm thickness is made of Ecoflex material with several wells printed on its top surface. The wells have a diameter of 1mm and depth of 0.3mm.

The finite element (FE) software ABAQUS 6.12 was used to simulate the expansion of pneumatic actuation of the micromold. The deformation determined from the FE analysis is compared with the experimentally measured deformation of the PASMO devices. The displacement of the bottom surface of the PASMO model is a constraint to avoid rigid body motion. Pneumatic pressures are set as the pressure load applied in the pneumatic channel of PASMO device. Since the model is symmetric, only a quarter model of PASMO is generated using 308,292 tetrahedral elements and each element consists of 10-node modified hybrid tetrahedral elements (ABAQUS C3D10MH). Modified tetrahedral elements provide good convergence rate and prevent volumetric locking. Locking is caused by imposing the incompressible constraint on the solution compared to degrees of freedom. For nearly incompressible materials, the Poisson's ratio approaches 0.5 and the bulk modulus become infinitely large.



Abaqus/standard uses hybrid formulation with a Lagrange multiplier interpolated. With a variable  $\hat{J}$  introduced and  $J - \hat{J} = 0$ , the internal energy integral is

$$W_I = \int_V [U(\bar{I}_1, \hat{J}) - p(J - \hat{J})] dV . \quad (3.8)$$

Hyperelastic material models are capable of describing the nonlinear elastic response of soft materials. Three different material models for isotropic response are considered, e.g., Gent, Yeoh, and Ogden. The Gent model has been implemented in UMAT, while Yeoh and Ogden models are available in ABAQUS library.

The strain energy density function for an incompressible Ogden model (N=3) is described as

$$U = \sum_{i=1}^N \frac{2\mu_i}{\alpha_i^2} \left( \bar{\lambda}_1^{\alpha_i} + \bar{\lambda}_2^{\alpha_i} + \bar{\lambda}_3^{\alpha_i} - 3 \right) + \sum_{i=1}^N \frac{1}{D_i} (J^{el} - 1)^{2i} \quad (3.9)$$

where U is the strain energy per unit of reference volume;  $\alpha_i$ ,  $\mu_i$  are material constants;  $\bar{\lambda}_i$  are the deviatoric principal stretches  $\bar{\lambda}_i = J^{-\frac{1}{3}} \lambda_i$ ;  $\lambda_i$  are the principal stretches; and J is the determinant of deformation gradient. The following material

parameters are used for the Ogden model:  $N = 3$  ,  $\mu_1 = 0.0111MPa$  ,  $\mu_2 = 1.119E - 05MPa$  ,  $\mu_3 = 0.0114MPa$  ,  $\alpha_1 = 2.393$  ,  $\alpha_2 = 8.123$  and  $\alpha_3 = -2.168$  .

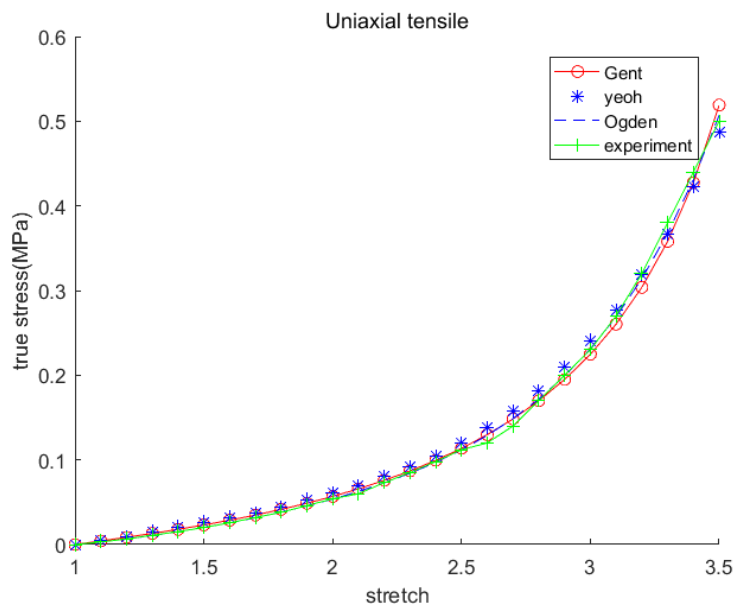
The material parameters for incompressible Yeoh model are  $C_1 = 0.008MPa$  ,  $C_2 = 4e - 5MPa$  and  $C_3 = 4e - 5MPa$  . The compressible Gent model parameters are

$\mu = 0.014MPa$  ,  $J_m = 14.5$  ,  $K = 2000$  . A comparison (Figure 11) has been for Ogden

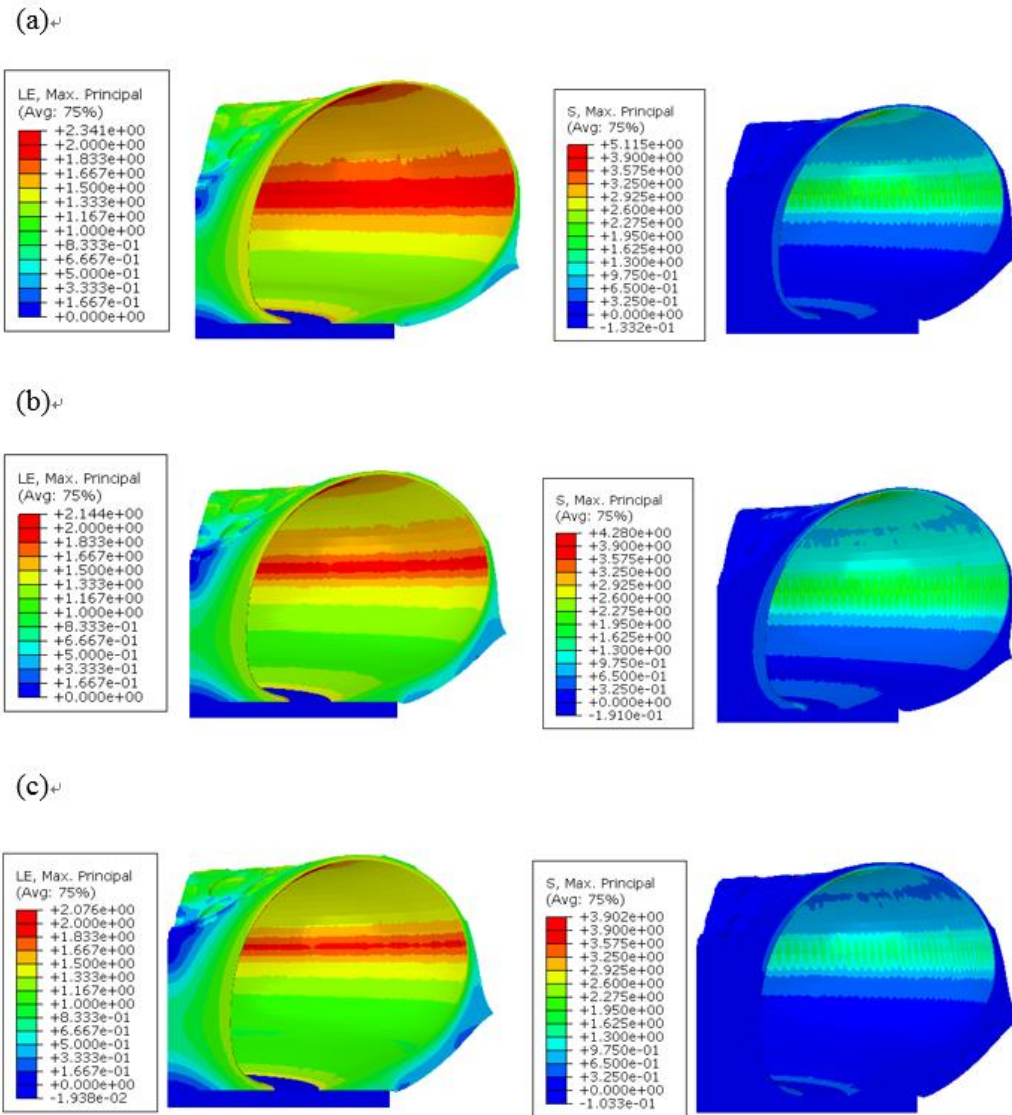
model, Yeoh model and Gent model with the max principal strain equal to two and minimum principal strain zero. The maximum principal stress is equal to 3.9 MPa and

minimum principal stress is set up as zero. It is seen that slight variations are seen in the stress and strain field in case of multi-axial responses are considered. The material

parameters in the above models are obtained from testing uniaxial tensile specimens (Figure 10).



**Figure 10.** The fitting material parameter for Ogden(a), Yeoh(b) and Gent(c) model.



**Figure 11.** The deformed max principal stress contour plots of cPASMO for Ogden(a), Yeoh(b) and Gent(c) model.

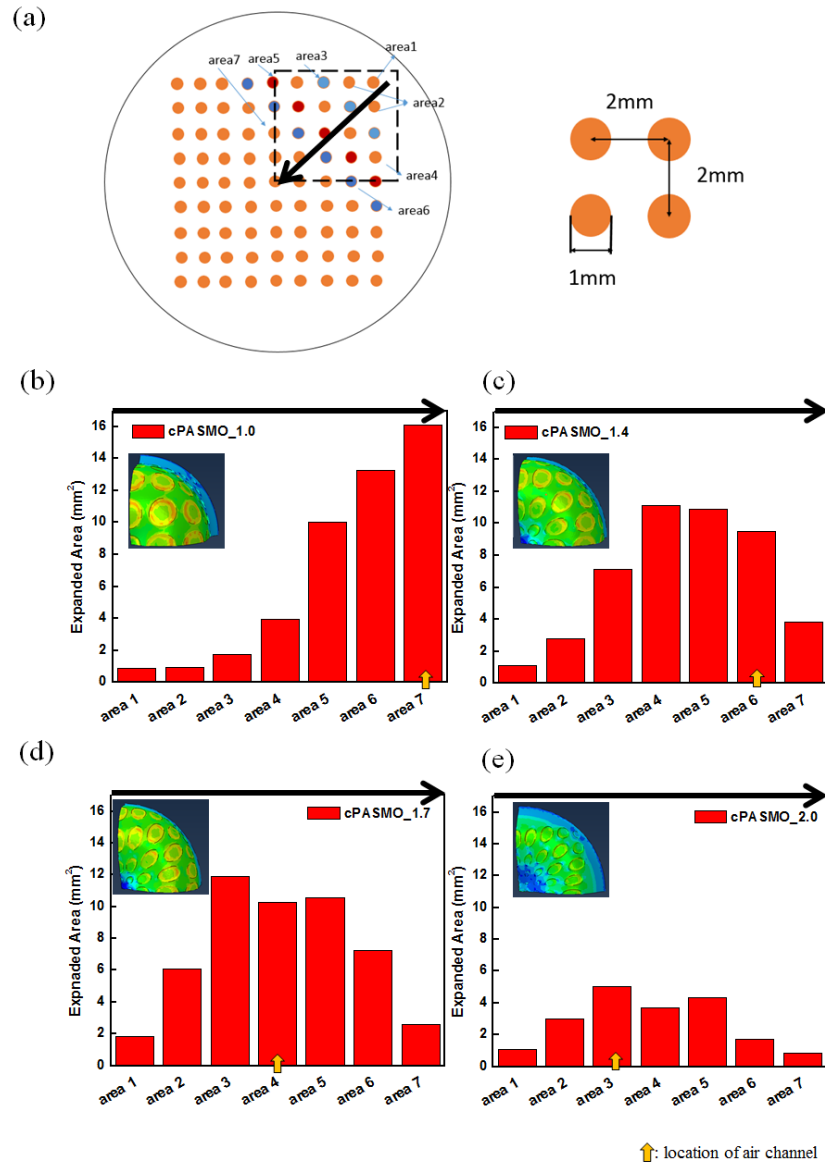
### 3.4.3 Results

To determine the expanded area and the uniformity of expansion of particles' wells, simulation is performed to optimize the design of the position of air channel. Figure 12 presents the deformed expanded area after pneumatic deformation. According to the different expanded level of deformation at different area, particles' wells are classified as seven areas, which indicate area 1 to area 7 from outer to inner region shown in Figure 12a. Figure 12b to 12e presents the distribution of expanded area from area 1 to

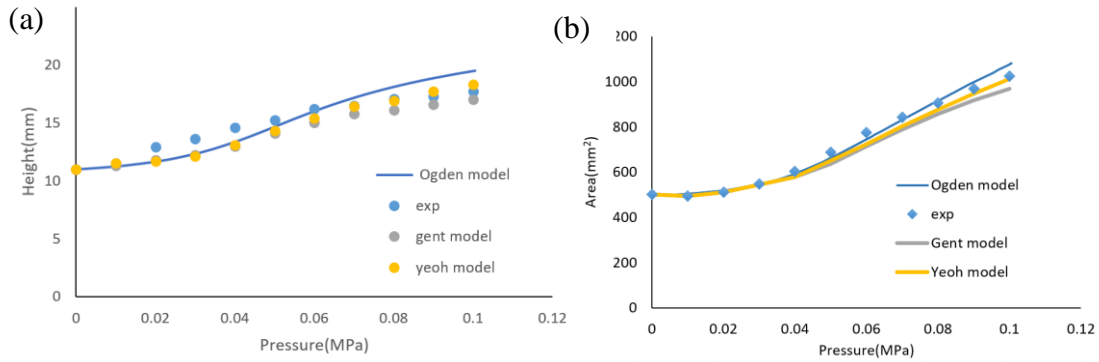
area 7 in cPASMO\_1.0 to cPASMO\_2.0. The maximum expanded area is located at channel's position because larger deformation is generated from center of air channel. The further location from air channel decreases the deformed level of particles' well because the pneumatic force cannot propagate through whole cPASMO device. Figure 12c mentions the distribution of expanded area of each particles' well on cPASMO\_1.4. However, the maximum deformed particles' wells are not located at the air channel position because of two-dimensional deformation of cPASMO device. Once the lateral resistance decreases as following the decreasing lateral thickness, like cPASMO\_1.4, the pneumatic force would contribute lateral and vertical deformation simultaneously. This two-dimensional deformation would help improving the expansion at wider region. Figure 12d shows the distribution of deformed particles' wells for cPASMO\_1.7. The deformation of particles' well and expanded area of each region on cPASMO\_1.7 is similar as cPASMO\_1.4 so that cPASMO\_1.7 can also contribute two-dimensional deformation. However, if the position of air channel moves further to 2.0cm called cPASMO\_2.0, the pneumatic force generated from air channel for cPASMO\_2.0 cannot propagate and contribute to centric region (area 6 and area 7) so that the expanded area of particles' wells cannot properly produce gap between collagen microparticles and mold.

cPAMSO-1.4 is selected as the optimized dimension to create larger gap and generate larger mold expansion which can enhance the releasing rate of collagen micro-disks without damage. Figure 13 shows the responses determined from the FE analyses are in good agreements with the experimental results for cPAMSO-1.4. Responses from

different models were considered. This analysis shows that the UMAT code is capable in capturing nonlinear elastic response of isotropic materials undergoing large deformation.



**Figure 12.** Expanded area of cPASMO device from seven areas. (a) Schematic diagram of micro-disks' mold of cPASMO device and we distinguished as seven areas, area 1 to area 7 from outer to inner, respectively. (b) cPASMO\_1.0 presents the expanded area varied from area 1 to area 7. The position of air channel is located at area 7. (c) cPASMO\_1.4 presents the expanded area varied from area 1 to area 7. The position of air channel is located at area 6. (d) cPASMO\_1.7 presents the expanded area varied from area 1 to area 7. The position of air channel is located at area 4. (e) cPASMO\_2.0 presents the expanded area varied from area 1 to area 7. The position of air channel is located at area 3.



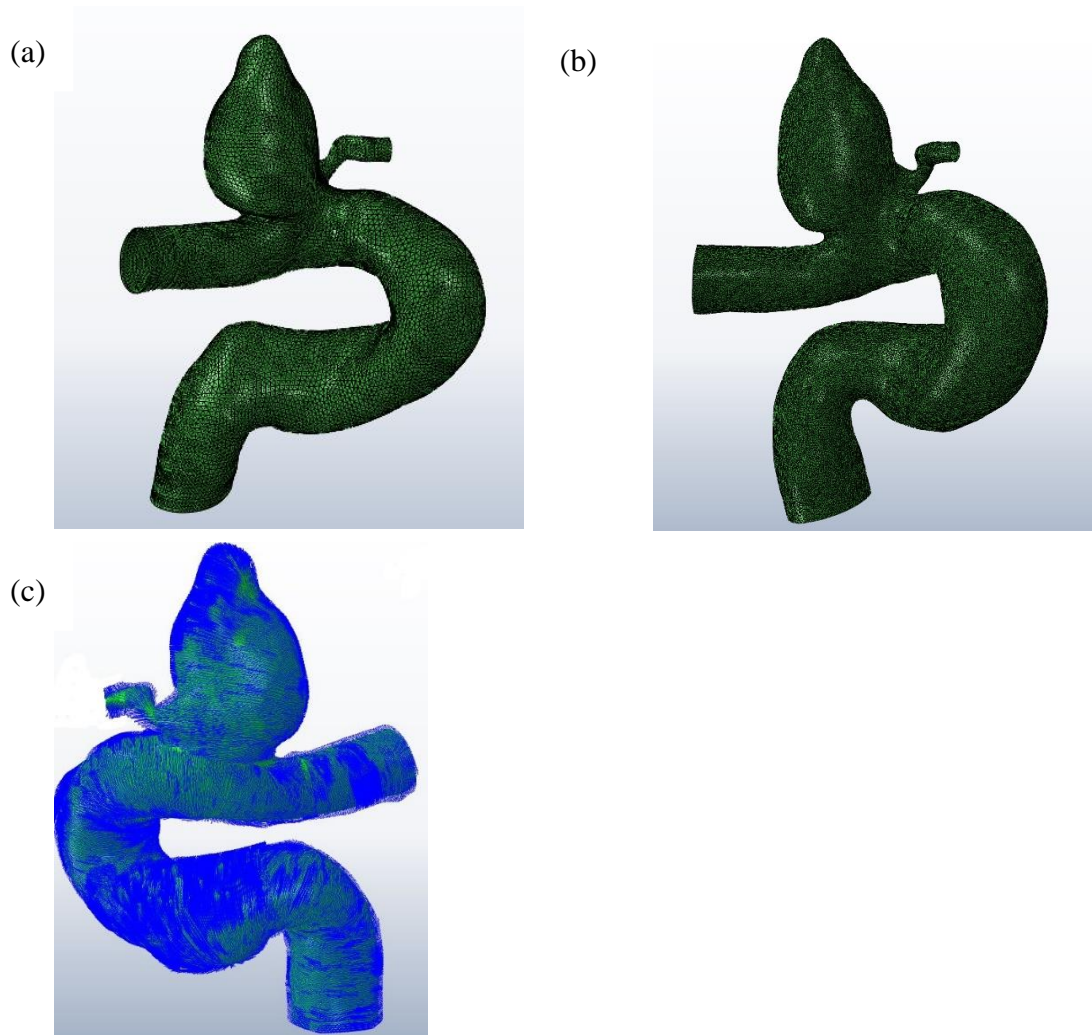
**Figure 13.** The plot of simulation result of pressure versus expanded area of particles' wells (a) and the max height of cPASMO (b) mold area of cPASMO.

### 3.5 Modeling of mechanical response of blood vessels

Stents have been considered to provide mechanical support for damaged blood vessels. In the design of stent and/or patient treatment, it is important to understand the interaction between stent and blood vessels, when the system is subjected to mechanical boundary condition, e.g., pressure from the fluid/blood flow. Prior to studying the interaction between stent and blood vessel, it is necessary to have proper material models for both stent and vessels. In this study, we will consider metallic stent with elastic-plastic material model. As for the vessels, we will first assume the vessels as nonlinear elastic with anisotropic material model. Later we will extend this to include time-dependent response. We start with modeling blood vessels considering patient specific geometry. The image was obtained from Methodist Hospital Houston (Dr. Christof Karmonik). We will continue with deploying metallic stent inside the vessels.

### **3.5.1 Numerical analysis of deformation of blood vessel from brain aneurysm model**

Inflation test was carried out with nearly incompressible transversely isotropic material model. We model the artery wall as a homogeneous material with one family of fibres. It was meshed with three-noded shell elements S3R in Abaqus. Before performing simulation on the realistic geometry model from CT, finite element processor HyperMesh is used to reconstruct the mesh in order to avoid stress concentration at the corner (figure 14b) In Abaqus, the local material 1- and 2- axis lie in the plane of shell and 2- direction is perpendicular to the 1-direction. The local 1-direction is the projection of the global x-axis onto the shell surface. After local 1-axis is determined, fiber direction could be defined. Abaqus allow us to indicate material orientation for local element, and since there are more than 80k elements for the model, it is more efficient to define orientation for slices by dividing model into several segments. Spatially varying local coordinate systems for shell elements was defined by distributions in Abaqus (figure 14c).

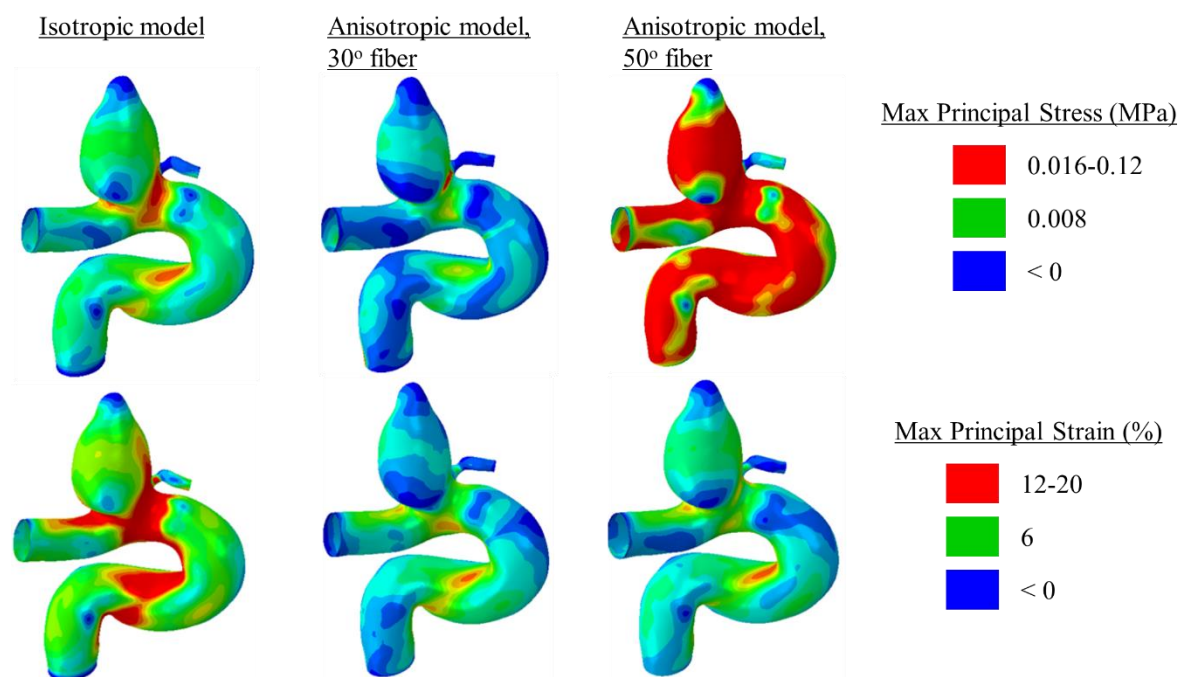


**Figure 14.** (a) CAE model of a Patient brain aortic vessel and (b)reconstructing the geometry of the model by smoothing the curve. (c) Local 1-axis of the realistic geometry model.

The material parameters for the vessels are calibrated from experimental data[62]. The parameters are  $\mu = 0.0024MPa$  ,  $J_m = 0.9$  ,  $K = 2000$  ,  $K_1 = 0.001$  and  $K_2 = 1.2$  . In case of isotropic response, the parameters related to the anisotropic part are set to zero. Figure 15 below shows principal stress and strain of a blood vessel of patient with brain aneurysm, subjected to inner pressure of 0.025 MPa. We compare the response when isotropic and anisotropic material responses are considered. It is noted that we also study the effect of fiber orientation since it is not that obvious or easy to determine fiber



direction. As expected the blood vessel response depends strongly on the anisotropic material model. It is also noted that it is necessary to determine proper material parameters for specific tissue under investigation; however, these data are not always available. Thus, we will later study the effect of different material parameters obtained from different tissue.



**Figure 15.** Simulation results for isotropic and anisotropic with different fiber angle

### 3.6 Microhands model

We proposed a micro-hand model with biocompatibility of PDMS using the pneumatic soft actuator. Three fingers on the pneumatic channel open and close as a result of a swelling of the pneumatic channel that can be an ideal replacement for micro-grippers. The structure allows one to capture soft and fragile samples by closing fingers. When inflating the channel like balloons for actuating the fingers open which enable

them to grab larger samples. The maximum force can be measured by AFM and output in Abaqus, while the measurement of angles of fingers was performed by optical microscope. Comparison of the angles of fingers versus the volume change of pneumatic channel was made between experiment and simulation results.

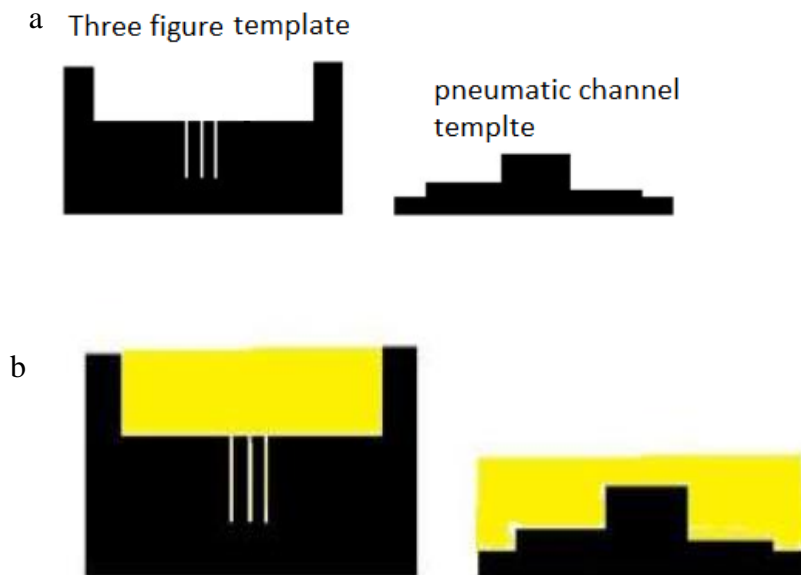
### **3.6.1 Experiment work**

We used polydimethylsiloxane (PDMS) because it is biocompatible, nontoxic and has been used for ear and nose implants as a biomaterial. PDMS is widespread used in the development of MEMS for biomedical applications. Both of them are easy to mold and inexpensive. PDMS is transparent and capable of resisting repeated bending which is suitable for our micro hand model that only bending is required. PDMS has a Shore A hardness of 50 while ecoflex has a hardness below the Shore A scale test so that it is too soft to bend under its own weight. When interacting with cells, the three fingers of PDMS have a limited range of deflection which enable to produce gentle biomechanics. The highly challenging issue of the manufacturing process is that PDMS is sticky. To prevent the PDMS model from adhering to the 3D printed molds, silane gas was used to cover the mold. The size of micro hand model is significantly small, which make it greatly difficult to ensure precision of dimensions.

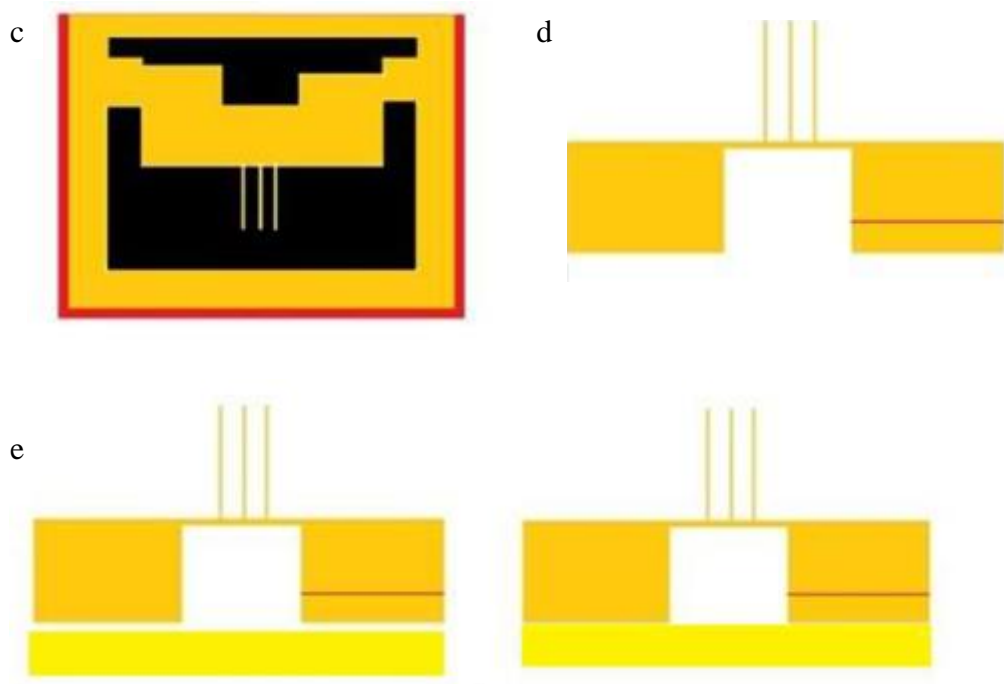
The micro hand model is manufactured from polydimethylsiloxane (PDMS) network 10:1 by 3D printed mold. PDMS was made by PDMS silicone elastomer base and PDMS silicone elastomer curing agent and purchased from Dow Corning. The base and agent were mixed at a ratio of 10:1 by weight. To debubble the mixture, the PDMS

mixture was degassed under vacuum for 20~30 minutes. The PDMS network was cured for one week at room temperature. The molds of the model were fabricated by Envisiontech perfactory microprinter 3D printer and light cured for 72 hours at 65°C in oven.

Figure 16 describes the approach we applied to manufacture microhands. The two parts of the mold are used to shape three fingers and pneumatic channel template separately (Figure 16a). After covering both parts of the mold by PDMS, we placed the model in a vacuum environment to remove all bubbles. After all bubbles were eliminated, we closed the two parts and placed them into one PDMS container under vacuum for debubbling. After the model was cured for one week at the room temperature, we removed the mold gently.



**Figure 16.** Fabrication of Micro-hand. (a) The first part of mold with three figures template and the second part of mold with pneumatic channel template. (b) The mold is filled with PDMS and cured in vaccum. (c)The mold is placed into a container filled with PDMS and remained in the room temperature for one week to remove bubbles from PDMS. (d) The micro hand model is removed from the mold. e) Bond micro hand model to a plate of PDMS with oxygen plasma treatment and water.



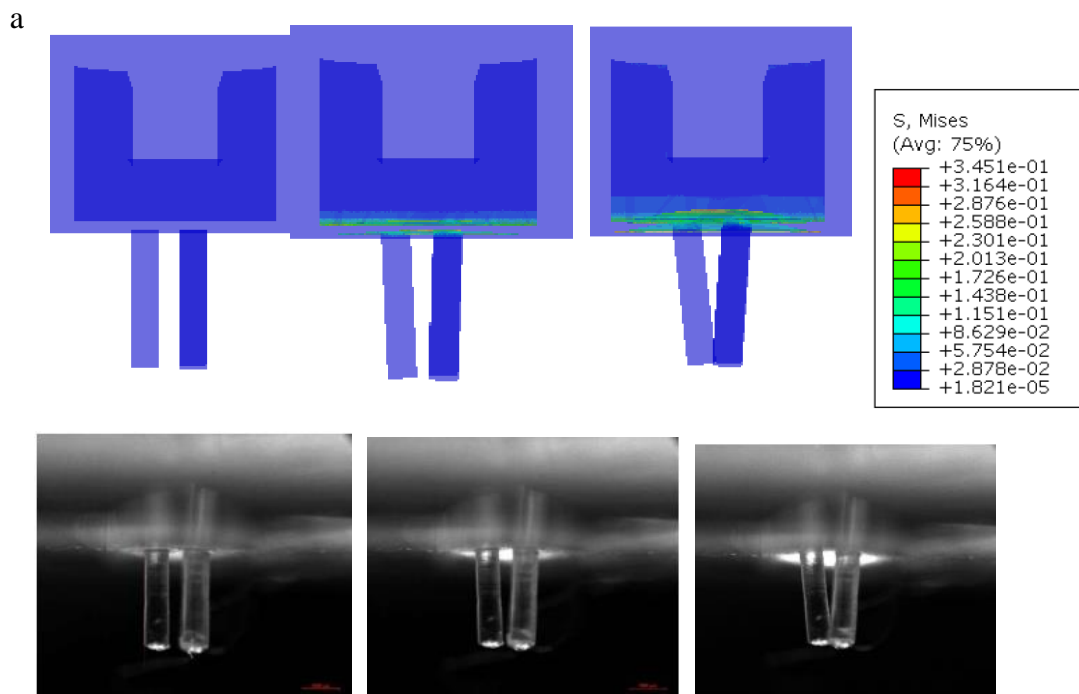
**Figure 16** Continued.

### 3.6.2 Modeling and simulation

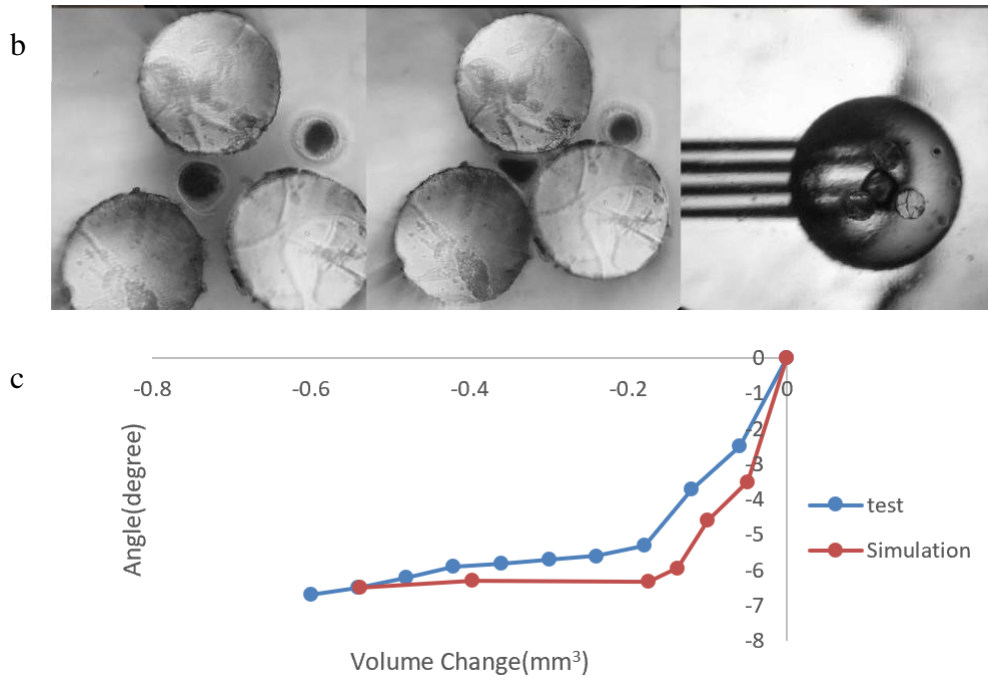
The finite-element software ABAQUS 6.12 was carried out to build up a 3D model for simulating the pneumatic actuation of the micro hand. The deformation result is shown in Figure 18. The displacement of the bottom surface of the model was constraint since the model was bonded horizontally on a plate of PDMS. Applied pneumatic pressures are set as pressure load which acts in the nominal direction on pneumatic channel. General surface-to-surface contacts are set up for three figures. The model uses 376,938 tetrahedral elements and consists of 10-node modified hybrid tetrahedral elements (ABAQUS C3D10MH). Modified tetrahedral elements provide good convergence rate and prevent volumetric locking. Hyper elastic material models are highly capable of describing the nonlinear response of complex materials. The

Supporting Information shows the experimental relationship between stress and strain for the PDMS under uniaxial tension. With the experiment data fitted and analyzed, the PDMS was modeled as an incompressible and isotropic Gent model which are satisfied with convergence and solution satiability. The Gent model with isotropic condition is applied and material properties are  $\mu = 0.4MPa$  and  $J_m = 5.5$ .

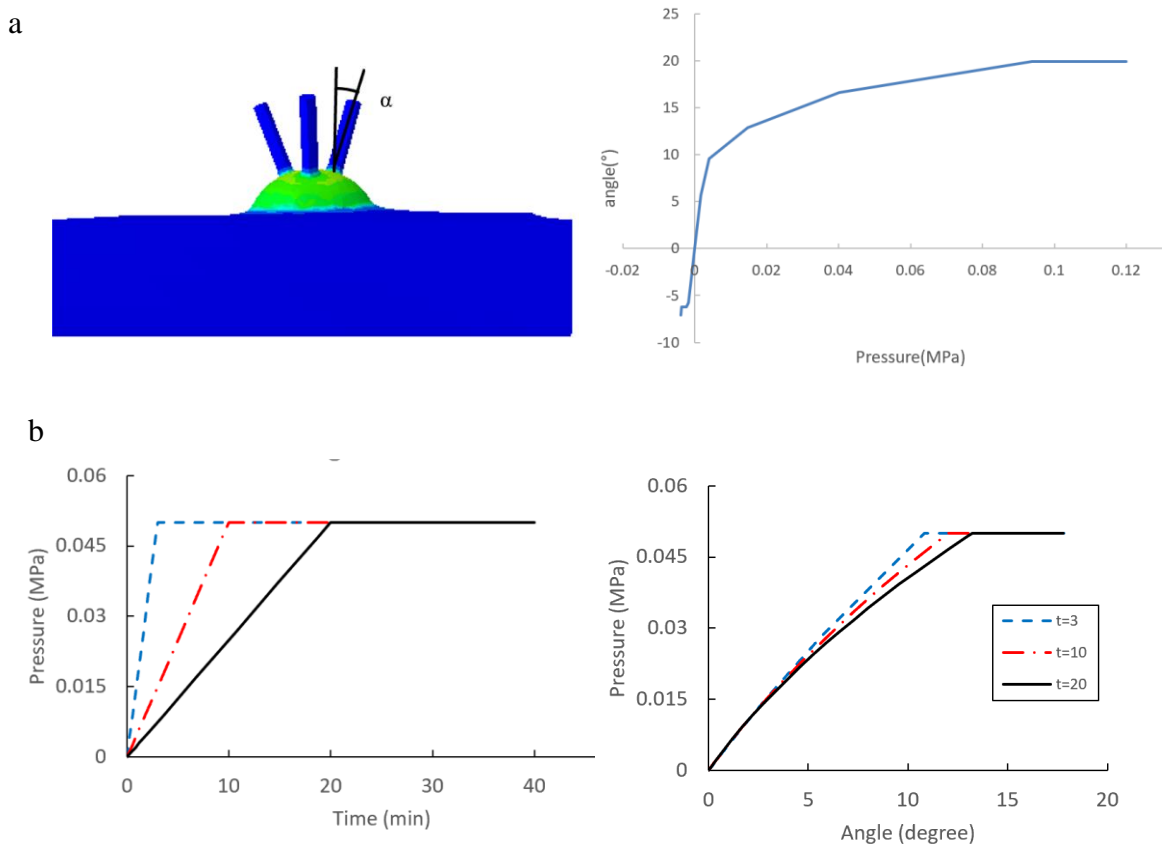
Microliter syringe and optical microscope were used to test the characterization of the micro hand model. The model was placed under optical microscope horizontally to capture the deflection. The three fingers opening and closing are actuated under pressure supply by syringe. The comparison figures of simulation and experiment results for three hands closing (figure 17a). The figure 17b shows that the model enables to provide enough force to hold and deform embryonic cell.



**Figure 17.** (a) Three fingers closing for simulation and experiment results, (b) the optical Image of fingers holding bio samples, (c) the volume change of channel vs angle of microhands for experimental and simulation results.



**Figure 17 Continued.**



**Figure 18.** (a) The introduction of angle  $\alpha$  and pressure vs angle (b) time versus pressure and pressure versus angle.

We applied viscoelasticity model for the soft material. The angle  $\alpha$  presented in Fig. 18(a) is defined as the angle between vertical axis and the line of center of micro hand. The material parameters is calibrated from the experimental data in Jennifer et al. [63] are the characteristic relaxation time  $\tau = 3$  min and the initial value of  $\frac{\mu_{\infty}}{\mu} = 0.7$  defined in equation 2.36. To observe significant viscoelastic response, we hypothesis the relaxation time is 10 min. Figure 18 (b) indicate different results of angle  $\alpha$  with respect to different loading rates with loading ramp 3 min, 10 min, and 20 min and the faster pressure loading, the smaller angle degree under same pressure. This result highlights the importance of incorporating time-dependent material behaviors for precise positioning of the devices, which can be crucial for many biomedicine applications.

## CHAPTER IV

### MECHANICAL RESPONSES OF SOFT COMPOSITES

In this chapter, soft composite responses under different boundary conditions are examined. The first case study considers uniaxial tension and compression of soft composite plates. The soft composites comprise of glass fibers embedded in soft matrix. Two soft matrixes, i.e., silicone rubber ecoflex and PDMS, with different mechanical responses are studied, Responses for different parameters, i.e., fiber volume fraction, fiber shape and fiber angle, are investigated in order to understand the behavior of the soft composites. The second case studies the influence of viscoelastic matrix on the overall responses of the soft composites. The third case presents simulations of soft composite structures and devices under different loading conditions.

The material properties of PDMS are calibrated from experimental data in literature [63]. The properties of ecoflex 00-30 were obtained from experimental data [64]. The Gent model with isotropic condition is applied for the soft matrix and the material properties of ecoflex 00-30 and PDMS are  $\mu = 0.017MP$  and  $J_m = 14$ ;  $\mu = 0.65MPa$  and  $J_m = 5.0$  separately. Linear elastic material model is used for the glass fiber inclusions and the material properties are: Young's modulus 10 MPa and Poisson's Ratio 0.3.



#### 4.1 Uniaxial Responses of Elastic Soft Composites

Uniaxial tension and compression behaviors of soft composite plates with elastic and viscoelastic matrix are examined in this section. The geometry of soft composite plates is 10x10x0.5 mm. Two different fiber cross-sections are considered in order to understand the influence of fiber geometries on the overall responses of soft composites. For the circular fiber, the radius is 0.2 mm and for the square fiber the dimension is 0.07x0.07 mm for the rectangular fiber. The thickness dimension is much smaller than the length and width; The material can be treated as a state of plane stress; The material is made up of one layer consisting of fibers uniformly parallel and continuous across the material. We assume the soft composite as a single ply laminated composite materials, the laminated composite shows the coupling behavior, unique to this type of material. The composites share the common feature that couplings between in-plane (i.e., extension or shear) and out-of-plane (i.e., bending or flexure) responses.

In a linear elastic laminate composite made up of a single layer, the coupling relationship is given as:

$$\begin{cases} N_x \\ N_y \\ N_s \end{cases} = \begin{bmatrix} A_{xx} & A_{xy} & A_{xs} \\ A_{xy} & A_{yy} & A_{ys} \\ A_{xs} & A_{ys} & A_{ss} \end{bmatrix} \begin{cases} \varepsilon_x \\ \varepsilon_y \\ \gamma_s \end{cases} + \begin{bmatrix} B_{xx} & B_{xy} & B_{xs} \\ B_{xy} & B_{yy} & B_{ys} \\ B_{xs} & B_{ys} & B_{ss} \end{bmatrix} \begin{cases} \kappa_x \\ \kappa_y \\ \kappa_s \end{cases} \quad (4.1)$$

$$\begin{cases} M_x \\ M_y \\ M_s \end{cases} = \begin{bmatrix} B_{xx} & B_{xy} & B_{xs} \\ B_{xy} & B_{yy} & B_{ys} \\ B_{xs} & B_{ys} & B_{ss} \end{bmatrix} \begin{cases} \varepsilon_x \\ \varepsilon_y \\ \gamma_s \end{cases} + \begin{bmatrix} D_{xx} & D_{xy} & D_{xs} \\ D_{xy} & D_{yy} & D_{ys} \\ D_{xs} & D_{ys} & D_{ss} \end{bmatrix} \begin{cases} \kappa_x \\ \kappa_y \\ \kappa_s \end{cases}$$

where [A] is the extensional stiffness matrix, [B] is the coupling stiffness matrix and [D] is the bending stiffness matrix  $\boldsymbol{\varepsilon}$  is the vector of in-plane strains ( $=\{\varepsilon_x, \varepsilon_y, \varepsilon_z\}^T$ ), and  $\boldsymbol{\kappa}$  is the vector of curvature ( $=\{\kappa_x, \kappa_y, \kappa_z\}^T$ ).

Case 1 presents a comparison between different fiber angles, measured from the lateral direction of the plate, for soft composites of circular fiber shape under a uniaxial tension. The composite plate models are shown in Fig. 20. The composites have around 0.231 fiber volume fraction. Figure 19 shows the uniaxial tensile behaviors, in terms of engineering stress and stretch for soft composites with different fiber angles and two soft matrices. The uniaxial responses of the two matrices are also shown in the figure 19. The PDMS is about ten times stiffer than the ecoflex matrix. For ecoflex soft matrix, fiber angles highly affect on overall mechanical behavior of soft composite, especially for 60° fiber angle much stiffer than 45- and 30-degree cases. It is can be explained as the soft ecoflex leads to fiber reorientation towards the loading axis and can be aligned with the loading axis, hence resulting in stiffening in the overall responses. For the composites with PDMS matrix, the effect of fiber angles on overall mechanical behavior of soft composite is quite insignificant. The fiber did make the soft composite stiffer compared to PDMS pure matrix. It is can be explained as the PDMS is 10 times stiffer than ecoflex which results in more resistant to fiber rotation.

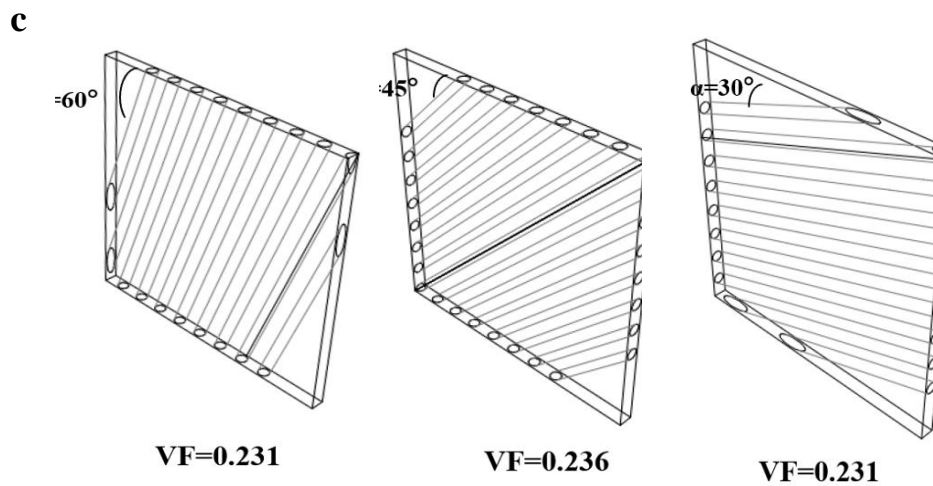
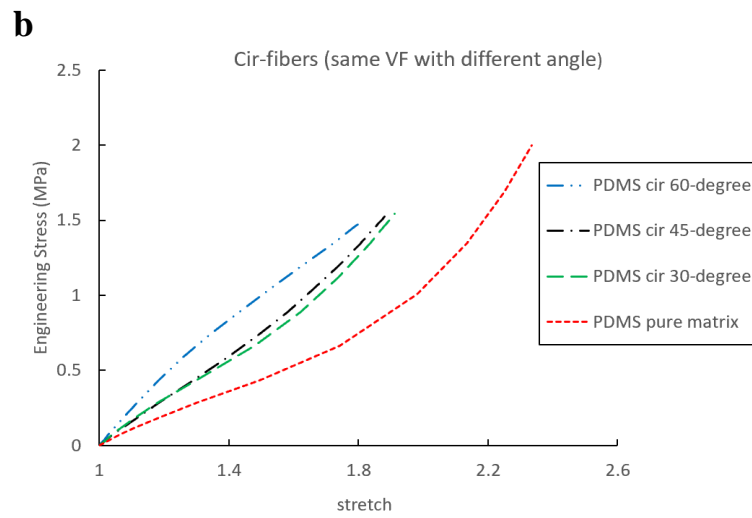
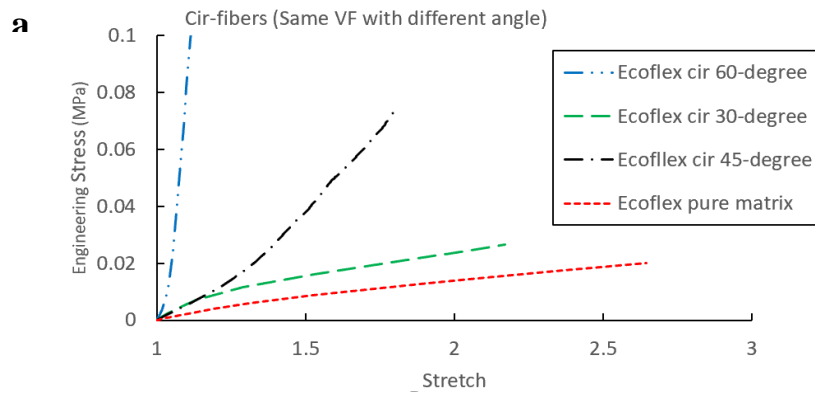
Comparing the results of EcoFlex and PDMS in Fig. 19 the stretch of PDMS are around 1.9 while that of EcoFlex composites vary largely based on different fiber angles. The engineering stress of PDMS composite is around 1.5 MPa compared with 0.25 MPa the largest stress EcoFlex can reach. For the EcoFlex, it is interesting to note, the fiber angle in 60 degree is much stiffer than 45 degree and 30 degree. The stiffer fact can be explained that the hard inclusion predominately preventing deformation in the uniaxial tension and the fiber angle become larger as the stretch of composite increases which

decreases further deformation in tension direction, consequently the engineering stress is larger and stretch is smaller compared with other two fiber angles.

Table 1 summarizes changes in fiber angles for soft composites with PDMS and EcoFlex matrix for different initial fiber angles. For both soft materials, the fiber angles change significantly and the fiber changes for the PDMS composites are around 20 degree and the changes for the Ecoflex composites are around 30 degree. The explanation is that ecoflex is very soft and allows for easy fiber reorientations.

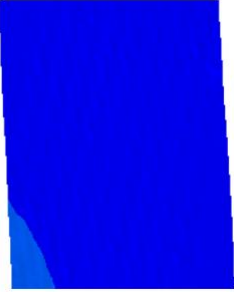
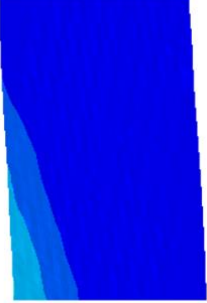

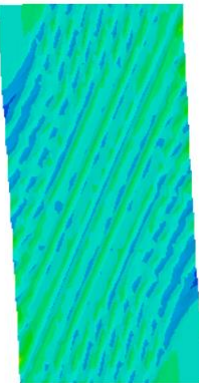


**Table 1** Fiber angles changes ( $\Delta \alpha$ ) with PDMS and EcoFlex matrix for different initial fiber angles

matrix Initial angle	PDMS	Ecoflex
30°	15.54°	30.6°
45°	25.93°	30.47°
60°	21.55°	26.73°

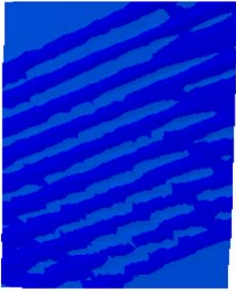
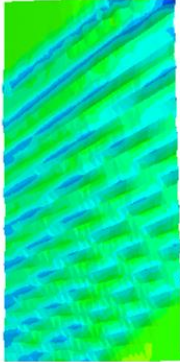
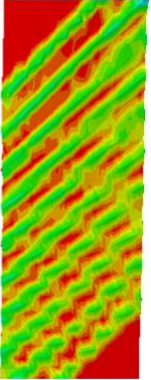


**Figure 19.** (a) Soft composite model with circular fiber shape of different fiber angles for ecoflex (b) for PDMS (c) Schemes for composite with circular fiber cross-section of different fiber angles

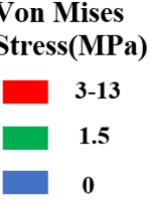



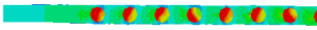
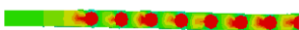
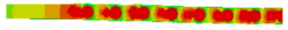


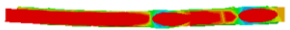
**Table 2** Contour plots of front view for PDMS matrix composite with circular fiber cross-section of different fiber angles

Soft composite with circular fiber cross-section in front view	Contour plots for early stage deformation	Contour plots for middle stage deformation	Contour plots for final deformation  <b>Von Mises Stress(MPa)</b> <div style="display: flex; flex-direction: column; align-items: center;"> <div style="display: flex; align-items: center; margin-bottom: 5px;"><span style="width: 15px; height: 10px; background-color: red; margin-right: 5px;"></span> 3-13</div> <div style="display: flex; align-items: center; margin-bottom: 5px;"><span style="width: 15px; height: 10px; background-color: green; margin-right: 5px;"></span> 1.5</div> <div style="display: flex; align-items: center;"><span style="width: 15px; height: 10px; background-color: blue; margin-right: 5px;"></span> 0</div> </div>
Fiber angle 60° case	 Axial stretch is 1.15	 Axial stretch is 1.53	 Axial stretch is 1.8
Fiber angle 45° case	 Axial stretch is 1.24	 Axial stretch is 1.64	 Axial stretch is 1.82

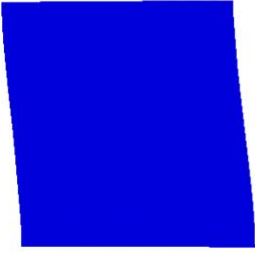
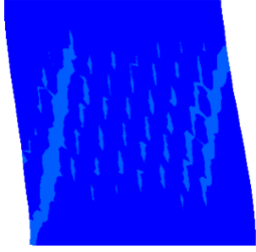
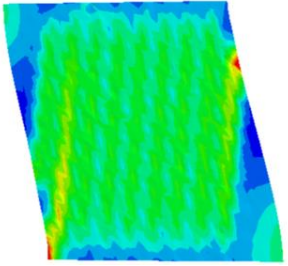
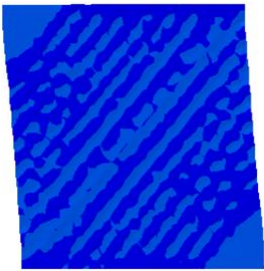
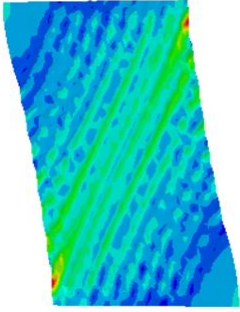
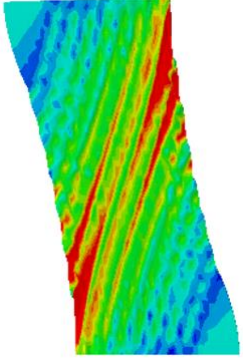
**Table 2** Continued.

<p>Soft composite with circular fiber cross-section in front view</p>	<p>Contour plots for early stage deformation</p>	<p>Contour plots for middle stage deformation</p>	<p>Contour plots for final deformation</p> <p><b>Von Mises Stress(MPa)</b></p> <p><span style="color: red;">■</span> 3-13</p> <p><span style="color: green;">■</span> 1.5</p> <p><span style="color: blue;">■</span> 0</p>
<p>Fiber angle 30° case</p>	 <p>Axial stretch is 1.2</p>	 <p>Axial stretch is 1.66</p>	 <p>Axial stretch is 1.83</p>

**Table 3** Contour plots of top view for PDMS matrix composite with circular fiber cross-section of different fiber angles

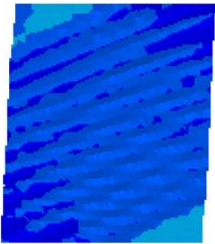
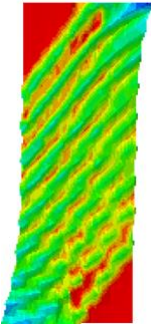

Soft composite with circular fiber cross-section in top view	Contour plots for early stage deformation	Contour plots for middle stage deformation	Contour plots for final deformation  <b>Von Mises Stress(MPa)</b> 
Fiber angle 60° case	 Axial stretch is 1.15	 Axial stretch is 1.53	 Axial stretch is 1.8
Fiber angle 45° case	 Axial stretch is 1.24	 Axial stretch is 1.64	 Axial stretch is 1.82
Fiber angle 30° case	 Axial stretch is 1.2	 Axial stretch is 1.66	 Axial stretch is 1.83

**Table 4** Contour plots in front view for ecoflex matrix composite with circular fiber cross-section of different fiber angles

Soft composite with circular fiber cross-section in front view	Contour plots for early stage deformation	Contour plots for middle stage deformation	Contour plots for final deformation  Von Mises Stress (MPa) <span style="color: red;">■</span> 0.05-4 <span style="color: green;">■</span> 0.025 <span style="color: blue;">■</span> 0
Fiber angle 60° case	 Axial stretch is 1.05	 Axial stretch is 1.1	 Axial stretch is 1.19
Fiber angle 45° case	 Axial stretch is 1.21	 Axial stretch is 1.54	 Axial stretch is 1.81



**Table 4** Continued

Soft composite with circular fiber cross-section in front view	Contour plots for early stage deformation	Contour plots for middle stage deformation	Contour plots for final deformation  Von Mises Stress (MPa) <div style="display: flex; flex-direction: column; align-items: center;"> <div style="display: flex; align-items: center; margin-bottom: 2px;"><span style="width: 15px; height: 10px; background-color: red; margin-right: 5px;"></span> 0.05-4</div> <div style="display: flex; align-items: center; margin-bottom: 2px;"><span style="width: 15px; height: 10px; background-color: green; margin-right: 5px;"></span> 0.025</div> <div style="display: flex; align-items: center;"><span style="width: 15px; height: 10px; background-color: blue; margin-right: 5px;"></span> 0</div> </div>
Fiber angle 30° case	 <p style="text-align: center;">Axial stretch is 1.52</p>	 <p style="text-align: center;">Axial stretch is 1.92</p>	 <p style="text-align: center;">Axial stretch is 2.16</p>

**Table 5** Contour plots in top view for ecoflex matrix composite with circular fiber cross-section of different fiber angles

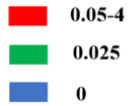








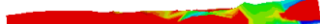
Soft composite in top view	Contour plots for early stage deformation	Contour plots for middle stage deformation	Contour plots for final deformation  Von Mises Stress (MPa) 
Fiber angle 60° case	 Axial stretch is 1.05	 Axial stretch is 1.1	 Axial stretch is 1.19
Fiber angle 45° case	 Axial stretch is 1.21	 Axial stretch is 1.54	 Axial stretch is 1.81
Fiber angle 30° case	 Axial stretch is 1.52	 Axial stretch is 1.92	 Axial stretch is 2.16

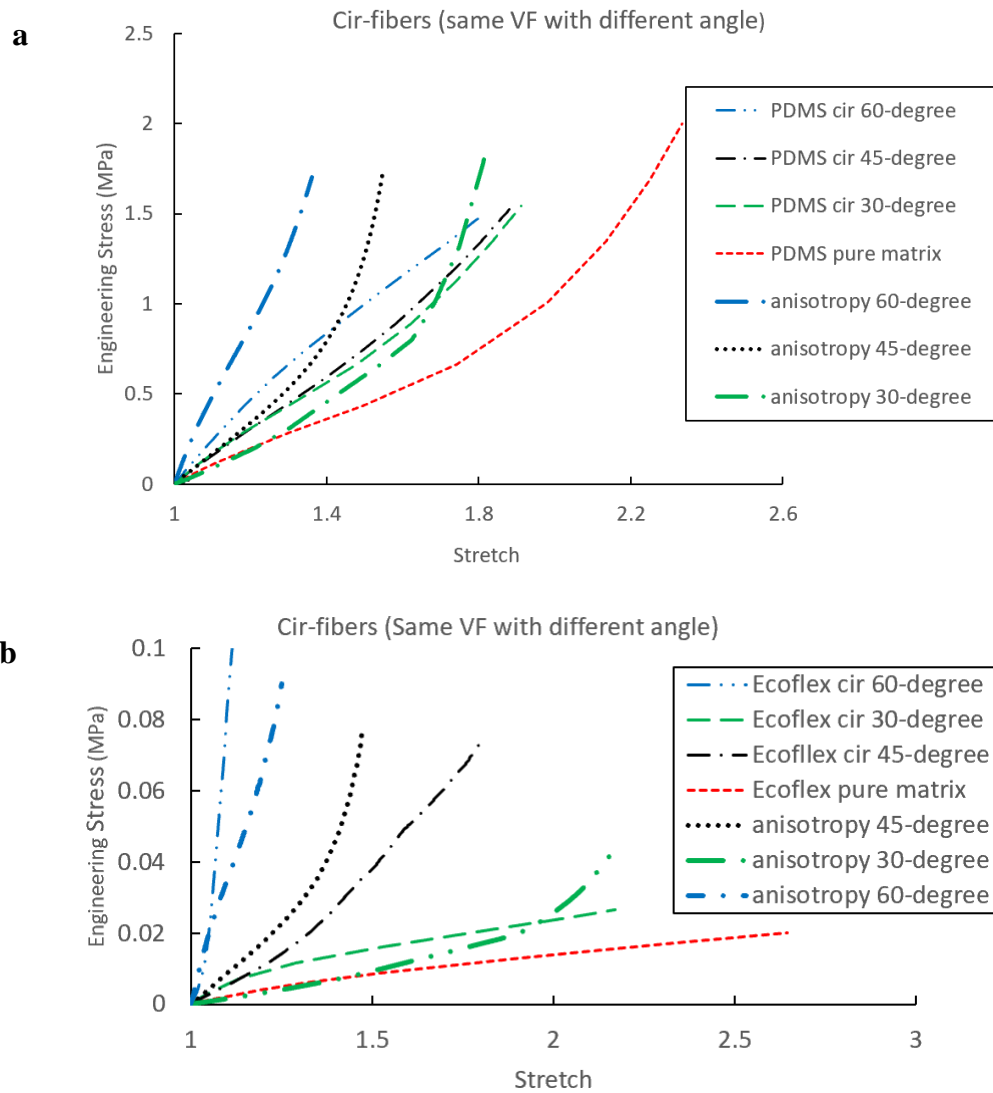
Table 2, 3 and 4, 5 are the simulation results of soft matrix made of PDMS and EcoFlex 00-30 respectively. Both PDMS and ecoflex matrix cases shows fiber angle does affect the results significantly in the fiber angle changes. Since the fibers play predominate role in the overall response of composite, the shear is significant for all fiber angles cases of ecoflex. The response of the composite with fiber angle 30 degree

is more similar to the uniaxial tension of soft matrix only because the initial fiber angle is small. For table 3, insignificant twisting exhibit for top views because of extension-shear-bending coupling. Therefore, the response of composite depends on both fiber angle and soft matrix material. Between those two soft materials, the results of 30 degree is significantly different that the stretch of EcoFlex is larger than PDMS. This can be explained by the fact that the Ecoflex is softer and soft material is predominant in the composite of 30 degree. The response of the composite with fiber angle 30 degree is more similar to the uniaxial tension of soft matrix only. On the contrary, the 60 degree is the opposite that the hard inclusion is predominant overall strength of composite, so the stretch is small under large stress. These two cases depicts the significant effect of fiber angle and soft material on the response of the composite and in the design of composite. It can be observed from the tables above, the fiber orientation rotates as the tensile stress increase and aligned to tensile direction, which affects the overall response of the composite. Both tables 2 and 4 present shearing, and the model using ecoflex as soft matrix can be shearing easier than PDMS.

In addition to the simulation results for the soft composites with detailed fiber architecture (heterogeneous materials), a constitutive model for anisotropic elastic responses of a homogeneous medium is also considered in examining the overall uniaxial responses for the PDMS and ecoflex composites with fiber angles: 30°, 45° and 60°. For this purpose, a homogeneous plate model with the same dimension as the composite model is generated. A constitutive material model developed in chapter 2 is used. In order to compare the mechanical response of anisotropic model, the material

parameters are calibrated by the uniaxial tension of the soft composite with PDMS 30° fiber angle, which is  $\mu = 0.017MP$ ,  $J_m = 14$ ,  $K = 2000$ ,  $K_1 = 0.8MPa$  and  $K_2 = 18$  for the ecoflex anisotropic case, and  $\mu = 0.65MPa$ ,  $J_m = 5.0$ ,  $K = 2000$ ,  $K_1 = 0.8MPa$  and  $K_2 = 18$  for PDMS anisotropic case. where  $K_1$  and  $K_2$  are two material constants presented in equation 2.5.

Fig. 20 presents the uniaxial response of the composites from the heterogeneous and anisotropic homogeneous models. The anisotropic response of the model shows similar responses with the composite models. In anisotropic model, the fibers reorientation is allowed by deformation gradient, but fiber volume fraction cannot be defined. The anisotropic model shows stiffening behavior but the response in soft composites did not show stiffening behavior. From experiment [21], higher volume fraction (higher than 60%) of soft composite, obvious stiffening behavior will exhibit. We will need run simulation of a higher fiber volume fraction (around 60%) to match anisotropic model in future work.

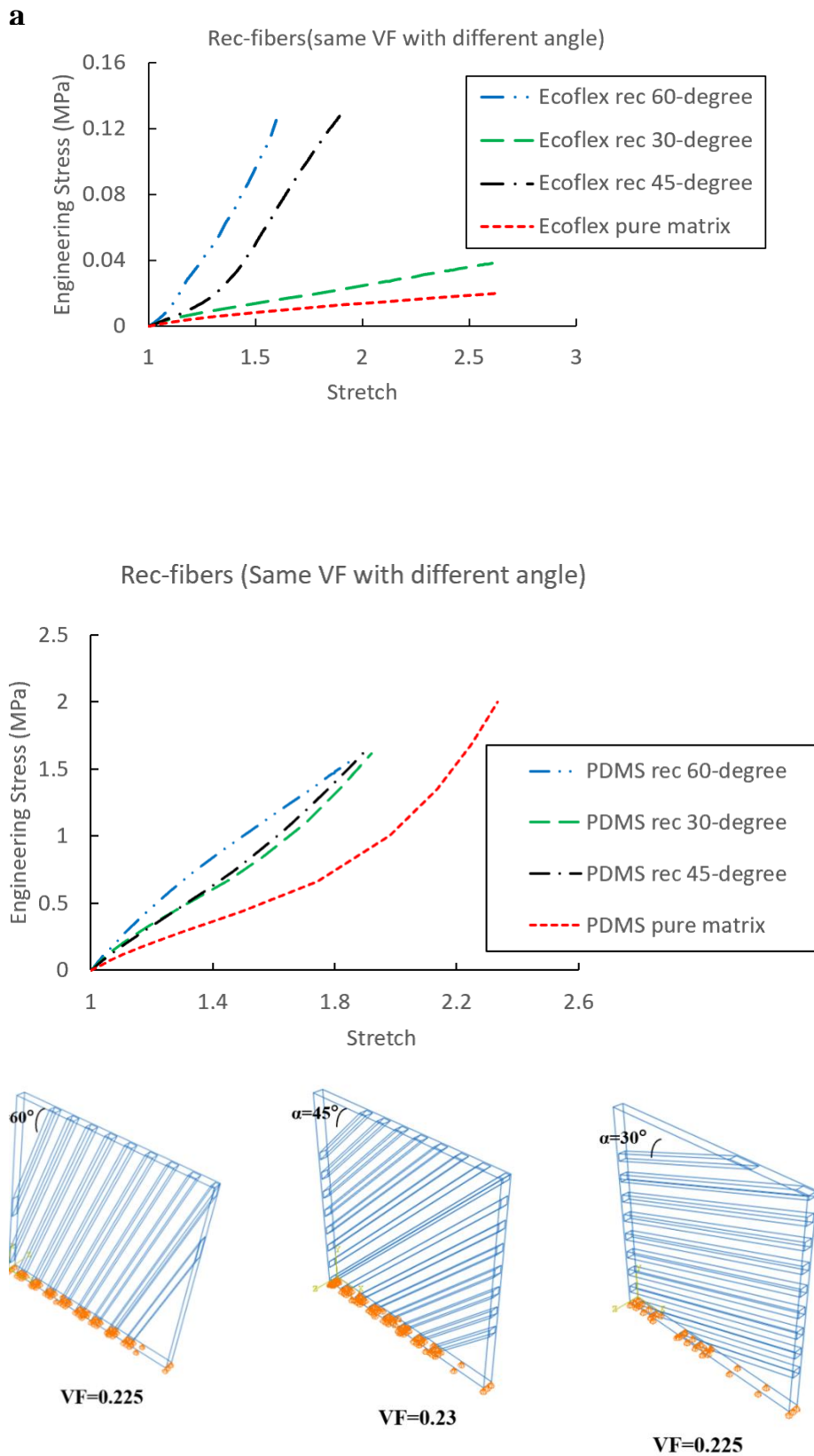


**Figure 20.** Engineering stress versus stretch for embedded circular fiber model with different fiber angle and soft matrix materials: (a) PDMS, (b) Ecoflex.

Case 2 presents uniaxial responses of the soft composites with different fiber angles of the same fiber volume fraction with rectangular fiber shape. The fiber volume fraction in the three models are maintained around 0.23. Figure 21 summarizes the overall stress-stretch responses of the composites for PDMS and ecoflex matrix. For the PDMS matrix composites, it shows that the shape of fiber does not influence the overall response of the composites. However, for the very soft ecoflex, the shape of the

fiber cross-section affects the overall responses of the composites. It is seen that the effect of fiber angles on the overall mechanical behavior of soft composite is significant very similar to circular fiber shape case, except for 60° fiber angle case. The curve of 60 ° fiber angle rectangular fiber shape composite is less stiff than in the same fiber angle of circular fiber case. The reason will be found out in the contour plots later. For PDMS, the effect of fiber angles and fiber shape on soft composite is insignificant. The results are very similar to PDMS with circular fiber shape case.

To better illustrate the simulation results, we show stress contours at different stretches, shown in table 4 and 5. From the two cases, the overall engineering stress versus stretch plots show similar curve. When the fiber angle is 60 degree, the two models deform insignificantly because the fibers restrict elongation of the plate. On the contrary, the stretch of plate is very large for 30-degree fiber angle since the small fiber angle allow large displacement in the direction of loading. The result of the model is more similar to the plate without fibers. For the 45-degree fiber angle, the embedded rectangular fiber shows significant twist while the circular fiber remains flat, and both models have large stress around the diagonal fiber. For rectangular case, the twist shows at small stretch (1.36) and the stress in diagonal direction become larger.

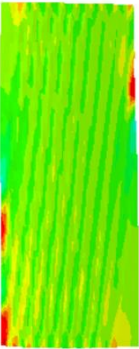
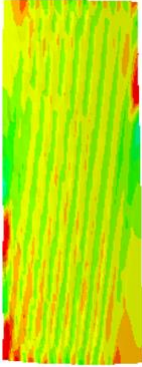
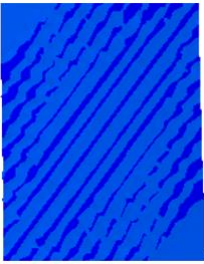
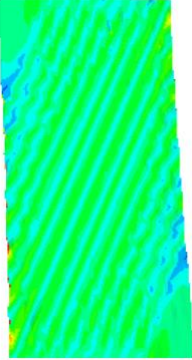
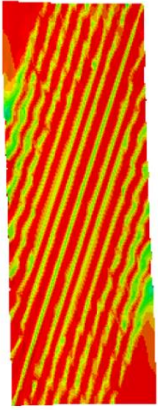


**Figure 21.** The soft composite model for composite of circular fiber shape of different fiber angles. (a) Contour plots for PDMS (b) Contour plots for EcoFlex 00-30 (c) Schemes for composite with rectangular fiber cross-section of different fiber angles

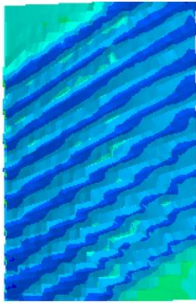
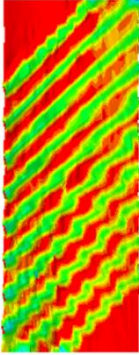
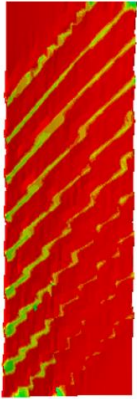
Table 6, 7 and 8, 9 depict the contour plots of soft matrix made of PDMS and EcoFlex 00-30, respectively. For table 6, The response of the composite with rectangular fiber angle is similar to that with circular fiber shape. We can conclude that for PDMS the soft matrix has predominate effect on the overall behavior of the soft composites. For ecoflex, the fiber shape and orientation largely affect overall behavior because it's too soft to prevent fiber from rotating to the loading direction. For table 7, insignificant twisting and bending exhibit for the three cases. For table 8 and 9, the ecoflex composites with 45- and 60-degree fiber angle, fiber reorientations are shown during loading. Particularly for the composites with 45° fiber angle, Significant twisting exhibit 45-degree case. It is understandable that the 45-degree cause relatively large stiffness matrix and shear and bending deformation. However, the bending effect is too significant. For 60-degree case, large stress occurs at the diagonal of the composite. Our hypothesis is the stress concentration occurs at corner of rectangular fiber which results in numerical instability in this model and inaccurate deformation result. The results of 30 degree is more similar to that with circular fiber shape.



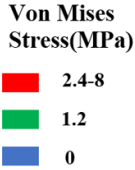

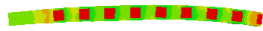
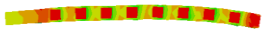

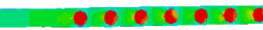
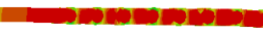



**Table 6** Contour plots in front view for PDMS matrix composite with rectangular fiber cross-section of different fiber angles

Soft composite with circular fiber cross-section in front view	Contour plots for early stage deformation	Contour plots for middle stage deformation	Contour plots for final deformation  Von Mises Stress(MPa) <div style="display: flex; flex-direction: column; align-items: center;"> <div style="display: flex; align-items: center; margin-bottom: 5px;"><span style="width: 15px; height: 10px; background-color: red; margin-right: 5px;"></span> 2.4-8</div> <div style="display: flex; align-items: center; margin-bottom: 5px;"><span style="width: 15px; height: 10px; background-color: green; margin-right: 5px;"></span> 1.2</div> <div style="display: flex; align-items: center;"><span style="width: 15px; height: 10px; background-color: blue; margin-right: 5px;"></span> 0</div> </div>
Fiber angle 60° case	 Axial stretch is 1.38	 Axial stretch is 1.59	 Axial stretch is 1.74
Fiber angle 45° case	 Axial stretch is 1.25	 Axial stretch is 1.64	 Axial stretch is 1.81

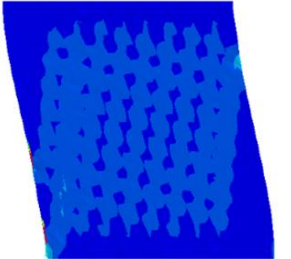
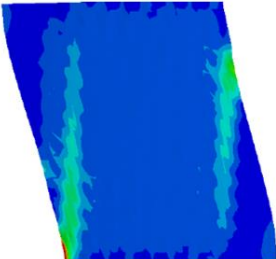
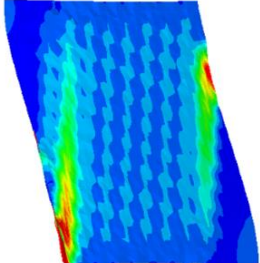
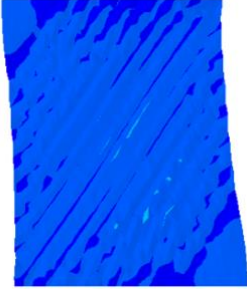
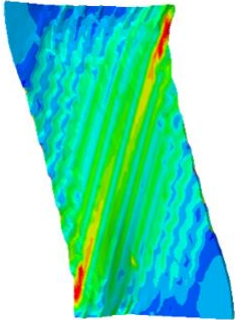
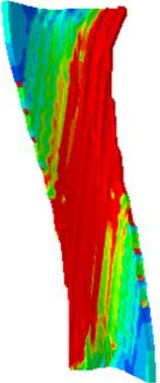
**Table 6** Continued

Soft composite with circular fiber cross-section in front view	Contour plots for early stage deformation	Contour plots for middle stage deformation	Contour plots for final deformation  <b>Von Mises Stress(MPa)</b> <span style="color: red;">■</span> 2.4-8 <span style="color: green;">■</span> 1.2 <span style="color: blue;">■</span> 0
Fiber angle 30° case	 <p data-bbox="469 1301 735 1339">Axial stretch is 1.32</p>	 <p data-bbox="772 1301 1038 1339">Axial stretch is 1.62</p>	 <p data-bbox="1062 1301 1329 1339">Axial stretch is 1.83</p>

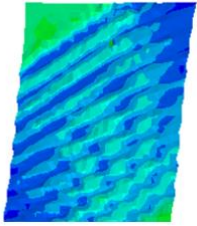
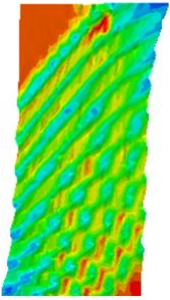
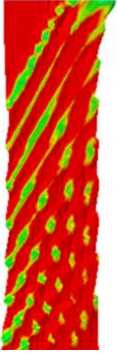
**Table 7** Contour plots in top view for PDMS matrix composite with rectangular fiber cross-section of different fiber angles

Soft composite in top view	Contour plots for early stage deformation	Contour plots for middle stage deformation	Contour plots for final deformation  Von Mises Stress(MPa) 
Fiber angle 60° case	 Axial stretch is 1.38	 Axial stretch is 1.59	 Axial stretch is 1.74
Fiber angle 45° case	 Axial stretch is 1.25	 Axial stretch is 1.64	 Axial stretch is 1.81
Fiber angle 30° case	 Axial stretch is 1.32	 Axial stretch is 1.62	 Axial stretch is 1.83




**Table 8** Contour plots in front view for ecoflex matrix composite with rectangular fiber cross-section of different fiber angles

Soft composite in front view	Contour plots for early stage deformation	Contour plots for middle stage deformation	Contour plots for final deformation  Von Mises Stress(MPa) <div style="display: flex; flex-direction: column; align-items: center;"> <div style="display: flex; align-items: center; margin-bottom: 2px;"><span style="width: 15px; height: 10px; background-color: red; margin-right: 5px;"></span> 0.05-2.2</div> <div style="display: flex; align-items: center; margin-bottom: 2px;"><span style="width: 15px; height: 10px; background-color: green; margin-right: 5px;"></span> 0.025</div> <div style="display: flex; align-items: center;"><span style="width: 15px; height: 10px; background-color: blue; margin-right: 5px;"></span> 0</div> </div>
Fiber angle 60° case	 Axial stretch is 1.25	 Axial stretch is 1.36	 Axial stretch is 1.59
Fiber angle 45° case	 Axial stretch is 1.51	 Axial stretch is 1.67	 Axial stretch is 1.81


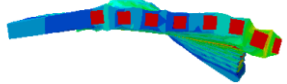
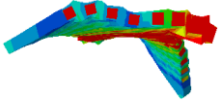



**Table 8** Continued

Soft composite in front view	Contour plots for early stage deformation	Contour plots for middle stage deformation	Contour plots for final deformation  Von Mises Stress(MPa) 0.05-2.2 0.025 0
Fiber angle 30° case	 <p data-bbox="435 1059 695 1093">Axial stretch is 1.61</p>	 <p data-bbox="770 1093 1031 1126">Axial stretch is 1.95</p>	 <p data-bbox="1098 1081 1358 1115">Axial stretch is 2.56</p>

**Table 9** Contour plots in top view for ecoflex matrix composite with rectangular fiber cross-section of different fiber angles

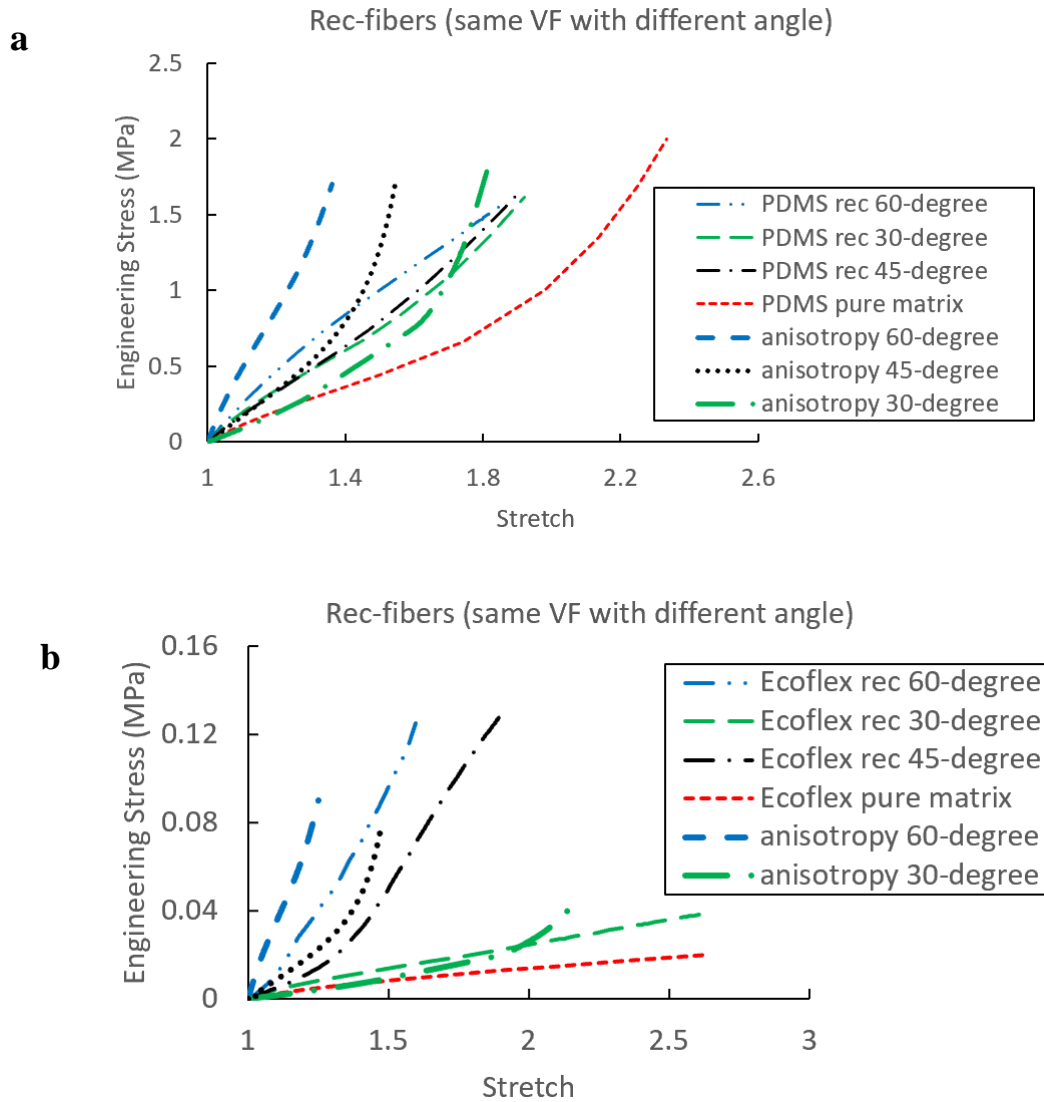
Soft composite in top view	Contour plots for early stage deformation	Contour plots for middle stage deformation	Contour plots for final deformation  Von Mises Stress(MPa) 0.05-2.2 0.025 0
Fiber angle 60° case	 <p data-bbox="440 1888 703 1921">Axial stretch is 1.25</p>	 <p data-bbox="791 1888 1054 1921">Axial stretch is 1.36</p>	 <p data-bbox="1137 1888 1401 1921">Axial stretch is 1.59</p>

**Table 9** Continued

Soft composite in top view	Contour plots for early stage deformation	Contour plots for middle stage deformation	Contour plots for final deformation  Von Mises Stress(MPa) 0.05-2.2 0.025 0
Fiber angle 45° case	 <p>Axial stretch is 1.51</p>	 <p>Axial stretch is 1.67</p>	 <p>Axial stretch is 1.81</p>
Fiber angle 30° case	 <p>Axial stretch is 1.61</p>	 <p>Axial stretch is 1.95</p>	 <p>Axial stretch is 2.56</p>

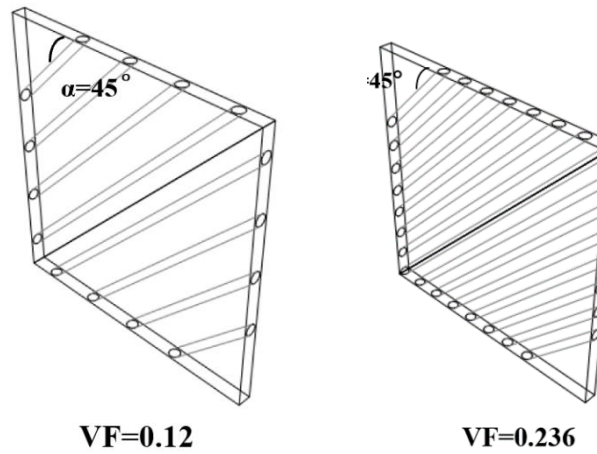
Furthermore, the responses of the composite with square fiber cross-section are also compared to the ones determined from the homogeneous anisotropic model, as shown in Fig. 22. The figure 22(a) is very similar with Figure 20(a) which means that the fiber shape does not affect the mechanical behavior of the composite. For the ecoflex, the Fig. 22(b) is also similar to Fig 20(b) except the 45-degrees model that the model of rectangular fiber with 45 degrees have stress localization in diagonal corner and the result is not reliable. When the stretches of PDMS are around 1.5, the results of EcoFlex vary largely based on different fiber angles. The engineering stress of PDMS composite is around 1.7 MPa compared with 0.13MPa the largest stress Ecoflex can reach. For PDMS the results of the three fiber angles show similar trend. For Ecoflex,

the fiber angle in 60 degree is similar to 45 degree much stiffer than 30 degree. The reason can be same as previous case that the hard inclusion predominately make deformation harder as the fiber angle rotate to the tension direction for ecoflex.



**Figure 22.** Engineering stress versus stretch for embedded rectangular fiber model with different fiber angle and soft matrix materials: (a) PDMS, (b) Ecoflex. (c) Schemes for composite with circular fiber cross-section of different VF

**c**



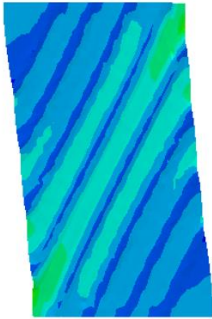
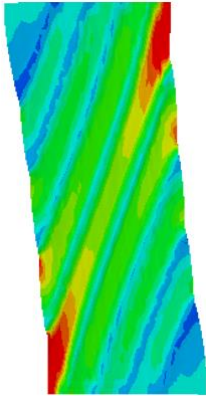
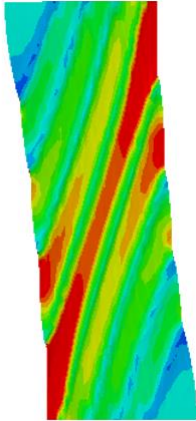
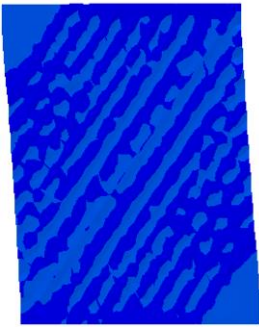
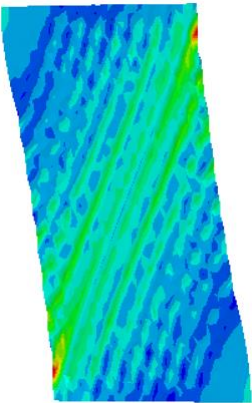
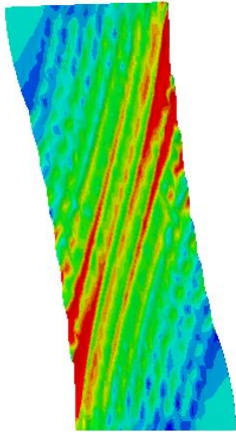
**Figure 22** Continued.

Case 3 is a comparison between different fiber volume fractions in the same fiber angles for composite of rectangular fiber and circular fiber under uniaxial tension.







The stress contour plots of soft composite of different volume fraction (VF) at certain stretch for both circular and rectangular fiber are presented in Table 10-13, which gives us more information on the deformation. The simulation results show similar contours for different fiber volume fraction, which match the engineering stress-stretch plots shown in figure 23.



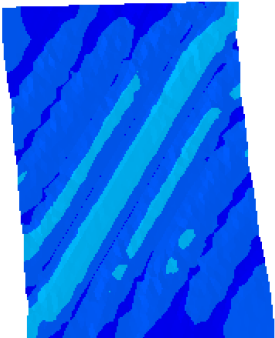
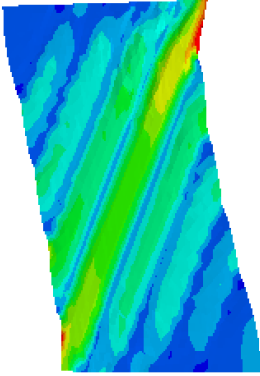
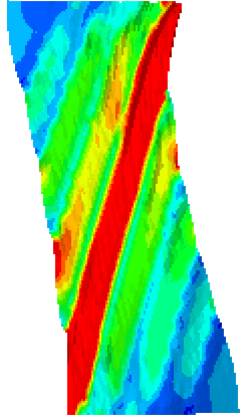
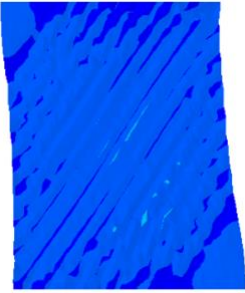
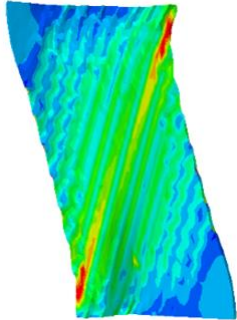
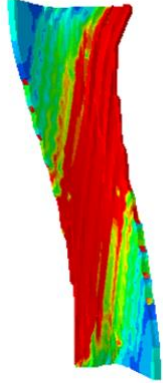
**Table 10** Contour plots in front view for ecoflex matrix composite with circular fiber cross-section of different volume fractions

Soft composite in front view	Contour plots for early stage deformation	Contour plots for middle stage deformation	Contour plots for final deformation  Von Mises Stress (MPa) <div style="display: flex; justify-content: space-around; font-size: small;"> <span style="color: red;">■</span> 0.05-6</div> <div style="display: flex; justify-content: space-around; font-size: small;"> <span style="color: green;">■</span> 0.025</div> <div style="display: flex; justify-content: space-around; font-size: small;"> <span style="color: blue;">■</span> 0         </div>
Small VF	 Axial stretch is 1.35	 Axial stretch is 1.56	 Axial stretch is 1.81
Large VF	 Axial stretch is 1.21	 Axial stretch is 1.54	 Axial stretch is 1.81





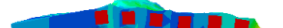
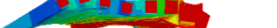
**Table 11** Contour plots in top view for ecoflex matrix composite with circular fiber cross-section of different volume fractions

Soft composite in top view	Contour plots for early stage deformation	Contour plots for middle stage deformation	Contour plots for final deformation  Von Mises Stress (MPa) <div style="display: flex; justify-content: space-around; font-size: small;"> <span style="color: red;">■</span> 0.05-6</div> <div style="display: flex; justify-content: space-around; font-size: small;"> <span style="color: green;">■</span> 0.025</div> <div style="display: flex; justify-content: space-around; font-size: small;"> <span style="color: blue;">■</span> 0         </div>
Small VF	 Axial stretch is 1.35	 Axial stretch is 1.56	 Axial stretch is 1.81
Large VF	 Axial stretch is 1.21	 Axial stretch is 1.54	 Axial stretch is 1.81

**Table 12** Contour plots in front view for ecoflex matrix composite with rectangular fiber cross-section of different volume fractions

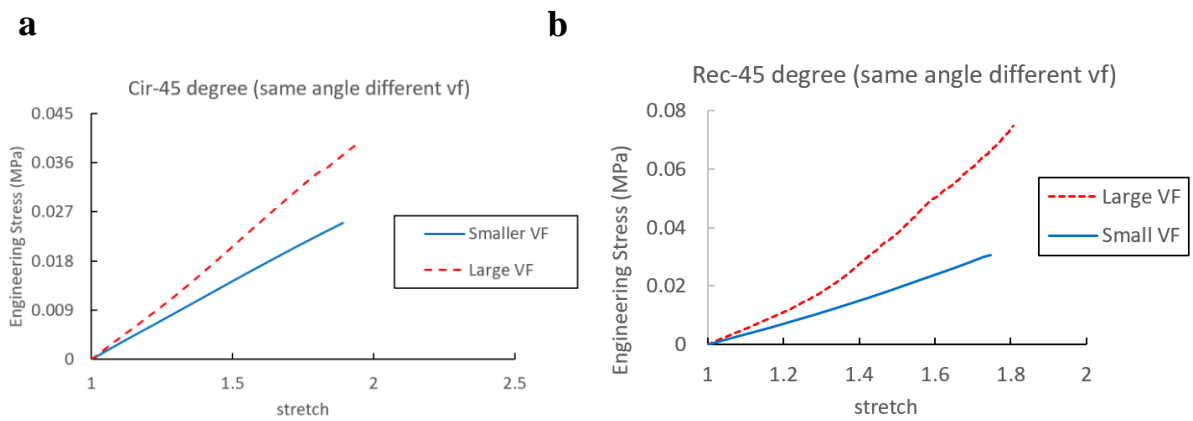
Volume fraction (VF) scheme for soft composite in front view	Contour plots for early stage deformation	Contour plots for middle stage deformation	Contour plots for final deformation  Von Mises Stress(MPa) <div style="display: flex; flex-direction: column; align-items: center;"> <div style="display: flex; align-items: center; margin-bottom: 2px;"><span style="width: 15px; height: 10px; background-color: red; margin-right: 5px;"></span> 0.05-4</div> <div style="display: flex; align-items: center; margin-bottom: 2px;"><span style="width: 15px; height: 10px; background-color: green; margin-right: 5px;"></span> 0.025</div> <div style="display: flex; align-items: center;"><span style="width: 15px; height: 10px; background-color: blue; margin-right: 5px;"></span> 0</div> </div>
Small VF	 <p style="text-align: center;">Axial stretch is 1.35</p>	 <p style="text-align: center;">Axial stretch is 1.54</p>	 <p style="text-align: center;">Axial stretch is 1.77</p>
Large VF	 <p style="text-align: center;">Axial stretch is 1.31</p>	 <p style="text-align: center;">Axial stretch is 1.47</p>	 <p style="text-align: center;">Axial stretch is 1.78</p>

**Table 13** Contour plots in top view for ecoflex matrix composite with rectangular fiber cross-section of different volume fractions

Volume fraction (VF) scheme for soft composite in top view	Contour plots for early stage deformation	Contour plots for middle stage deformation	Contour plots for final deformation  Von Mises Stress(MPa) <div style="display: flex; flex-direction: column; align-items: center;"> <div style="display: flex; align-items: center; margin-bottom: 2px;"><span style="width: 15px; height: 10px; background-color: red; margin-right: 5px;"></span> 0.05-4</div> <div style="display: flex; align-items: center; margin-bottom: 2px;"><span style="width: 15px; height: 10px; background-color: green; margin-right: 5px;"></span> 0.025</div> <div style="display: flex; align-items: center;"><span style="width: 15px; height: 10px; background-color: blue; margin-right: 5px;"></span> 0</div> </div>
Small VF	 Axial stretch is 1.35	 Axial stretch is 1.54	 Axial stretch is 1.77
Large VF	 Axial stretch is 1.31	 Axial stretch is 1.47	 Axial stretch is 1.78

Tables 10, 11 and 12, 13 represents the soft composite model with ecoflex matrix and 45-degree fiber angle in Abaqus with volume fraction: 0.23 and 0.12 for comparison. The boundary conditions are defined as previous cases. The responses from circular fiber show similar result while the rectangular ones differ because of twisting shown previously. For table 10, 11, insignificant twisting and bending exhibit for both VF case. The extension strain and shear strain are the same for both cases. The deformation matches the engineering stress versus stretch plot that higher VF require

larger stress. It is understandable that higher VF increase the stiffness matrix. For table 12 and 13, insignificant twisting and bending exhibit for the small VF case is because small VF is softer and easier to elongate and significant twisting is expected when stretch goes larger. Again, the accuracy of high VF model is still arguable and more details need to be clarified.



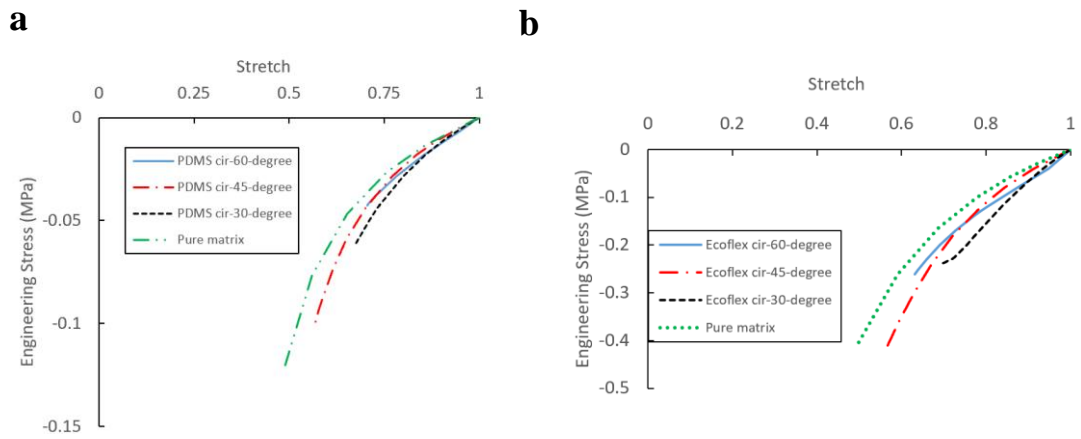
**Figure 23.** Engineering stress versus stretch for the same fiber angle (45) with different volume fraction (VF) and soft matrix materials: (a) circular fiber model, (b) rectangular fiber model.

From Fig. 23 we can observe the higher volume fraction model have bigger stress under same stretch, which can be expected that the hard fiber strengthens the composite and more fiber inclusions induce higher stiffness. The large volume fraction (0.23) is almost twice larger than the small one (0.12). From figure 23 (a) and (b), it should be noted that the high and low volume fraction model have similar trend in both figures. In Figure 23 (b), the stress in high fiber fraction model is almost twice as much as the low volume fraction but less twice in figure 23 (a), which illustrate the 45-degree fiber angle with ecoflex matrix may not reliable mentioned previously.

Case 4 is a comparison between different fiber angles in the same fiber volume fraction for composite of rectangular fiber shape under uniaxial compression. Besides uniaxial tension, we investigated the response of both Ecoflex and PDMS under uniaxial compression in same boundary condition. Both Fig. 24 (a) and (b) shows the similar trend for different fiber angle and different soft material under uniaxial compression. The mechanical response of matrix is similar to the composite response, and the composite results in slightly stiffer than pure matrix though. We can observe the fiber angle has insignificant effect on uniaxial compression, which can be explained that the mechanical response of compression and tension for the hyperelastic model is asymmetric and becomes stiffer for compression so the stiffness difference between fiber and matrix is small. The soft matrix play dominant role for compression. The stress contours at certain stretches in table 15 and 16 provides us with more information on the deformation. The contours revealed that the fiber orientation is in the opposite direction to the loading direction and fibers do not largely affect the behavior of composite. Table 14 reveal that the angle changes for PDMS and ecoflex are not significant.


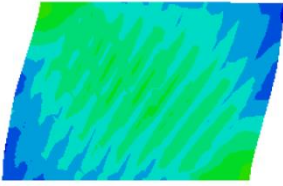
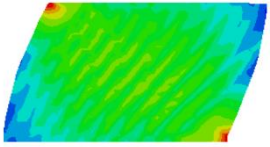
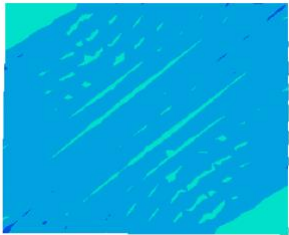
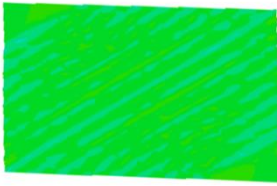
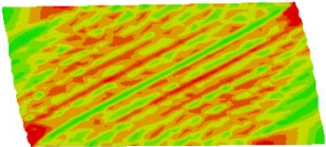
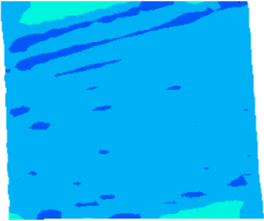
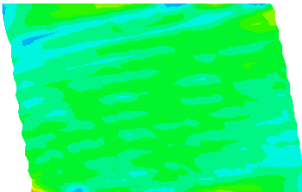
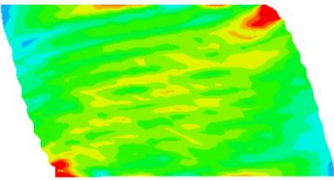
**Table 14** Fiber angles changes ( $\Delta \alpha$ ) with PDMS and EcoFlex matrix for different initial fiber angles

matrix \ Initial angle	PDMS	Ecoflex
30°	-11.5°	-13.6°
45°	-17.3°	-14.7°
60°	-15.6°	-15.5°




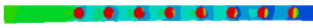
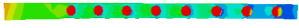


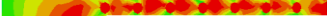


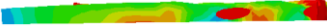
**Figure 24.** Engineering stress versus stretch for the same volume fraction (VF) with different fiber angle and soft matrix materials: (a) PDMS, (b) Ecoflex.

**Table 15** Different fiber angles in the same VF for composite of circular fiber shape under uniaxial compression in front view.

Soft composite in front view	Contour plots for early stage deformation	Contour plots for middle stage deformation	Contour plots for final deformation  Von Mises Stress (MPa) ■ 1-6.9 ■ 0.5 ■ 0
Fiber angle 60° case	 <p>Axial stretch is 0.9</p>	 <p>Axial stretch is 0.65</p>	 <p>Axial stretch is 0.6</p>
Fiber angle 45° case	 <p>Axial stretch is 0.85</p>	 <p>Axial stretch is 0.7</p>	 <p>Axial stretch is 0.55</p>
Fiber angle 30° case	 <p>Axial stretch is 0.8</p>	 <p>Axial stretch is 0.76</p>	 <p>Axial stretch is 0.65</p>

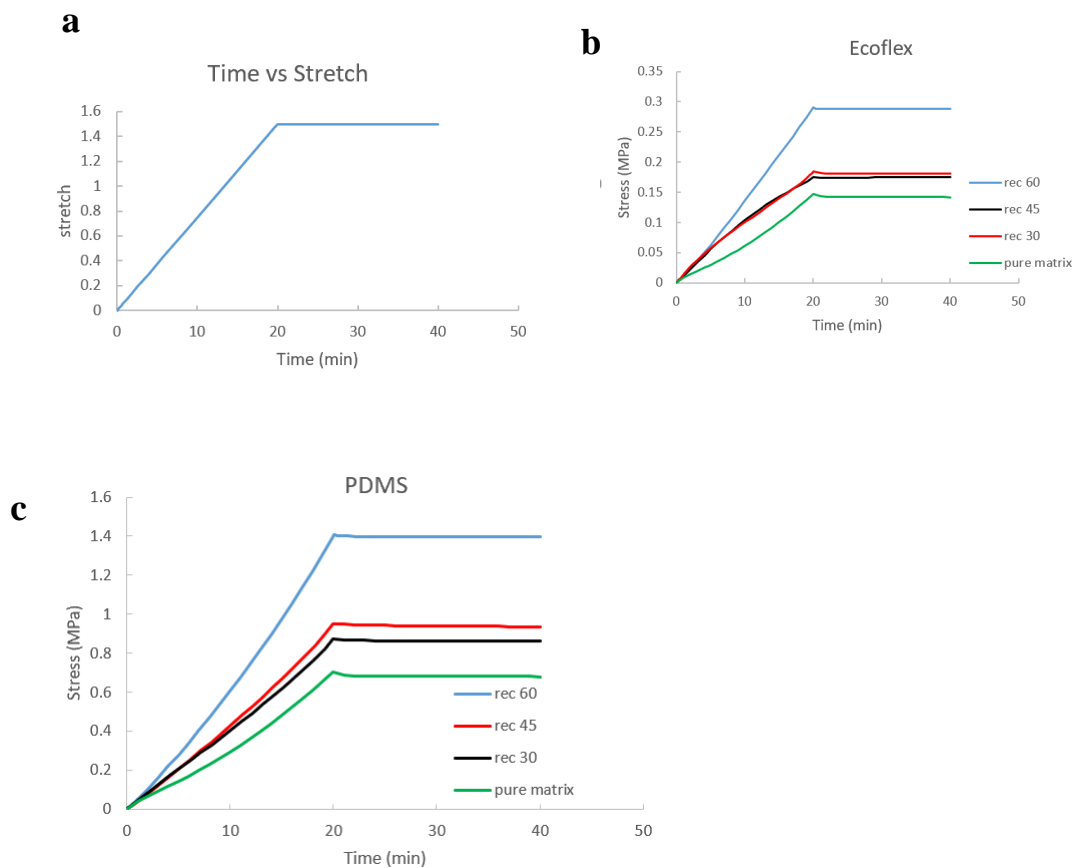


**Table 16** Different fiber angles in the same VF for composite of circular fiber shape under uniaxial compression in top view.

Soft composite in top view	Contour plots for early stage deformation	Contour plots for middle stage deformation	Contour plots for final deformation  Von Mises Stress (MPa) ■ 1-6.9 ■ 0.5 ■ 0
Fiber angle 60° case	 Axial stretch is 0.9	 Axial stretch is 0.65	 Axial stretch is 0.6
Fiber angle 45° case	 Axial stretch is 0.85	 Axial stretch is 0.7	 Axial stretch is 0.55
Fiber angle 30° case	 Axial stretch is 0.8	 Axial stretch is 0.76	 Axial stretch is 0.65

## 4.2. Uniaxial Response of Viscoelastic Soft Composites

In this section, the influence of viscoelastic matrix on the uniaxial response of soft composites is examined. First the simulation of uniaxial tension was performed. All boundary condition and material parameters are the same. The software OriginPro 2015 is applied to digitize the experimental data and find the optimal parameter values. The calibrated material parameters based on experiment conducted by Jennifer et al. [63] are the characteristic relaxation time  $\tau = 3$  min and the value of  $\frac{\mu_{\infty}}{\mu_a} = 0.75$ .



**Figure 25.** Time vs stretch and stress for soft composite with PDMS and ecoflex matrix under uniaxial tension.

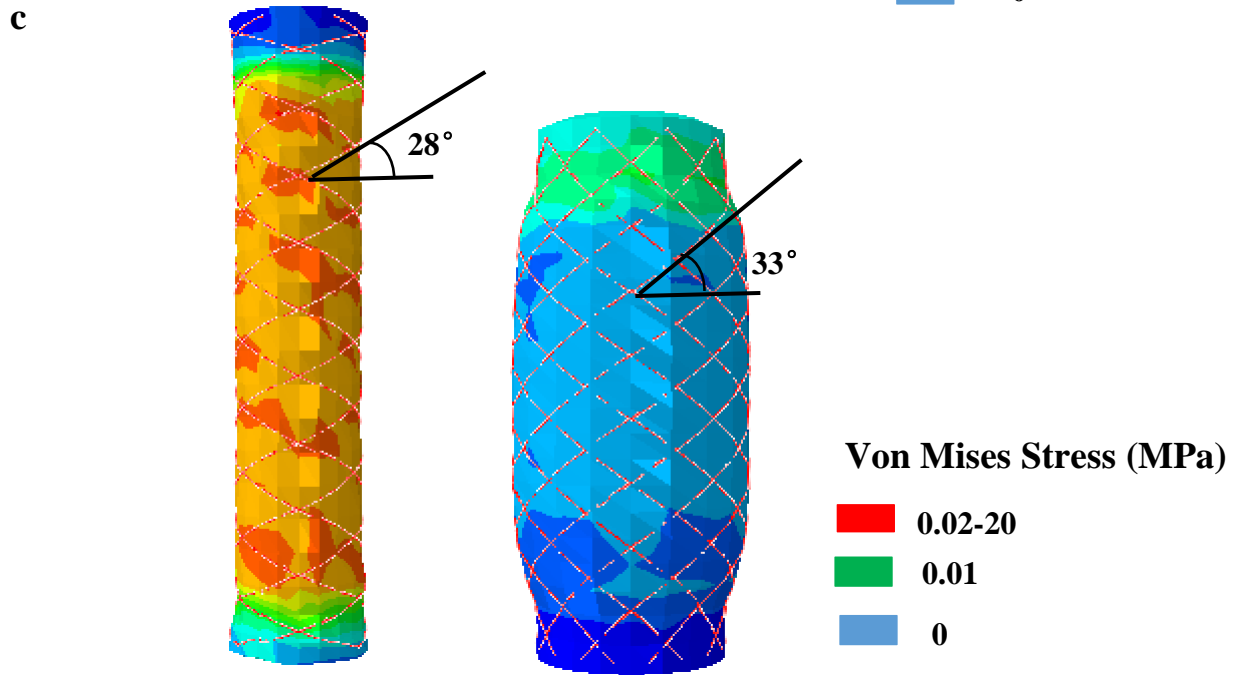
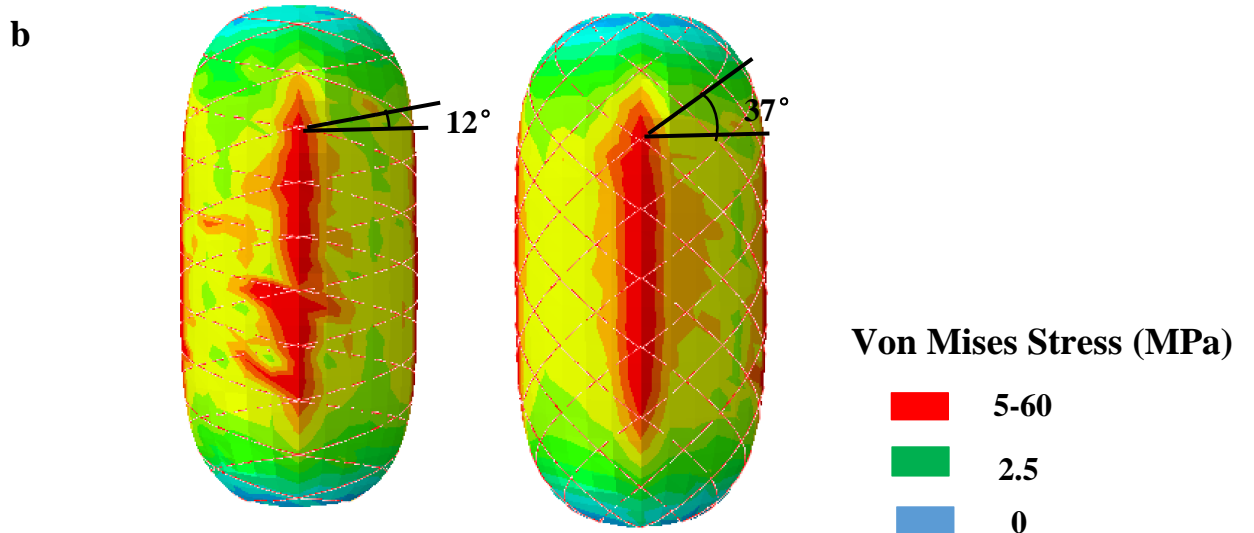
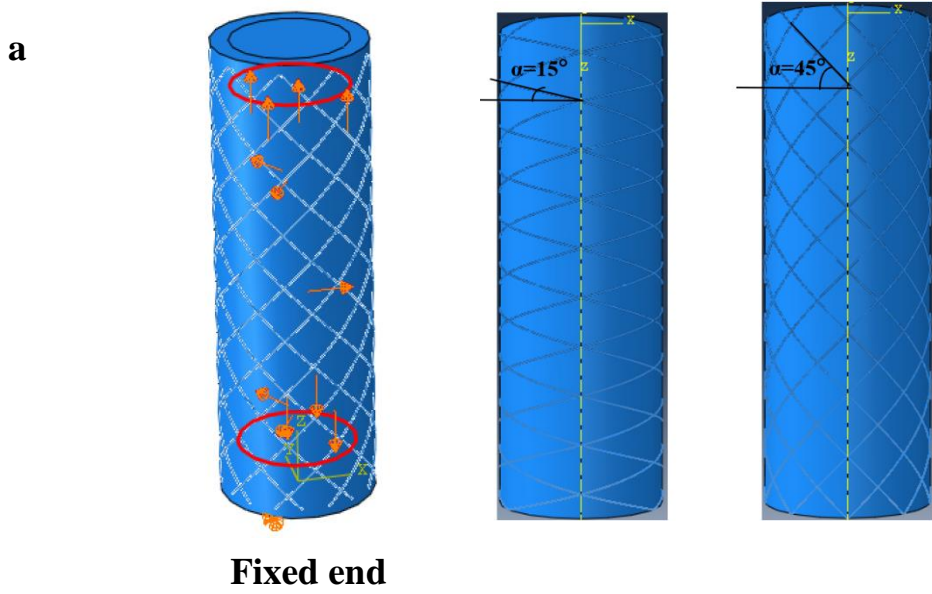
The composite is stretch along tension direction for 20 seconds till the stretch ratio of 1.5 and then hold stretch unchanged for another 20 seconds shown as Fig. 25 (a). The mechanical responses of the soft composite are shown in Fig. 25 (b) and (c). The material parameters are the same as previous section. Stress relaxation is presented for different fiber orientation cases and matrix material. The short relaxation response in each soft composite shows good agreement with the result from pure matrix. The viscoelastic effect in the soft composite is not very large since the fibers that bear most of the load are not viscoelastic.

### **4.3. Structural Analysis**

In this section, the composite model is used to simulate responses of composite structures, relevant for pneumatic soft robotics applications. In the first example, pressurized composite cylinders with different fiber angles under internal pressure are studied. Composite cylinders with both PDMS and ecoflex matrix with viscoelastic behavior are considered. Figure 26 (a) illustrates the composite geometrical models with different fiber angles. The double helix fiber is tied on the outer surface of tube at a prescribed angle  $\alpha$ . From Fig. 26 (b) PDMS is used as soft matrix and the contour plots shows insignificantly different between the tubes with 15 deg and 45 deg fiber angles, while Fig. 26 (c) presents different response that the tube contracts if the fiber angle  $\alpha$  is 15 degree and extends if angle  $\alpha$  is 45 degree. After the cylinder shrinks, the fiber angle becomes 28 degree while the angle turns into 33 degree for the 45-degree case. It is understandable that the decrease in the radial direction would result in

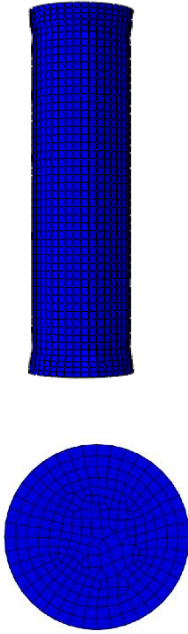
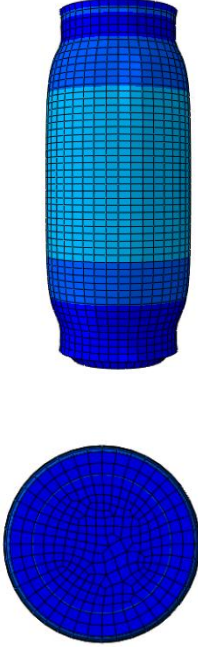
increase in fiber angle for 15-degree case and vice versa for 45-degree case. For the PDMS composite, the cylinder expands when inner pressure is applied as expected that the PDMS is stiffer compared to fiber. However, for the ecoflex case, the cylinder shrinks for 15-degree case, expand for 45-degree case. The fiber with 15-degree angle bear more load in the radial direction the cylinder will elongate in axial direction, while less radial constraint is caused by fiber, then the composite expands in the axial direction for 45-degree case. When designing the helix fiber embedded composite, soft material of resin matrix is an important factor besides fiber angle and ratio of outer radius to inner radius of tube. Inner pressure is applied to the inner surface of cylinder  $P=0.2$  MPa for PDMS composite and  $P=0.01$  MPa for the ecoflex composite.

Table 17 presents the deformed shapes of soft composites using the anisotropic model. Both heterogeneous and anisotropic model have the same geometrical parameters such as height, diameter and thickness. From this table of 15-degree case, both PDMS and ecoflex material, the cylinder shrinks in radial direction and elongate in longitudinal axis, which can be explained as the anisotropic model stiffen the response compared to fibers tied to the cylinder and anisotropic response in the model plays dominant role in the overall behavior. Therefore, the radial deformation is restricted, and large deformation is allowed in longitudinal direction for 15-degree case. For 45-degree case, since the anisotropic model results in stiffer response, the radial deformation is not as large as the one in figure 26.



**Figure 26.** (a) Fiber reinforced cylinder with 15 and 45 fiber angle and Comparison of von mises stress contour plot for different fiber angles and soft material (b) PDMS (c) Ecoflex

**Table 17** The contour plots of double helix fiber reinforced cylinder made of anisotropic model in front and top view.

	15°	45°
<p>PDMS</p> <p>Von Mises Stress (MPa)</p> <p>■ 5-60</p> <p>■ 2.5</p> <p>■ 0</p>		

**Table 17** Continued

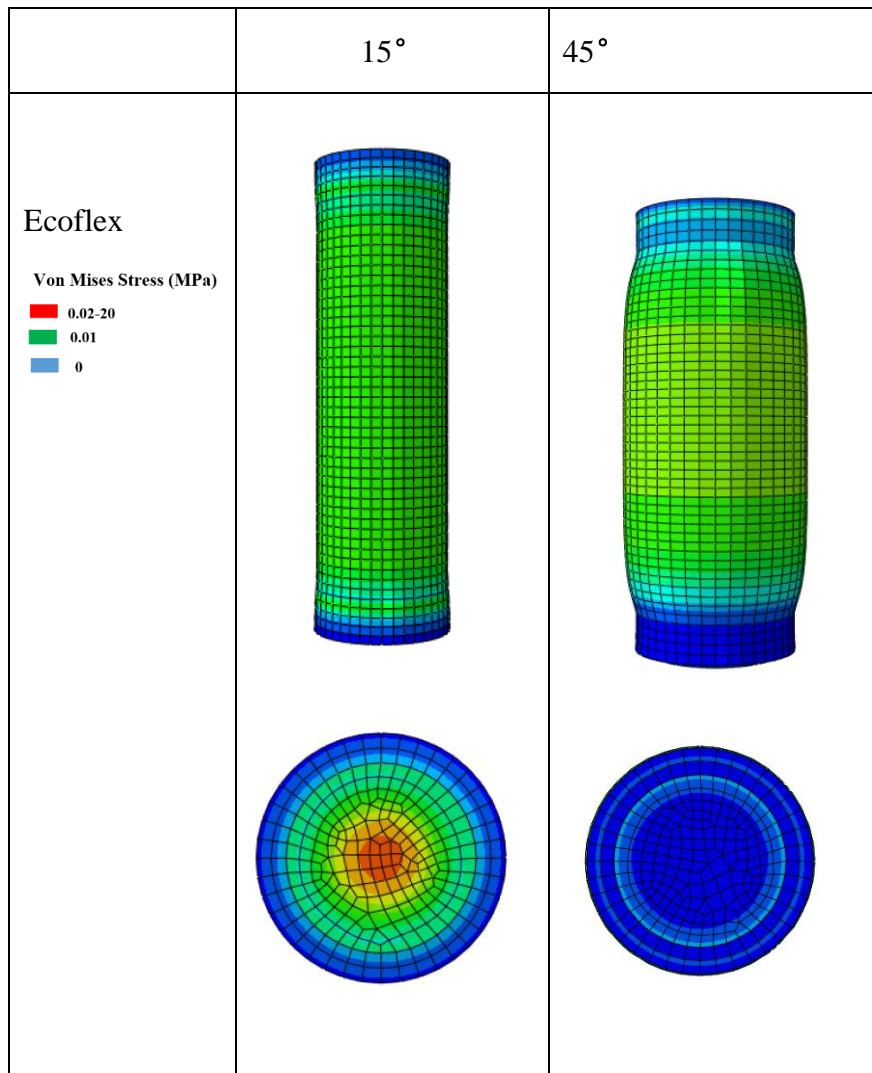
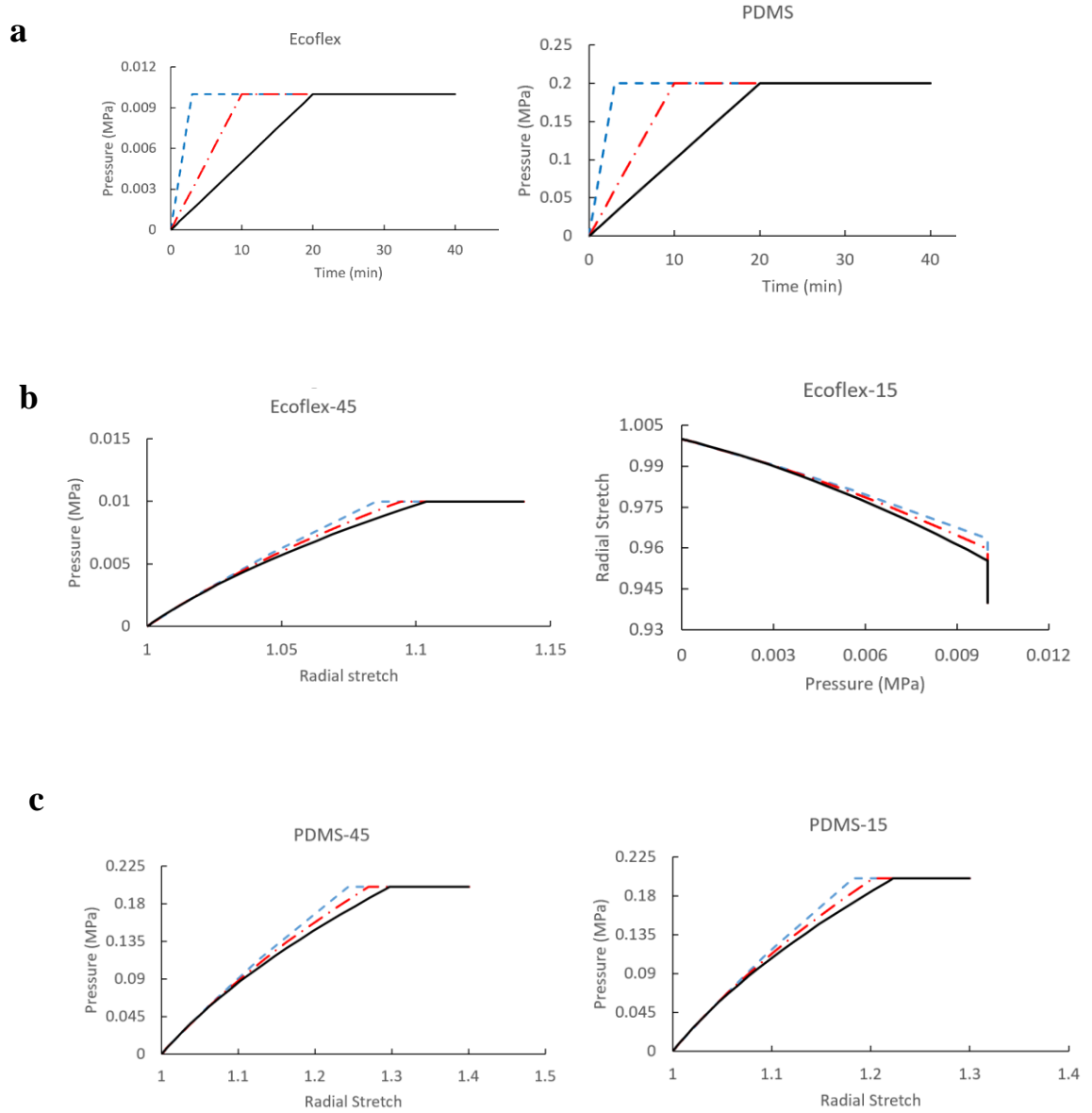


Fig. 27 shows the results of axial stretch of in the middle of cylinder under different loading rates. We assume relaxation time is 10 mins for the viscoelastic model. The loading ramps start from 0 to 3 mins, 10 mins and 20 mins are applied. Creep responses exhibit for each case, which means fibers will not restrict the viscoelastic behavior of matrix for different fiber angle and matrix material. Pressure versus radial stretch are

plotted in Fig. 27 b and c, the separate curves under different loading rates indicate the viscoelastic response exhibit as expected.



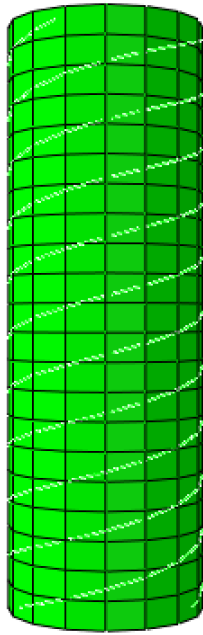
**Figure 27.** Time versus pressure and pressure versus axial stretch plots for different fiber angles and soft material (a)(e)(f) PDMS (a)(b)(c) Ecoflex

Then we built a single helix fiber reinforced cylinder made of PDMS and ecoflex. The same boundary conditions as the previous model are applied. The model is inspired by the study of uniaxial tension for unidirectional composite in section 4.1. Since a

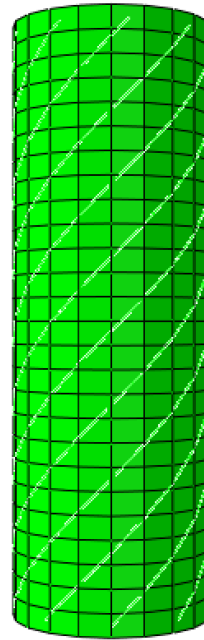


coupling of bending shearing and twisting behavior is exhibit in a uniaxial tension, the element in the cylinder with single fiber tied is experiencing biaxial tension. In this model, we want to explore the complex behavior of fiber reinforced composite in composite structures. Figure 28 and 29 present that Undeformed model of single helical fiber with coarse mesh and fine mesh separately for 15 and 45 fiber degree. Table 18 illustrates the contour plots of composite models made of PDMS and ecoflex with initial fiber angles 15 and 45 degree. In order to visualize the deformation, brick elements are used. By comparing the result in table 18, the result of simulation with refined mesh is shown in table 19. Even though the simulation with finer mesh is more accurate and less stiff, the results are similar, and we use the coarse mesh to visualize the twisting clearly. Significant twisting exhibit for both 15-degree fiber angle case and 45-degree case and this can be approximately explained as the elements with 45-degree and 15-degree fiber angle under two perpendicular same uniaxial tension loading induce two same shear forces toward fiber direction. For those two cases, both ecoflex and PDMS show significant twisting and soft ecoflex has larger deformation as expected. Table 20 reveals the contour plots with finer mesh of single helix fiber reinforced cylinder made of anisotropic model in front and top view. The results are similar to the ones in table 18 and 19. Twisting exhibits for each case and less radial expansion in table 20 as expected. The only difference is shrinking for PDMS in anisotropic model as we discussed before that fibers in anisotropic model dominate the overall behavior.

**a**

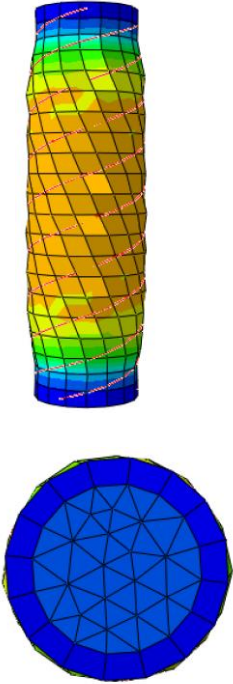
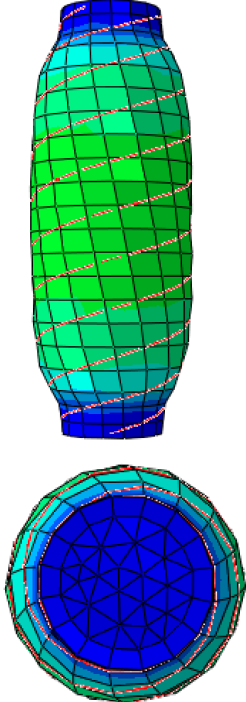


**b**

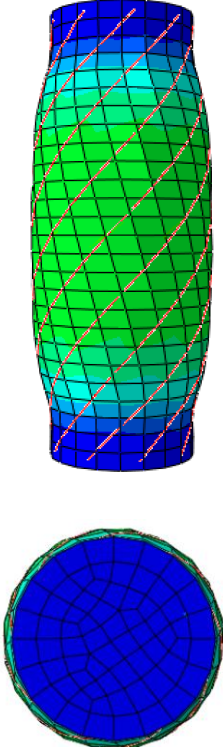
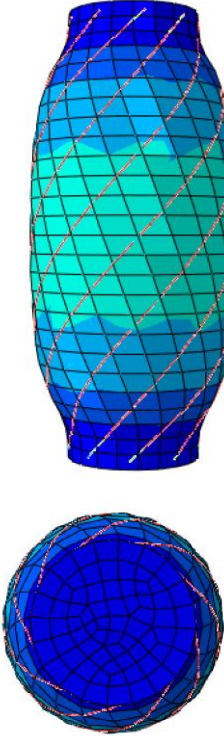


**Figure 28.** Undeformed model of single helical fiber with coarse mesh for 15 (a) and 45 fiber degree (b).

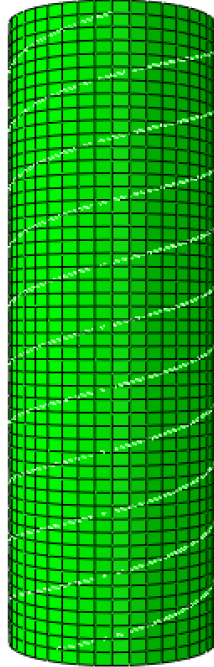
**Table 18** The contour plots of single helix fiber reinforced cylinder made of both PDMS and ecoflex in front and top view.

Initial fiber angle	Ecoflex  Von Mises Stress (MPa) <span style="color: red;">■</span> 0.02-20 <span style="color: green;">■</span> 0.01 <span style="color: blue;">■</span> 0	PDMS  Von Mises Stress (MPa) <span style="color: red;">■</span> 5-60 <span style="color: green;">■</span> 2.5 <span style="color: blue;">■</span> 0
15° fiber angle		

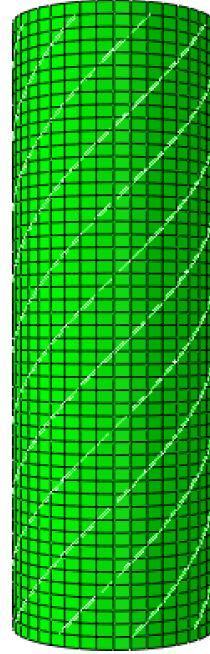
**Table 18** Continued

Initial fiber angle	Ecoflex	PDMS
45° fiber angle	<p data-bbox="533 371 724 394">Von Mises Stress (MPa)</p> <ul style="list-style-type: none"> <li data-bbox="533 405 619 427">■ 0.02-20</li> <li data-bbox="533 432 600 454">■ 0.01</li> <li data-bbox="533 459 587 481">■ 0</li> </ul> 	<p data-bbox="810 383 1002 405">Von Mises Stress (MPa)</p> <ul style="list-style-type: none"> <li data-bbox="831 416 917 439">■ 5-60</li> <li data-bbox="831 443 898 465">■ 2.5</li> <li data-bbox="831 470 885 492">■ 0</li> </ul> 

**a**

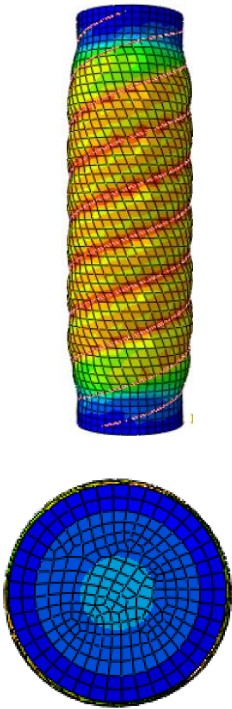
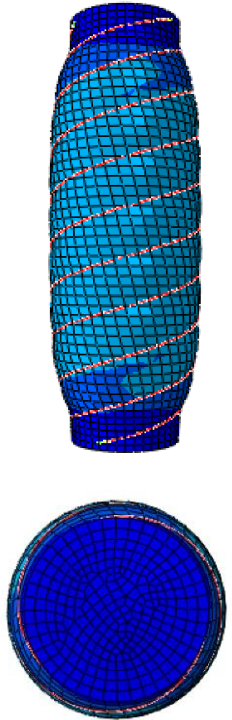


**b**

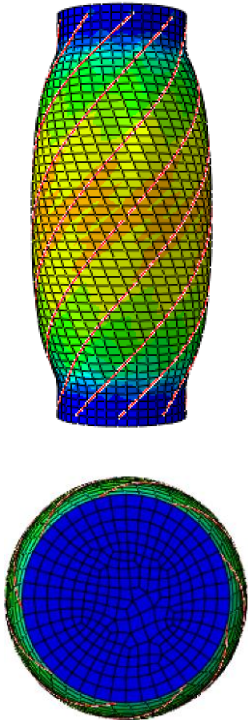
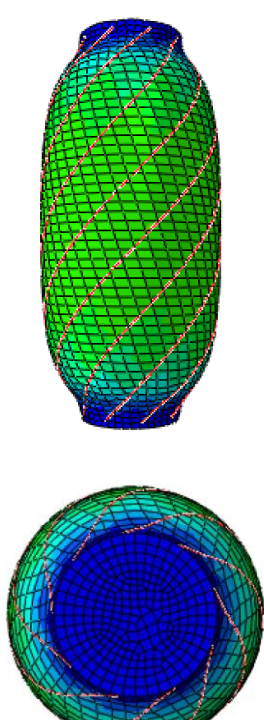


**Figure 29.** Undeformed model of single helical fiber with fine mesh for 15 (a) and 45 fiber degree (b).

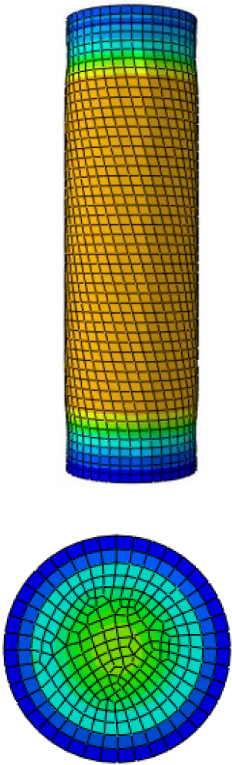
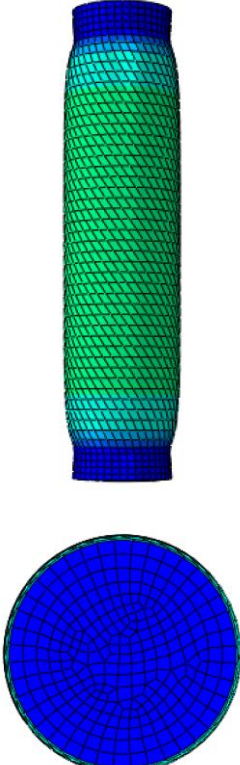
**Table 19** The contour plots with finer mesh of single helix fiber reinforced cylinder made of both PDMS and ecoflex in front and top view.

Initial fiber angle	Ecoflex Von Mises Stress (MPa) <span style="color: red;">■</span> 0.02-20 <span style="color: green;">■</span> 0.01 <span style="color: blue;">■</span> 0	PDMS Von Mises Stress (MPa) <span style="color: red;">■</span> 5-60 <span style="color: green;">■</span> 2.5 <span style="color: blue;">■</span> 0
15° fiber angle		

**Table 19** Continued

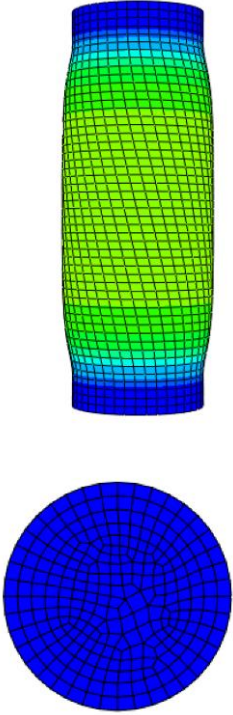
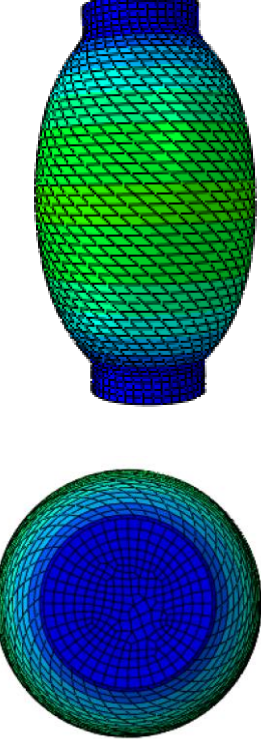
Initial fiber angle	<p>Ecoflex</p> <p>Von Mises Stress (MPa)</p> <ul style="list-style-type: none"> <li><span style="color: red;">■</span> 0.02-20</li> <li><span style="color: green;">■</span> 0.01</li> <li><span style="color: blue;">■</span> 0</li> </ul>	<p>PDMS</p> <p>Von Mises Stress (MPa)</p> <ul style="list-style-type: none"> <li><span style="color: red;">■</span> 5-60</li> <li><span style="color: green;">■</span> 2.5</li> <li><span style="color: blue;">■</span> 0</li> </ul>
45° fiber angle	 <p>Two views of an Ecoflex vessel with a 45° fiber angle. The top view is a perspective rendering showing a color gradient from blue (low stress) to red (high stress) across the vessel's surface. The bottom view is a circular cross-section showing the internal fiber structure and stress distribution.</p>	 <p>Two views of a PDMS vessel with a 45° fiber angle. The top view is a perspective rendering showing a color gradient from blue to red. The bottom view is a circular cross-section showing the internal fiber structure and stress distribution.</p>

**Table 20** The contour plots with finer mesh of single helix fiber reinforced cylinder made of anisotropic model in front and top view.

Initial fiber angle	Ecoflex  Von Mises Stress (MPa) <div style="display: flex; justify-content: space-around; font-size: small;"> <span style="color: red;">■</span> 0.02-20</div> <div style="display: flex; justify-content: space-around; font-size: small;"> <span style="color: green;">■</span> 0.01</div> <div style="display: flex; justify-content: space-around; font-size: small;"> <span style="color: blue;">■</span> 0         </div>	PDMS  Von Mises Stress (MPa) <div style="display: flex; justify-content: space-around; font-size: small;"> <span style="color: red;">■</span> 1-2.4</div> <div style="display: flex; justify-content: space-around; font-size: small;"> <span style="color: green;">■</span> 0.5</div> <div style="display: flex; justify-content: space-around; font-size: small;"> <span style="color: blue;">■</span> 0         </div>
15° fiber angle		



**Table 20** Continued

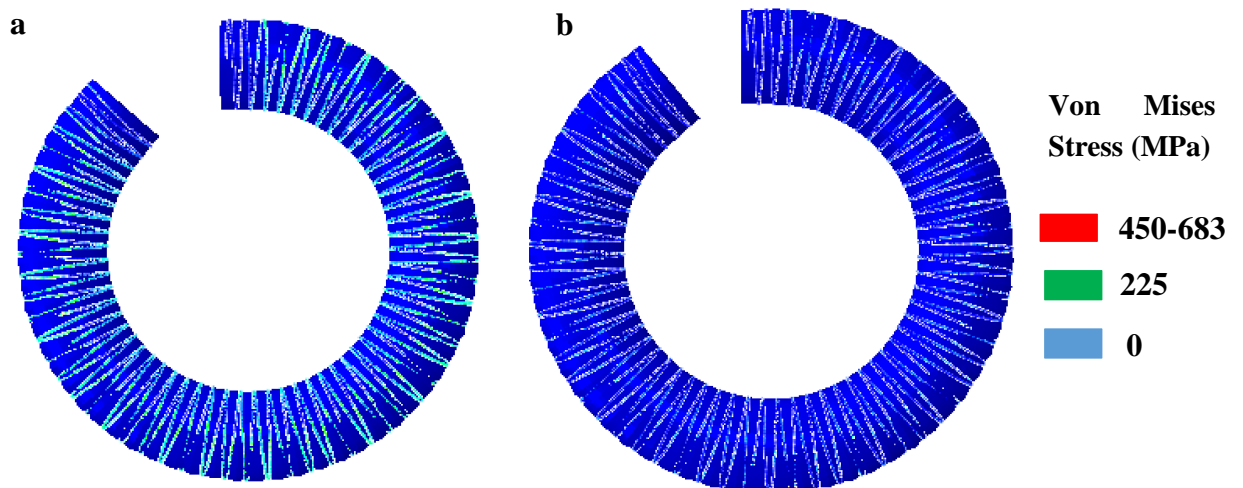
Initial fiber angle	Ecoflex  Von Mises Stress (MPa) <div style="display: flex; justify-content: space-around; font-size: small;"> <span style="color: red;">■</span> 0.02-20</div> <div style="display: flex; justify-content: space-around; font-size: small;"> <span style="color: green;">■</span> 0.01</div> <div style="display: flex; justify-content: space-around; font-size: small;"> <span style="color: blue;">■</span> 0         </div>	PDMS  Von Mises Stress (MPa) <div style="display: flex; justify-content: space-around; font-size: small;"> <span style="color: red;">■</span> 1-2.4</div> <div style="display: flex; justify-content: space-around; font-size: small;"> <span style="color: green;">■</span> 0.5</div> <div style="display: flex; justify-content: space-around; font-size: small;"> <span style="color: blue;">■</span> 0         </div>
45° fiber angle		

The second model considers bending of helical fiber-reinforced cylinders under an internal pressure. The composites with Ecoflex and PDMS are studied. As shown in Fig. 28, the structure is made of two material with hyperelastic material on the top half

and stiffer hyperelastic material at the bottom half. The length of the cylinder is 165mm and the dimension of cap is 18 mm. The double helix fiber composite is under internal pressure. The material parameters for stiffer material are  $\mu_e = 0.17MPa$ , while the parameter for ecoflex 00-30 is  $\mu = 0.017MPa$ ;  $\mu_b = 6.5MPa$ , while the parameter for PDMS is  $\mu = 0.65MPa$ . The right side of the body is totally fixed. Figure 29 provides the simulation results for PDMS and ecoflex matrix. Both matrix show similar deformation but high stress within PDMS matrix as expected.

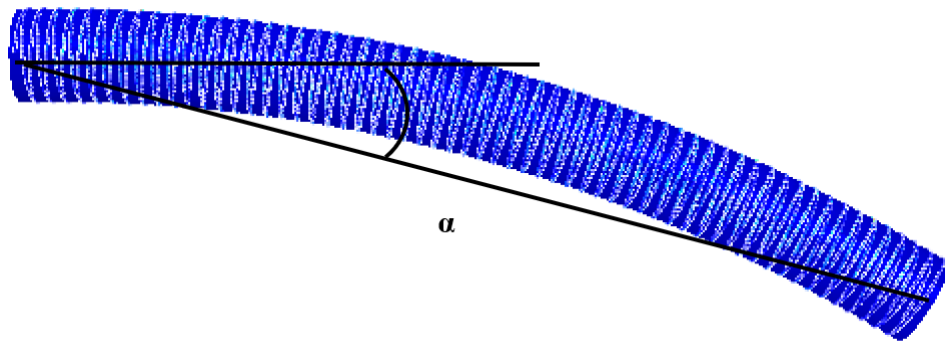


Fig. 30 Geometry of two material composite model

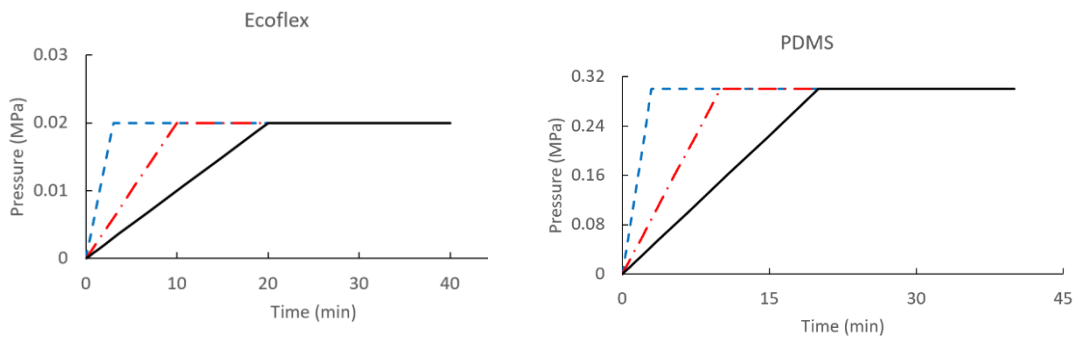


**Figure 31.** Comparison of von mises stress contour plot for different soft material (a) PDMS (b) Ecoflex

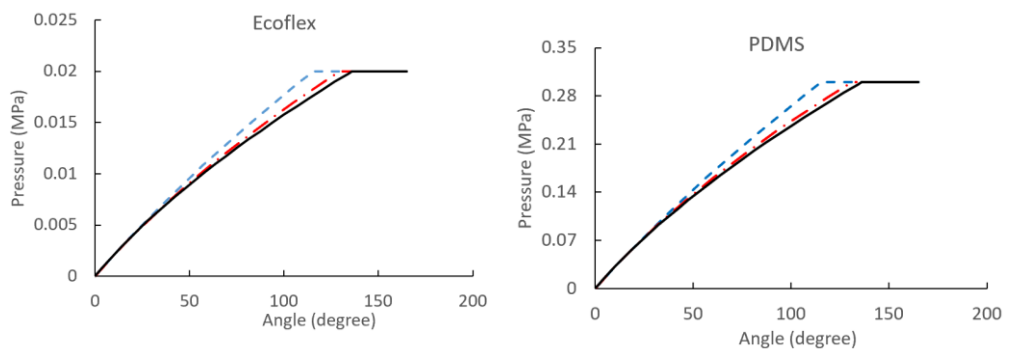
**a**



**b**



**c**



**Figure 32.** (a) The introduction of angle  $\alpha$  (b) time versus pressure (c) time versus angle (c) pressure versus angle  $\alpha$  for ecofelx and PDMS viscoelastic matrix

The time and pressure units in figure 30 are minutes and MPa. Fig. 30 showed the contour plots when the largest deformation has been reached. From Fig. 30, we

concluded that for helical fiber-reinforced cylinder model for both materials have similar results. It can be explained as the helical fibers limit the deformation in radial direction and the difference of the bending responses for the two soft materials are not significant. The angle  $\alpha$  presented in Fig. 30(a) is defined as the angle between horizontal axis and the line of center of two ends. The same material parameters used

The results of angle  $\alpha$  due to different loading rates indicate creep responses which show good agreement with the result in the previous section.

## CHAPTER IV

### CONCLUSION AND FUTURE WORK

In this study, we developed a constitutive model for nonlinear viscoelastic response of soft materials. Both isotropic and anisotropic responses are considered. The constitutive model is implemented within user material subroutines (UMAT) within ABAQUS finite element analysis. The subroutines are verified by uniaxial tension, equal biaxial tension and spherical inflation tests. Finite element is then used to simulate and investigate the response of the soft robotics devices, such as pneumatic soft actuators and micro-hands. The simulation tests are in good agreement in experiments. Furthermore, an investigation of soft composites comprising of elastic fiber and nonlinear viscoelastic matrix for potential applications in soft robots is presented. Parametric studies are carried out to obtain a better understanding of the design of soft composites.

In future, to meet the objective discussed above, we will consider the following tasks:

1. Model multi-layers vessels with different fiber angle in each layer to mimic vessels in humans. In this work, we only model single fiber reinforced layer and if we extend the model in human and animal tissues, multi-layer heterogenous model need to be considered.
2. The effect of higher fiber volume fraction on the mechanical behavior of soft composite is required to study. We only present the soft composite model with fiber

volume fraction 0.23 and 0.12, higher fiber volume fractions need to be considered and compared with human and animal tissues' experimental data.

3. Experimental data are needed to validate the soft composite models in last chapter.

Only simulation results of the soft composites are shown in this work, due to limited experimental data in literature.

4. Temperature need to be considered for accurate modeling since thermal condition has an effect on viscoelastic behavior. In this study, we only investigate the deformation by mechanical loading.

## REFERENCES

1. Bashir, R., *BioMEMS: state-of-the-art in detection, opportunities and prospects*. Advanced drug delivery reviews, 2004. **56**(11): p. 1565-1586.
2. Applegate, B., S. Kehrmeier, and G. Sayler, *A Chromosomally Based *tdxCDABE* Whole-Cell Reporter for Benzene, Toluene, Ethylbenzene, and Xylene (BTEX) Sensing*. Applied and Environmental Microbiology, 1998. **64**(7): p. 2730-2735.
3. Low, L.-M., et al., *Microactuators toward microvalves for responsive controlled drug delivery*. Sensors and Actuators B: Chemical, 2000. **67**(1-2): p. 149-160.
4. Trivedi, D., et al., *Soft robotics: Biological inspiration, state of the art, and future research*. Applied Bionics and Biomechanics, 2008. **5**(3): p. 99-117.
5. Kier, W.M. and K.K. Smith, *Tongues, tentacles and trunks: the biomechanics of movement in muscular-hydrostats*. Zoological Journal of the Linnean Society, 1985. **83**(4): p. 307-324.
6. Kier, W.M. and M.P. Stella, *The arrangement and function of octopus arm musculature and connective tissue*. Journal of Morphology, 2007. **268**(10): p. 831-843.
7. Napadow, V.J., R.D. Kamm, and R.J. Gilbert, *A biomechanical model of sagittal tongue bending*. JOURNAL OF BIOMECHANICAL ENGINEERING-TRANSACTIONS OF THE ASME, 2002. **124**(5): p. 547-556.
8. Cieślak, R., *Elephant trunk type elastic manipulator - A tool for bulk and liquid materials transportation*. Robotica, 1999. **17**(1): p. 11-16.
9. Martinez, R.V., et al., *Robotic tentacles with three-dimensional mobility based on flexible elastomers*. Advanced Materials, 2013. **25**(2): p. 205-212.
10. Ilievski, F., et al., *Soft Robotics for Chemists*. Angewandte Chemie, 2011(8).
11. Bar-Cohen, Y. and Q. Zhang, *Electroactive Polymer Actuators and Sensors*. MRS Bulletin, 2011. **33**(3): p. 173-181.
12. Koichi, S., i. shoichi, and t. hirohisa, *Development of flexible microactuator and its applications to robotic mechanisms*. IEEE International Conference on Robotics and Automation, 1991. **2**: p. 1622-1627.
13. Tsukagoshi, H., *Active hose: An artificial elephant's nose with maneuverability for rescue operation*. IEEE International Conference on Robotics and Automation, 2001. **3**: p. 2454-2459.

14. Mencias, A. and P. Dario, *Bio-Inspired Solutions for Locomotion in the Gastrointestinal Tract: Background and Perspectives*. 2003, The Royal Society. p. 2287.
15. Pritts, M.B., *Design of an artificial muscle continuum robot*. Proceedings - IEEE International Conference on Robotics and Automation, 2004. **2004**(5): p. 4742-4746.
16. Suzumori, K., *A bending pneumatic rubber actuator realizing soft-bodied manta swimming robot*. IEEE International Conference on Robotics and Automation., 2007: p. 4975-4980.
17. Kim, S., C. Laschi, and B. Trimmer, *Soft robotics: a bioinspired evolution in robotics*. Trends Biotechnol, 2013. **31**(5): p. 287-94.
18. Sfakiotakis, M., A. Kazakidi, and D.P. Tsakiris, *Octopus-inspired multi-arm robotic swimming*. Bioinspir Biomim, 2015. **10**(3): p. 035005.
19. Suarez, J.I., R.W. Tarr, and W.R. Selman, *Aneurysmal subarachnoid hemorrhage*. N Engl J Med, 2006. **354**(4): p. 387-96.
20. Gross, B.C., et al., *Polymer coatings in 3D-printed fluidic device channels for improved cellular adherence prior to electrical lysis*. Analytical chemistry, 2015. **87**(12): p. 6335-6341.
21. Chanda, A. and C. Callaway, *Tissue Anisotropy Modeling Using Soft Composite Materials*. 2018.
22. Chanda, A. and H. Ghoneim, *Pumping potential of a two-layer left-ventricle-like flexible-matrix-composite structure*. Composite Structures, 2015. **122**: p. 570-575.
23. Moreira, C.S. and L.C.S. Nunes, *Effects of fiber orientation in a soft unidirectional fiber-reinforced material under simple shear deformation*. International Journal of Non-Linear Mechanics, 2019. **111**: p. 72-81.
24. Yousefsani, S.A., A. Shamloo, and F. Farahmand, *Nonlinear mechanics of soft composites: hyperelastic characterization of white matter tissue components*. Biomechanics and Modeling in Mechanobiology, 2019.
25. Holzapfel, G.A. and T.C. Gasser, *A viscoelastic model for fiber-reinforced composites at finite strains: Continuum basis, computational aspects and applications*. Computer Methods in Applied Mechanics and Engineering, 2001. **190**(34): p. 4379-4403.
26. Nguyen, T.D., R.E. Jones, and B.L. Boyce, *Modeling the anisotropic finite-deformation viscoelastic behavior of soft fiber-reinforced composites*. International Journal of Solids and Structures, 2007. **44**(25): p. 8366-8389.



27. Davies, P.J., F.J. Carter, and A. Cuschieri, *Mathematical modelling for keyhole surgery simulations: a biomechanical model for spleen tissue*. IMA Journal of Applied Mathematics, 2002. **67**(1): p. 41-67.
28. Chui, C., et al., *Combined compression and elongation experiments and non-linear modelling of liver tissue for surgical simulation*. Medical and Biological Engineering and Computing, 2004. **42**(6): p. 787-798.
29. Martins, P.A.L.S., R.M.N. Jorge, and A.J.M. Ferreira, *A Comparative Study of Several Material Models for Prediction of Hyperelastic Properties: Application to Silicone-Rubber and Soft Tissues*. Strain, 2006. **42**(3): p. 135-147.
30. Gent, A.N. and Knovel (Firm), *Engineering with rubber : how to design rubber components*. 3rd ed. 1 online resource (xviii, 433 pages).
31. Ogden, R.W., G. Saccomandi, and I. Sgura, *Fitting hyperelastic models to experimental data*. Computational Mechanics, 2004. **34**(6): p. 484-502.
32. Mansouri, M.R. and H. Darijani, *Constitutive modeling of isotropic hyperelastic materials in an exponential framework using a self-contained approach*. International Journal of Solids and Structures, 2014. **51**(25): p. 4316-4326.
33. Boyce, M.C., *Direct Comparison of the Gent and the Arruda-Boyce Constitutive Models of Rubber Elasticity*. Rubber Chemistry and Technology, 1996. **69**(5): p. 781-785.
34. Puglisi, G. and G. Saccomandi, *The Gent model for rubber-like materials: An appraisal for an ingenious and simple idea*. International Journal of Non-Linear Mechanics, 2015. **68**: p. 17-24.
35. Einstein, D. and I. Vesely, *Invariant formulation for dispersed transverse isotropy in aortic heart valves: An efficient means for modeling fiber splay*. Biomechanics and modeling in mechanobiology, 2005. **4**: p. 100-117.
36. Sun, W. and M.S. Sacks, *Finite element implementation of a generalized Fung-elastic constitutive model for planar soft tissues*. Biomechanics and modeling in mechanobiology, 2005. **4**(2-3): p. 190-199.
37. Humphrey, J. and F. Yin, *A new constitutive formulation for characterizing the mechanical behavior of soft tissues*. Biophysical journal, 1987. **52**(4): p. 563-570.
38. Holzapfel, G.A., T.C. Gasser, and R.W. Ogden, *A New Constitutive Framework for Arterial Wall Mechanics and a Comparative Study of Material Models*. Journal of elasticity and the physical science of solids, 2000. **61**(1): p. 1-48.

39. Gasser, T.C., R.W. Ogden, and G.A. Holzapfel, *Hyperelastic modelling of arterial layers with distributed collagen fibre orientations*. *Journal of the royal society interface*, 2006. **3**(6): p. 15-35.
40. Skacel, P. and J. Bursa, *Material parameter identification of arterial wall layers from homogenised stress–strain data*. *Computer methods in biomechanics and biomedical engineering*, 2011. **14**(01): p. 33-41.
41. Jamison, C.E., R.D. Marangoni, and A.A. Glaser, *Viscoelastic Properties of Soft Tissue by Discrete Model Characterization*. *Journal of Engineering for Industry*, 1968. **90**(2): p. 239-247.
42. Rashid, B., M. Destrade, and M.D. Gilchrist. *Hyperelastic and Viscoelastic Properties of Brain Tissue in Tension*. in *ASME 2012 International Mechanical Engineering Congress and Exposition*. 2012.
43. Pioletti, D.P., et al., *Viscoelastic constitutive law in large deformations: application to human knee ligaments and tendons*. *Journal of Biomechanics*, 1998. **31**(8): p. 753-757.
44. Limbert, G. and J. Middleton, *A transversely isotropic viscohyperelastic material: Application to the modeling of biological soft connective tissues*. *International Journal of Solids and Structures*, 2004. **41**(15): p. 4237-4260.
45. HOLZAPFEL, G.A., *ON LARGE STRAIN VISCOELASTICITY: CONTINUUM FORMULATION AND FINITE ELEMENT APPLICATIONS TO ELASTOMERIC STRUCTURES*. *International Journal for Numerical Methods in Engineering*, 1996. **39**(22): p. 3903-3926.
46. Bischoff, J.E., E.M. Arruda, and K. Grosh, *A rheological network model for the continuum anisotropic and viscoelastic behavior of soft tissue*. *Biomechanics and Modeling in Mechanobiology*, 2004. **3**(1): p. 56-65.
47. Green, M.S. and A.V. Tobolsky, *A New Approach to the Theory of Relaxing Polymeric Media*. *The Journal of Chemical Physics*, 1946. **14**(2): p. 80-92.
48. Lockett, F.J. and F. Lockett, *Nonlinear viscoelastic solids*. 1972: Academic Press London.
49. Morman, K., *Rubber Viscoelasticity: A Review of Current Understanding*. 1985: Ford Motor Company.
50. Schapery, R., *Nonlinear viscoelastic solids*. *International Journal of Solids and Structures*, 2000. **37**(1-2): p. 359-366.
51. Muliana, A., K.R. Rajagopal, and A.S. Wineman, *A new class of quasi-linear models for describing the nonlinear viscoelastic response of materials*. *Acta Mechanica*, 2013. **224**(9): p. 2169-2183.

52. Fung, Y.C., *Biomechanics : mechanical properties of living tissues*. Second edition. ed. 1993: Springer-Verlag.
53. Freed, A.D. and K.R. Rajagopal, *A viscoelastic model for describing the response of biological fibers*. *Acta Mechanica*, 2016. **227**(12): p. 3367-3380.
54. Abramowitch, S.D., et al., *An Evaluation of the Quasi-Linear Viscoelastic Properties of the Healing Medial Collateral Ligament in a Goat Model*. *Annals of Biomedical Engineering*, 2004. **32**(3): p. 329-335.
55. Drapaca, C.S., et al., *A Quasi-linear Viscoelastic Constitutive Equation for the Brain: Application to Hydrocephalus*. *Journal of Elasticity*, 2006. **85**(1): p. 65-83.
56. Suchocki, C., *A quasi-linear viscoelastic rheological model for thermoplastics and resins*. *Journal of Theoretical and Applied Mechanics*, 2013. **51**: p. 117-129.
57. Muliana, A., K.R. Rajagopal, and D. Tscharnuter, *A Nonlinear Integral Model for Describing Responses of Viscoelastic Solids*. *International Journal of Solids and Structures*, 2015. **58**.
58. Mehrabadi, M.M. and S. Nemat-nasser, *Some basic kinematical relations for finite deformations of continua*. *Mechanics of Materials*, 1987. **6**(2): p. 127-138.
59. *Soft Material Characterization for Robotic Applications*. *Soft Robotics*, 2015. **2**(2): p. 80-87.
60. Muliana, A., K.R. Rajagopal, and D. Tscharnuter, *A nonlinear integral model for describing responses of viscoelastic solids*. *International Journal of Solids and Structures*, 2015. **58**: p. 146-156.
61. Po-Jung, H., et al., *Pneumatically Actuated Soft Micromold Device for Fabricating Collagen and Matrigel Microparticles*. *Soft Robotics*, 2017. **4**(4): p. 390-399.
62. Holzapfel, G.A., G. Sommer, and P. Regitnig, *Anisotropic mechanical properties of tissue components in human atherosclerotic plaques*. *J Biomech Eng*, 2004. **126**(5): p. 657-65.
63. C., C.J., W.E. L., and K.R. K., *Soft Material Characterization for Robotic Applications*. *Soft Robotics*, 2015. **2**(2): p. 80-87.
64. Steck, D., et al., *Mechanical responses of Ecoflex silicone rubber: Compressible and incompressible behaviors*. *Journal of Applied Polymer Science*, 2019. **136**(5): p. 47025.